The Role of Domain II and Domain IV Extracellular Turrets in Determining Ion Selectivity in the T-type Calcium Channel from *Lymnaea stagnalis*

by

Robert Stephens

A thesis

presented to the University of Waterloo

in fulfillment of the

thesis requirement for the degree of

Masters of Science

in

Biology

Waterloo, Ontario, Canada, 2016

AUTHOR'S DECLARATION

I hereby declare that I am the sole author of this thesis. This is a true copy of the thesis, including any required final revisions, as accepted by my examiners.

I understand that my thesis may be made electronically available to the public.

Abstract

The T-type calcium channel from the pond snail *Lymnaea stagnalis*, LCa_v3, undergoes alternative splicing in exon 12. Exon 12 codes for the L5 structure (S5-P) in Domain II (DII), which is dubbed the "turret". The turret is a cysteine-rich extracellular loop near the selectivity filter. The selectivity filter is critical for ion selectivity. The DII turret is capable of influencing ion selectivity in the LCa_v3 channel, possibly through interactions with the selectivity filter.

LCa_v3 with exon 12a is highly sodium-selective, whereas LCav3-12b is more calcium-selective. The turret of exon 12a is different from the turret of exon 12b in its size (number of amino acids) and cysteine configuration. Genome and transcriptome analyses have revealed that some cnidarians possess two versions of the genes encoding T-type calcium channels, and that these gene products differ from one another based on the size and cysteine configurations of their Domain IV turrets. We hypothesize that the Domain IV turret is playing a role in determining ion selectivity in T-type calcium channels.

We created T-type calcium channel chimeras and investigated their ion selectivity in whole-cell patch clamp recordings of transfected HEK293T cells. Chimeras were created, in which the Domain IV turret from LCa_v3 was replaced by the Domain IV turret from $Ca_v3.2$. Cav3.2 is a highly calcium-selective human T-type channel. Each of the chimeras possessed increased calcium selectivity. Calcium selectivity in the LCa_v3-12b $DIV_{\alpha 1hL}$ chimera approached the levels of calcium-selectivity observed in human channels. However, we found that the Domain II turret has a dominant influence on selectivity.

The research presented here provides support for a role in ion selectivity for extracellular turrets. A structural model, based on the recently resolved $Ca_v1.1$ cryo-EM structure, is proposed here to explain how turrets could influence ion selectivity.

Acknowledgements

I would like to begin this thesis by thanking the people that made it possible – starting with my wonderful teammates in the Spafford lab. Throughout my years as a member of the Spafford lab, I have encountered many brilliant scientists and dedicated students. I could never thank Dr. Spafford enough for everything that he has done for me, and all that he continues to do for me. I believe that I have grown immensely as a person in the last four years because I have been lucky to have amazing mentors. David Spafford is at the top of my list as an incredible mentor. He is dedicated to science and passionate about his craft. The excitement is contagious.

Wendy Guan has also been an incredible mentor. If I have acquired any practical skills as a scientist, it is only because of her guidance. I have also learned innumerable life-lessons from Wendy. I also want to thank Adriano Senatore and Adrienne Boone, because without them my project would not have existed. Adrienne and Adriano are both incredible scientists, and it was an honour to learn from them early on in my career. Julia Fux has been a great friend and an incredible teacher. Julia is always smiling and approachable, and she has always been willing to help out whenever I needed it.

I am also grateful for the friendships that I have gained over the years. Amrit Mehta, basically the chillest yet hardest-working guy I know. Always awesome to spend time with you, you made tackling our daily problems in the lab fun. I'm lucky to call Amrit a friend a role model. Jennifer Czekus (no idea how to say it), I always have a good time chatting about basically anything with you. Brilliant, funny, friendly, and always happy to help. To all of the other students that have been a part of this journey, I appreciate each and every one of you. I have had great TA partners, amazing 499 students, the best classmates, and all of my fellow grad

students in Science are incredible. This program has been stressful, but more than that, it has been fun because of the people I've encountered.

To my committee members, Dr. Michael Beazely, Dr. Paul Craig and Dr. Bob French, thank you for taking the time to read my thesis and for meeting with me to offer your guidance over the past two years. Your advice and expertise throughout this process is greatly appreciated.

Finally, I'd like to thank my family. To my partner and best friend Chloe: I can't thank you enough for everything that you do for me. You are always supportive, always encouraging, and always on my side. When I have been stressed out, you find a way to make the stress melt away. I want to thank my parents. They have always been supportive of my goals and have always helped out in every way possible. To my Aunt Lisa, Uncle Kenny, Aunt Marg, and Uncle Rob: thank you for your kindness and everything that you've done for me. You have let me into your homes and provided me with so much. And to my sister and brothers – Rebecca, Daniel, James – you've been my best friends my whole life, and have always helped me to put things in perspective and relax every once in a while. I appreciate this more than you could know. You're all inspirational and great role models.

To everyone that has made this journey a success and good time, thank you.

Table of Contents

List of Figures

List of Tables

List of Abbreviations

DI/DII/DIII/DIV	Domains I/II/III/IV
Cryo-EM	Cryo-electron microscopy
HVA	High voltage activated
LVA	Low voltage activated
TM	Transmembrane
VSD	Voltage-sensor domain
PD	Pore domain
L5/L6	Extracellular loops 5 and 6
MD	Molecular dynamics
PMF	Potentials of mean force
HFS	High-field strength site
HEK2933T	Human embryonic kidney cells (293T)
AMFE	Anomalous mole fraction effect
DMEM	Dulbecco's modified eagle's medium
EGTA	Ethylene glycol tetra-acetic acid
FBS	Fetal bovine serum
LB	Luria Bertani broth
NEB	New England Biolabs
HEPES	4-(2-hydroxyethyl)-1-piperazineethanesulfonic acid
HES	HEPES-buffer saline
NMDG	N-methyl-D-glucamine
SB	Super broth
TEA	Tetraethylammonium
TTA-P2	3,5-dichloro-N-[1-(2,2-dimethyl-tetrahydro-pyran-4-ylmethyl)-4-fluoro-piperidin-4-ylmethyl]-benzamide

1. Introduction

Ion channels are numerous and diverse, with as many as 235 genes in the human genome coding for ion channel pore-forming subunits (Jegla et al., 2009). This accounts for nearly 1% of the entire protein-coding genes in humans (Jegla et al., 2009). These diverse channels are grouped into many different families (Figure 1.1).

Channels are classified based upon ion selectivity and gating properties. A common feature of ion channels is the ability to form an ion-permeable pathway to allow ions to flow down their electrochemical gradients, using the potential energy generated from electrochemical gradients. The vast majority of ion channels have evolved to derive the energy required for gating from one of three sources: transmembrane voltage, mechanical force, and ligand binding (Jegla et al., 2009). Those channels that open in response to transmembrane voltage changes are referred to as voltage-gated ion channels. The physiological ions for these channels are generally cations, but this superfamily of proteins is often broadly referred to as the voltage-gated ion channels.

Different voltage-gated ion channels are classified on the basis of their ion selectivity, and ion selectivity is critically important to the functional character of different families of voltage gated ion channels. For example, pacemaking currents in mammalian sino-atrial (SA) nodes have seven identifiable ion current types. These include the sustained inward sodium current (I_{st}), the delayed rectifier potassium current (K_{ir}), the muscarinic potassium current, the sodium/potassium pump current, funny currents (I_f) controlled by non-selective hyperpolarization-activated cyclic nucleotide gated channel (HCN), and L- and T- type channel calcium currents (Grant, 2009; Mitsuiye et al., 2000; Ono and Iijima, 2010; Zamponi, 2005).

Evidently, there is a vast functional diversity of ionic currents through many different channels in the sino-atrial node; in contributing to the shape of the action potential(s) in the SA node, each channel must preferentially pass specific ions with high probability at a certain time. In the heart, and on the membranes of many cells throughout the body, the proper functioning of ion channels is highly dependent on their ability to preferentially select some ions over others. Despite the critical importance of ion selectivity, the mechanism(s) responsible for ion selectivity in these channels are not fully understood.

This thesis is concerned with exploring some distinct structural features of T-type calcium channels which allows them to alter their ion selectivity to be either more or less calcium selective. In 2014, the Spafford lab published an article on the presence of two splice isoforms of the T-type calcium channel from *Lymnaea stagnalis*, which are dubbed LCa_v3-12a and LCa_v3-12b (Senatore et al., 2014). LCa_v3-12b is relatively calcium selective, whereas LCa_v3-12a is essentially a sodium channel (Figure 1.14). The structural difference between these two channel isoforms is within the extracellular loop in Domain II (L5-P-L6), also referred to as the turret (Senatore et al., 2014). Further analysis revealed uniquely cysteine rich turrets in T-type channels. The Domain II and Domain IV turrets from invertebrate T-types have a distinctively different cysteine arrangement when compared to the T-types of vertebrates (Figure 1.13, 1.15-1.18). The calcium versus sodium selectivity is also different between invertebrates and vertebrates (Figure 1.14). Besides cysteine arrangements within the turrets, the length of the turret sequences might also be playing an important role in influencing ion selectivity (Figure 1.16). This thesis will explore the role of the extracellular loops in Domain II and Domain IV in determining ion selectivity in the T-type calcium channel from *L. stagnalis*, LCa_v3.

I Support For This Study

It should be noted that alternative splicing in LCa_v3 from *Lymnaea stagnalis* to generate two isoforms with different Domain II extracellular turrets was discovered by Adriano Senatore as a part of his doctoral thesis (2013). The involvement of these turrets in the regulation of ion selectivity formed a chapter in Dr. Senatore's thesis. From there, a description of the altered ion selectivity of T-type channels in the snail heart, a description of variable sodium selectivity in wild-type human T-type channels (i.e., $Ca_v3.1$, $Ca_v3.2$, and $Ca_v3.3$), electrophysiological analysis of snail T-types lacking cysteines in their Domain II turrets (LCa_v3-12a ΔCys and LCa_v3- 12b ΔCys) and a chimeric channel containing the Domain II turret from human $Ca_v3.2$ in snail LCav3 (LCav3-$DII_{\alpha 1hL}$) formed the Master's thesis of a previous MSc student in the Spafford lab, Wendy Guan (2014).

This thesis expands into the analyses of more turret chimeras generated between $Ca_v3.2$ and snail LCa_v3, including Domain IV turret swaps. Domain II turret swaps, in which LCa_v3 turrets 12a and 12b are cloned into $Ca_v3.2$, and a mutation in the Domain II pore (D to N), are also briefly discussed. The molecular cloning work to generate two of the channel chimeras that are included in this thesis ($Ca_v3.2$-12a and $Ca_v3.2$-12b) were carried out by MSc student Amrit Mehta. One of the Domain IV chimeras, LCa_v3-12b $DIV_{\alpha 1hL}$, was created by undergraduate project student Omar Mourad. Modeling of the folding pattern of the snail Domain II turret, based on the amino acid coordinates derived from the three-dimensional structure of $Ca_v1.1$ (resolved by cryo-electron microscopy), was carried out by Dr. Boris Zhorov (Unpublished; McMaster University).

Before introducing the objectives and hypothesis of this research, there is a brief introduction to voltage-gated calcium channels, important functional and structural features of Ca_v3 T-type

calcium channels, and a discussion of long-standing and widely accepted theories regarding ion selectivity in ion channels.

II Voltage-Gated Calcium Channels

The different calcium channels were first distinguished based upon their voltage activation. In 1975, Susumo Hagiwara and colleagues identified two separable calcium selective currents in recordings of starfish eggs (Hagiwara et al., 1975). These distinct current peaks were assumed to be facilitated by two different calcium channels, which were named 'channel I' and 'channel II'. As it turns out, channel I and channel II were not simply two different channels, but instead represent two broad groups of calcium channels: the low-voltage activated (LVA) calcium channels and the high-voltage activated (HVA) calcium channels, respectively (See Figure 1.2). The LVA channels open after small depolarizations, and can therefore open at potentials near the resting state. The HVA channels open from larger depolarizations. In the decade following the groundbreaking work of Hagiwara et al., LVA and HVA currents were identified in mammalian inferior olivary neurons, mammalian thalamic neurons, the lateral thalamic nuclei from cats, and embryonic chick neurons, and several others (Bean, 1985; Carbone and Lux, 1987; Kostyuk et al., 1985; Llinas and Yarom, 1981; Matteson and Armstrong, 1986; Nilius et al., 1985; Veselovski and Fedulova, 1983).

The LVA and HVA currents were further characterized in 1985 by Nowycky and colleagues. The calcium channels were differentiated based upon their single channel conductance, utilizing the barium ion (Ba^{2+}) as a charge carrier (Nowycky et al., 1985). The LVA channels were characterized as T-type calcium channels due to their *transient* opening and

tiny single channel conductance. Nowycky et al. further differentiated the HVA channels as either L-type or N-type. L-type channels displayed a single channel conductance that was *large* and *long-lasting*, whereas the N-type channels were *intermediate* and *neuronal*. The N-type channels are intermediate in the sense that they require strongly negative potentials for removal of inactivation (unlike L-type) and strong depolarizations for activation (i.e. HVA, unlike T-type). Other non-L-type HVA channels have also been described. These include the P/Q-type channels and the R-type channels.

In the mammalian genome, ten calcium channel protein-coding genes are known. These genes are distinguished on the basis of sequence similarity in the α1 pore-forming subunits. There are four L-type channel genes within the Ca_v1 gene family ($Ca_v1.1$-1.4). The non-L-type HVA channels (i.e. N-type, P/Q-type, and R-type) are within the Ca_v2 gene family ($Ca_v2.1$-2.3). T-type channels are within the Ca_v3 gene family and include $Ca_v3.1$, $Ca_v3.2$, and $Ca_v3.3$ channels (Ertel et al., 2000). Most invertebrates have only a single representative gene for each of the classes of calcium channels (Senatore and Spafford, 2010; Spafford et al., 2006, 2003). For example, the great pond snail *Lymnaea stagnalis* has only three calcium channel genes – LCa_v1, LCa_v2, and LCa_v3 (see Figure 1.2). In some organisms, such as LCa_v3, alternative splicing of voltage gated ion channels has been discovered (Cens et al., 2015; Senatore and Spafford, 2012; Senatore et al., 2014). The T-type calcium channels will be the focus of this research, in particular LCa_v3 and $Ca_v3.2$.

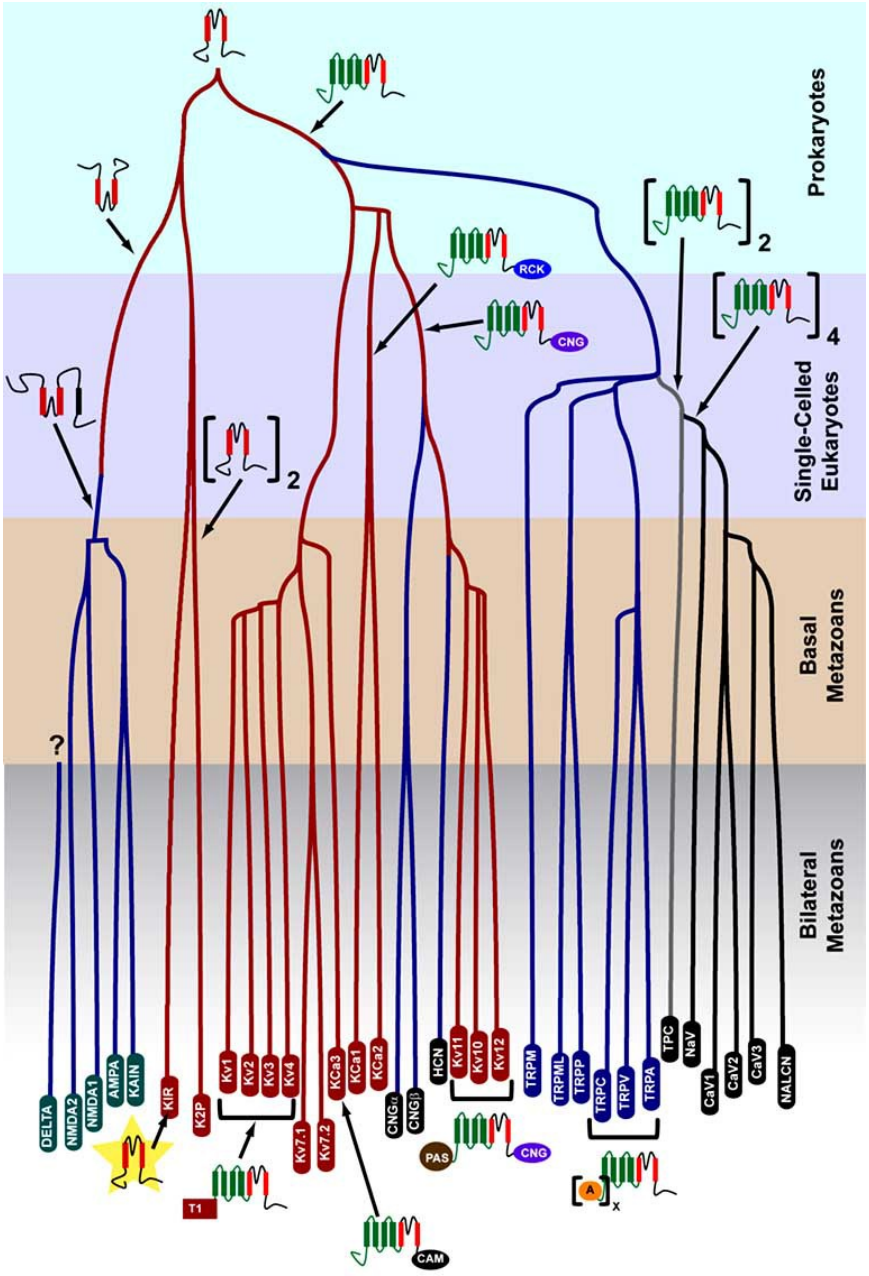

Figure 1.1 Evolutionary Relationships and Origins of the Conserved Metazoan Families of the Voltage-Gated Cation Channel Superfamily

Branches are labeled by gene family at the bottom and branch color indicates K^+ selectivity (red), Na^+ and/or Ca^{2+} permeable tetrameric channels (blue), dimeric channels (X2 homology domains) (grey) and monomeric channels (X4 homology domains) (black). See (Jegla et al., 2009).

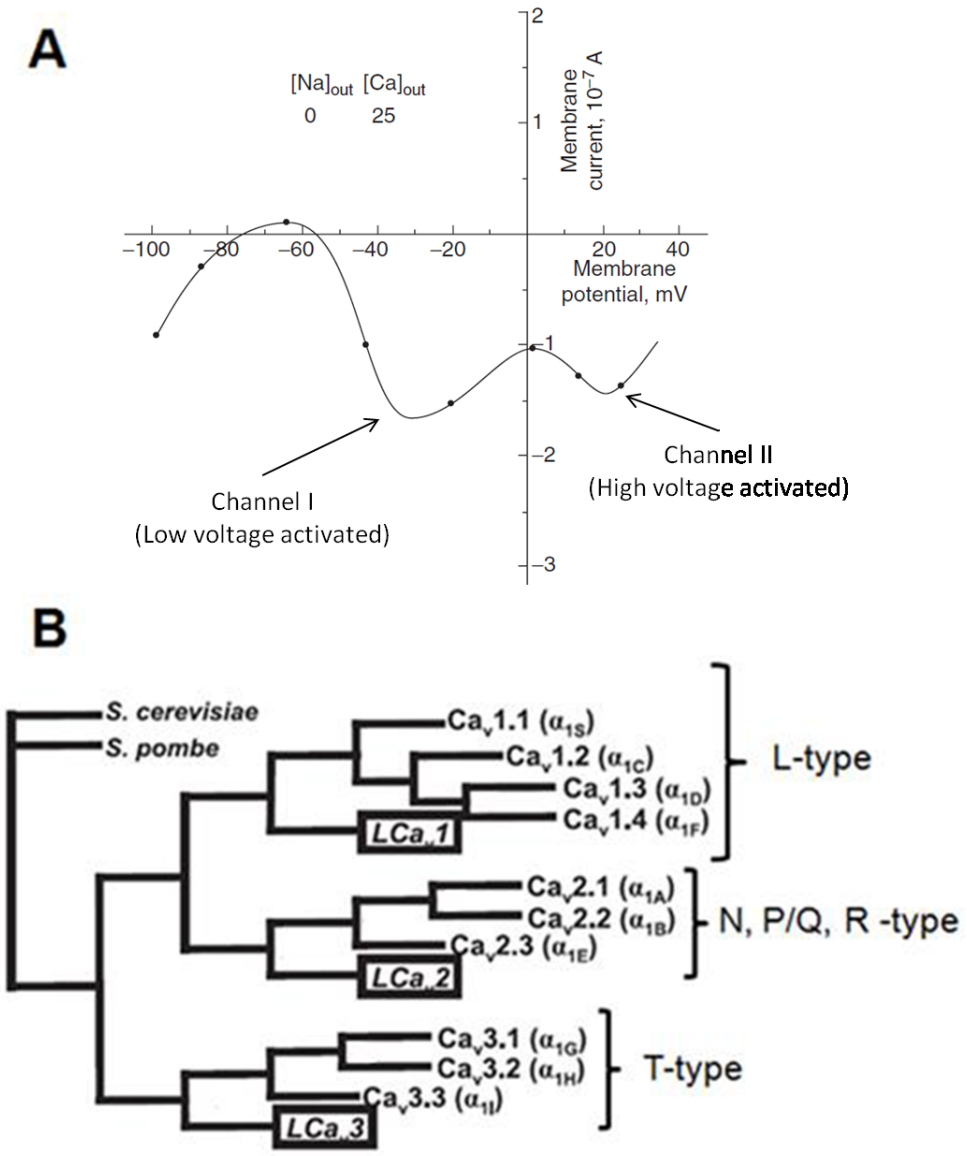

Figure 1.2 Low- and High- Voltage Activated Calcium Channels

(A) Hagiwara et al. discovered two calcium channels in starfish eggs based upon their voltage activation. The low voltage activated channels (T-types) open near -40 mV membrane potential, and high voltage activated (N, P/Q, R- types and L-types) open near 20 mV. (B) Gene tree showing various calcium channels from humans (10 genes) and the pond snail, *Lymnaea stagnalis* (3 genes) with the out-groups *S. cerevisiae* and *S. pombe* included. A: (Hagiwara et al., 1975); B: (Senatore et al., 2012).

III T-type Calcium Channels (Ca_v3): Structural and Functional Features

T-type calcium channels are 4x6TM voltage-gated ion channels of the gene family Ca_v3 in mammals. Like other Ca_v, Na_v, and NALCN channels, the 4x6TM T-type calcium channels contain a single long polypeptide that encompasses four 6-TM Domains (DI-DII-DIII-DIV) of twenty-four segments; each domain is connected by cytoplasmic linkers between Domains I-II, II-III and III-IV. There is strong evidence to suggest that the 4x6TM channels arose as a result of gene duplication events of the K_v pore-forming genes (Strong et al., 1993). Typically, in K_v channels, four 6-TM subunits are arranged within the membrane to create the pore-forming subunit of the channel. These subunits can combine to form homomultimers or heteromultimers with members within the same potassium channel family (Anderson and Greenberg, 2001). The genes encoding Ca_vs and Na_vs might have evolved as a result of two rounds of gene duplication of the single-domain channel gene encoding the ancestral K_v channel subunit. This is supported by evidence that DI is more similar to DIII and DII is more similar to DIV in Navs (Strong et al., 1993). The similarities between DII and DIV will be of importance in the research presented here. A summary of these proposed duplication events is provided in Figure 1.3.

The predicted topology for T-type channels can be seen in Figure 1.4. Note the presence of four homologous domains (DI-DIV) each comprised of a voltage-sensor domain (VSD) and a pore domain (PD) and are connected by cytoplasmic linkers.

The domains DI-DIV fold up in the channel membrane to create the voltage sensor domain (VSD) which is connected to the pore domain (PD) via the linker helix between S4 and S5; this linker helix is denoted as L45. Movements in S4 of the VSD in response to voltage changes in the membrane are transmitted to the S5 of the PD through the L45. This allows the

channel pore to open (Catterall, 1986; Guy and Seetharamulu, 1986; Oelstrom et al., 2014; Zhao et al., 2004).

The process of channel opening in response to membrane depolarization is known as activation. The mechanisms of activation in the pore domain of 4x6TM channels have been inferred from studies of other voltage-gated ion channels, including NaChBac, bacterial K^+ channels, and the *Shaker* channels from *Drosophila* (Doyle et al., 1998; Jiang et al., 2002a, 2002b; Webster et al., 2004; Zhao et al., 2004). The evidence provided by the aforementioned studies indicates that movements transmitted to the PD from the VSD cause movements in S6, which lines the channel pore. In the closed state, S6 is in a straight conformation and the S6 helices from the different domains (DI-DIV) are crossed in a bundle close to the pore at the intracellular end (see Figure 1.5 for positions of S6). Upon activation, pulling on L45 leads to bending of the S6 segment and separation of the S6 helical bundle at the intracellular mouth of the pore – this leads to channel opening (Catterall, 2010; Oelstrom et al., 2014; Stühmer et al., 1989). Due to overall structural homology, it is assumed that the process is similar, if not identical, in other voltage-gated ion channels.

Compared to the high voltage activated (HVA) Ca_v1 and Ca_v2 channels, Ca_v3 channels are distinguished by low voltage activation (LVA) which allows them to function close to resting membrane potentials (Senatore et al., 2012). The kinetics (i.e., rate of opening and closing) of T-type channels are also more rapid compared to HVA channels. The proximal I-II linker of T-type channels contains a specialized structure involved in the regulation of the channel's kinetics of activation and inactivation (Figure 1.4). This 'gating brake' is a helix-loop-helix structure that is highly conserved, even within the T-type channels of the most primitive multicellular eukaryotes (Senatore et al., 2012). If the gating brake is deleted, the mutants display 'runaway gating',

whereby the channels activate at hyperpolarized potentials and display even faster kinetics than normal T-type channels.

The biophysical characterization of channel behavior involves determining the kinetics of activation, inactivation, recovery from inactivation, and deactivation (Hille, 2001). The biophysical properties of the channels studied as a part of this thesis will be a secondary consideration of this research (with the primary consideration being changes in ion selectivity). Activation is the process of channel opening, and deactivation is the process of channel closing from an opened state - which is usually studied by measuring the decay of tail currents (Molleman, 2003). Inactivation refers to the process of channels moving to a refractory state after opening (Hille, 2001). After a period of time, or upon hyperpolarization, channels will undergo a de-inactivation and leave the refractory state (i.e. recovery from inactivation). The voltage-sensitivity and the decay kinetics of state changes (inactivation, deactivation) can be studied using tau exponential fits. For inactivation, a larger tau value means that a smaller proportion of channels will move to the refractory state in a given period of time. For activation, time-to-peak current will be determined as an indicator of kinetics.

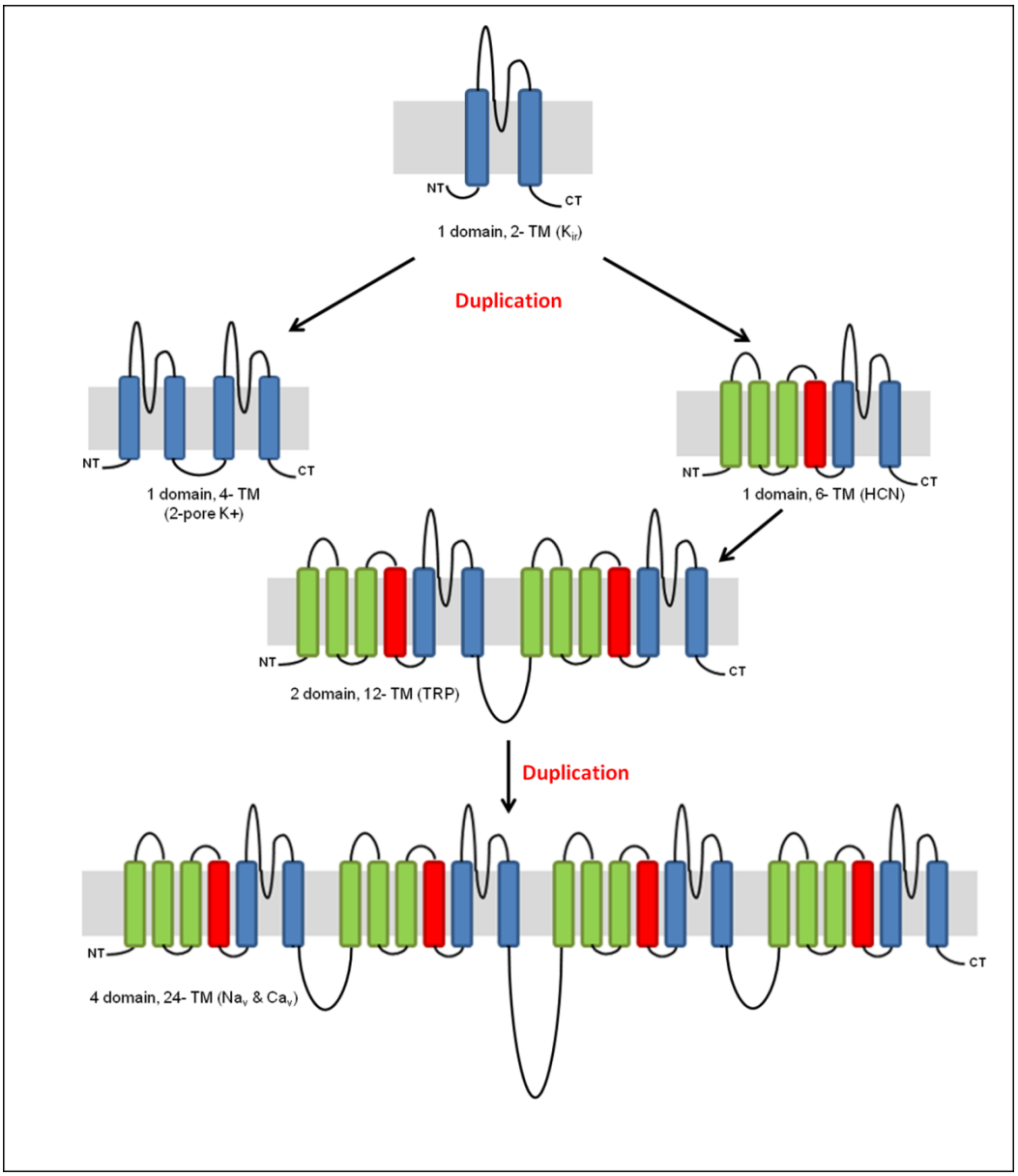

Figure 1.3 Evolutionary Diagram of Ion Channel Domains

A proposed diagram of the evolution of 4x6TM voltage-gated ion channels through two round of duplication of a 6-TM channel (e.g., K_v). From (Guan, 2014), adapted from (Strong et al., 1993)

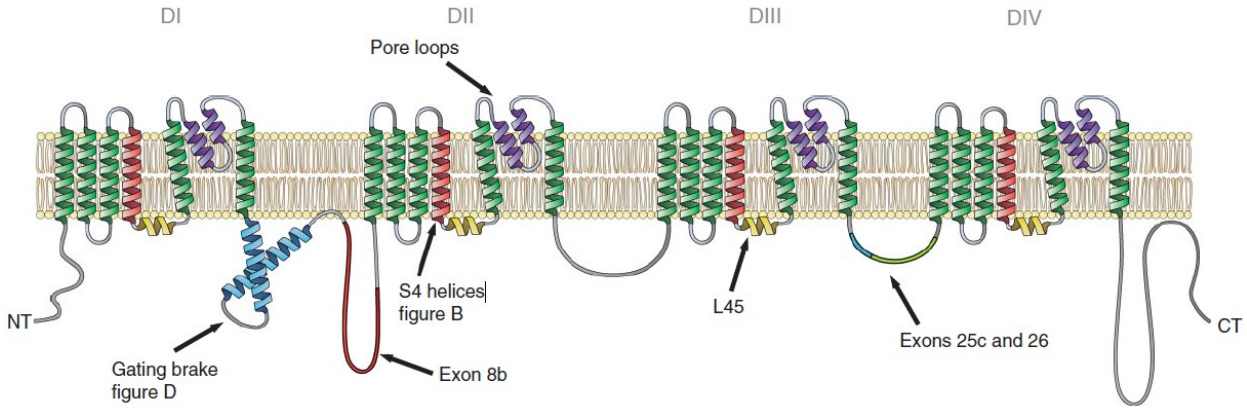

Figure 1.4 Structure of the Voltage-gated T-type Calcium Channel

The structure of the T-type calcium channel in the membrane displays critical features of 4x6TM channels, including 4 Domains (DI-DIV) each with 6 transmembrane segments (S1-S6). S1-S4 is the voltage sensor domain (VSD), and movements of the VSD are transmitted to the pore-domain (S5-P(pore-loop)-S6) via the S4-S5 linker. The pore loops create the narrow constricture point of the pore domain, and the S6 helices line the aqueous pore of the channel. From (Senatore et al., 2012)

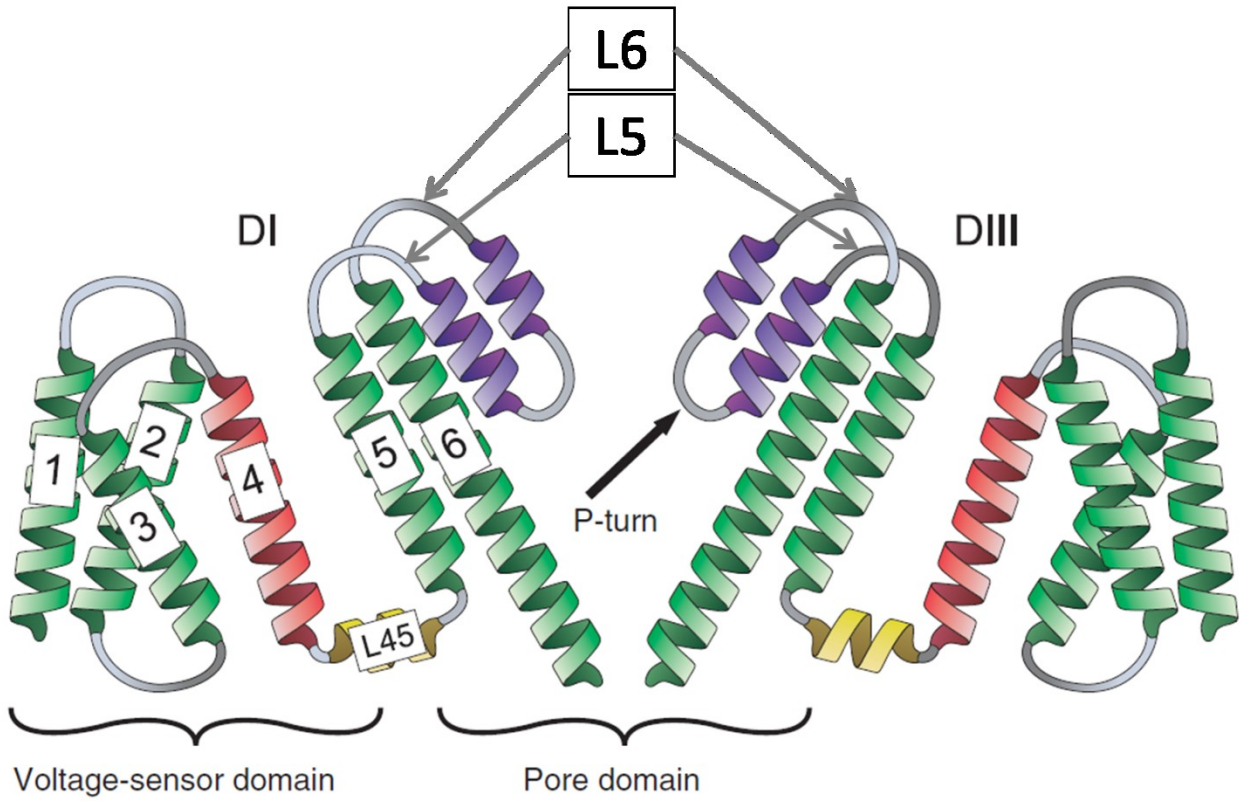

Figure 1.5 Folding of Domain I and Domain III in the Membrane

Folding of the Ca_v3 channel (see Figure 1.4) to highlight the projection of the P-loop into the channel pore, the position of the S6 helical bundles, and the S4-S5 linker (L45). The L5 and L6 (extracellular turret) regions are indicated. Only Domain I and Domain III are shown for clarity. The structural features of the Ca_v3 channels are elucidated from experimental results of Ca_v3 channels, from analysis of the primary sequence(s) of the Ca_v3 channels, and from structural data gathered from voltage-gated ion channels that are similar to Ca_v3 (see text for more details and references). From (Senatore et al., 2012).

IV Mechanisms of Ion Selectivity and Permeation

The research presented in this thesis will largely be concerned with the structural determinants of ion selectivity in T-type calcium channels. But before we can interpret the results presented herein, an understanding of the currently accepted mechanisms of ion selectivity in different kinds of channels is necessary. Much of what we know about ion selectivity and permeation has been conceived from the analysis of experimental data using various tissue preparations and cloned channels in electrophysiological recordings. Through interpretation of the results of various recordings in different conditions, permeation models were proposed. In 1998, the first voltage-gated ion channel was visualized as a crystal structure (Figure 1.9); the KcsA structure confirmed a permeation model that was proposed 20 years earlier, and shed light on the protein structures involved in ion selectivity and the permeation-pathways of ion channels (Doyle et al., 1998; Hille, 1975). Since that time, a number of other crystal structures of prokaryotic voltage-gated ion channels have been studied that have provided support for some long-standing theories of permeation through ion channels (Jiang et al., 2003, 2002b; Long et al., 2005; McCusker et al., 2011; Payandeh et al., 2011; Zhang et al., 2012). Eukaryotic voltage-gated ion channels from the Na_v and Ca_v families have been notoriously difficult to visualize with techniques in crystallography. Recently, cryo-electron microscopy has been used to visualize voltage-gated ion channels from the electric eel and rabbit skeletal muscle with some success (Sato et al., 2001; Wu et al., 2015; see Figures 1.19 and 1.21). Unfortunately, the pore structure cannot be determined with the cryo-EM images currently available. Until reliable structures are available, we turn to models of permeation determined experimentally and make comparisons with known structures of ion channels to elucidate mechanisms of ion selectivity in eukaryotic channels.

i Models of Permeation

First of all, it is important to define the term "permeability". Ionic permeability of a membrane is measured in three distinct ways: tracer flux measurements, conductance or current amplitude measurements, and reversal potentials (Hille, 1975). The term "permeability" is used to describe several different properties, and whenever this term is applied, the method used to determine the permeability will need to be taken into account. This will be important to keep in mind throughout the remainder of this thesis.

Prior to 1975, the Goldman-Hodgkin-Katz (GHK) equations were commonly used to relate permeability, ion concentration, membrane potential and current (Goldman, 1943; Hodgkin and Katz, 1949). Although useful under certain conditions, the GHK equations relied on assumptions of independence between ions. However, several studies indicate that ions compete with one another for permeation through the pore, and some ions are capable of blocking others at the channel pore.

In 1975, Bertil Hille published a groundbreaking paper in which he describes a permeability model for Na^+ ions moving through the membrane of myelinated axons (Hille, 1975). Based upon the fact that the independence principle is untrue under most conditions, Hille proposed a model in which the channel pore consists of saturable binding sites that create energy barriers for permeating ions, and used Eyring rate theory to describe the ion flux (Eyring et al., 1949; Hille, 1975). In Hille's model of the sodium channel pore within the myelinated axon, there are four energy barriers and multiple binding sites, and only one ion is allowed in at one time (Figure 1.6). Hille proposed the presence of an extracellular binding site, called the selectivity filter, which binds the cation of interest with particularly high affinity. Hille's

mechanism of permeation was supported by the crystal structure of Na_vAb (see Figure 1.10), described in 2011 (Payandeh et al. 2011).

In 1977, another Hille model was proposed that involved a multi-ion pore in potassium channels (Hille and Schwarz, 1978). This model indicated that the potassium channel's selectivity filter is made up of a linear sequence of binding sites and energy barriers. The pore was predicted to have at least three binding sites, and two ions could occupy the channel at a time (Figure 1.6). The K^+ ions hop in single file into vacant sites with rate constants that depend on barrier heights, membrane potential, and inter-ionic repulsion (Hille and Schwarz, 1978). Again, Hille's model was confirmed as an accurate representation of K^+ channels when the crystal structure of the KcsA potassium channel became available in 1998 (Doyle et al., 1998; see Figure 1.9).

Currently, there are no structures available that show the pore structure of voltage-gated calcium channels. For Ca_v channels, we rely on the interpretation of the channel's primary sequences, hydrophobicity analysis, and experimental results gathered in electrophysiological studies to elucidate their structures and mechanisms of permeation. In the mid-1980s, Tsien et al. and Almers and McCleskey noted the presence of an anomalous mole –fraction effect (AMFE) in preparations containing highly-calcium-selective L-type calcium channels (Almers and McCleskey, 1984; Tsien et al., 1987); when Ca^{2+} was introduced to channels being recorded in Na^+ solutions, the total whole-cell current decreased through a particular [Ca^{2+}] range, and then the current began to increase as [Ca^{2+}] became higher (See Figure 1.7). At first, the Ca^{2+} blocked the movement of the Na^+ ions through the channel pore and decreased the Na^+ current (and the total current), but as the [Ca^{2+}] increased a measureable calcium current became apparent (Figure 1.7). Tsien et al. and Almers and McCleskey interpreted the AMFE as an indication that the

calcium-channel pore contains two or more high-affinity binding sites that select for Ca^{2+}, and that Ca^{2+} occupancy of these sites guards the pore against permeation by other ions; this could explain how Ca_v channels achieve Ca^{2+} selectivity (Figure 1.7). Repulsion by Ca^{2+} ions coming into the pore may allow for the bound Ca^{2+} to flow through the channel, resulting in a Ca^{2+} flux (Figure 1.8). The AMFE has also been observed in T-type calcium channels, although the rate of block of the Na^+ current tends to be slightly less than that of the L-type channels (Kostyuk et al., 1984; Senatore et al., 2014; Shuba, 2014).

Currently there are two long-standing plausible mechanisms of calcium permeation and selectivity based on rate theory (Figure 1.8; Almers and Mccleskey, 1984; Dang and McCleskey, 1998; Ellinor et al., 1995; Friel and Tsien, 1989; Hess and Tsien, 1984; Hess et al., 1986; McCleskey, 1999; Sather and Mccleskey, 2003; Shuba, 2014; Tsien et al., 1987). The first theory is the ion-ion interaction theory, in which there are two high affinity binding sites. When two Ca^{2+} bind, the energy profile changes and the binding sites become low affinity; the repulsion between ions allows one Ca^{2+} to exit (Figure 1.8). The second theory is the stair-step mechanism. In this model, there are three binding sites: a single high affinity binding site (probably the selectivity filter) flanked by two lower-affinity sites. As extracellular concentration of calcium ions increases, the high affinity site becomes saturated and ions begin to overflow into the lower affinity sites. As a result rapid Ca^{2+}-selective flux occurs (Figure 1.8). A model proposed by Cheng et al. is similar to the stair-step mechanism and involves a highly conserved aspartate in Domain II ($D2_{p51}$) of the L-type calcium channel. The aspartate at $D2_{p51}$ acts as a molecular beacon, binding Ca^{2+} on the extracellular side of the pore (Cheng et al., 2010). An aspartate residue is found at this site in all voltage-gated calcium channels (i.e., Ca_v1, Ca_v2, and Ca_v3). An analogous structure in a pore-only derivative of BacNav Na_vAe1 was recently discovered (Shaya

et al., 2014). X-ray crystallography shows that this site does, indeed, bind Ca^{2+}. In electrophysiological studies, mutants lacking this "outer ion" beacon displayed reduced calcium affinity. Similarly, the residues of the extracellular turrets in T-type calcium channels could play a role in attracting calcium ions to the pore or providing an extracellular binding site for ions outside of the channel's pore.

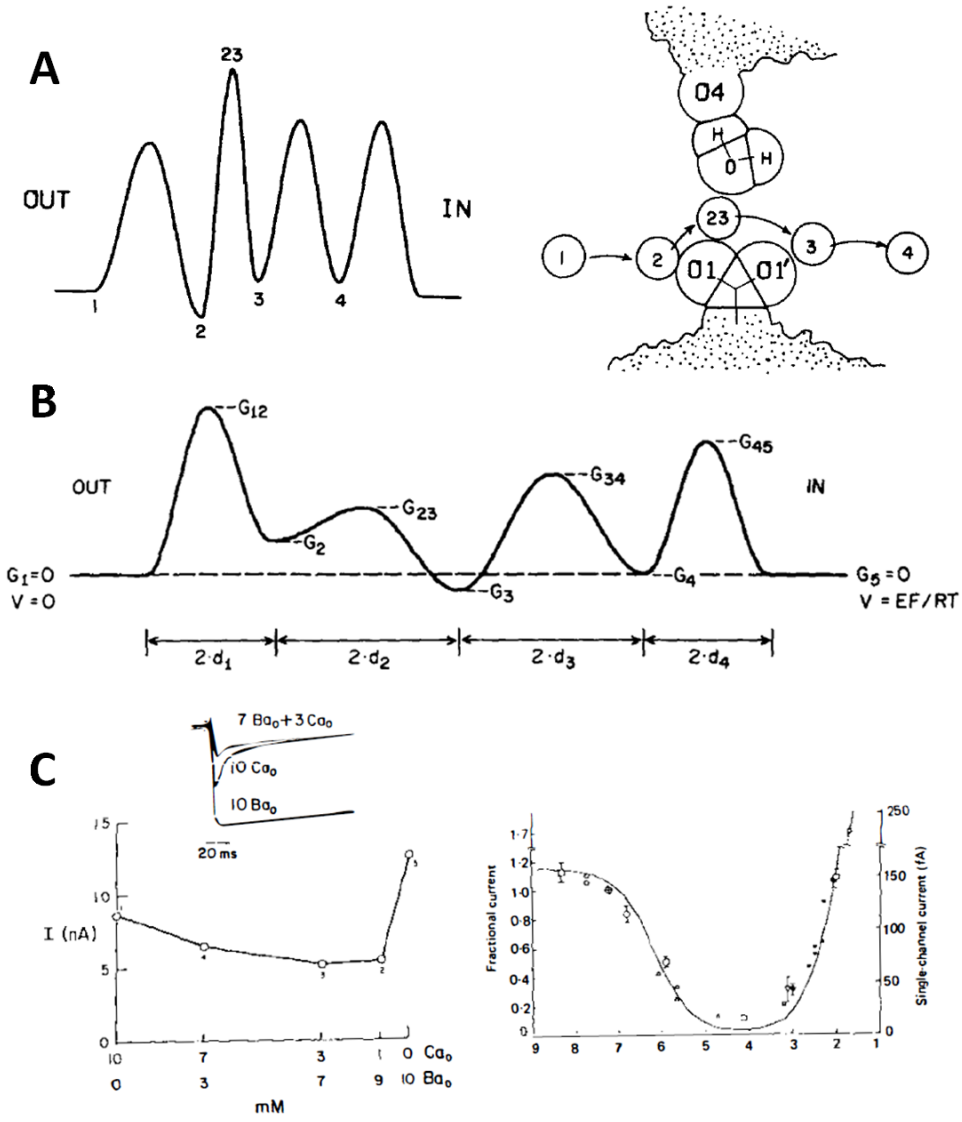

Figure 1.6 Models of Permeation: Occupancy, Binding Sites, and Energy Barriers

(A) Single-ion four energy barrier permeability model for Na^+ channels in myelinated axons proposed by Hille in 1975. (B) Multi-ion four energy barrier permeability model for K^+ channels proposed by Hille and Schwarz (1977). (C) Anomalous mole-fraction effect through cardiac Ca^{2+} channels and frog skeletal muscle Ca^{2+} channels, as observed by Almers and McCleskey and Tsien et al. This behaviour suggests that L-type Ca^{2+} channels have two ion binding sites with high affinity for Ca^{2+} and low affinity for monovalent ions, and when two Ca^{2+} ions bind they repel each other to allow for flux through the channel.

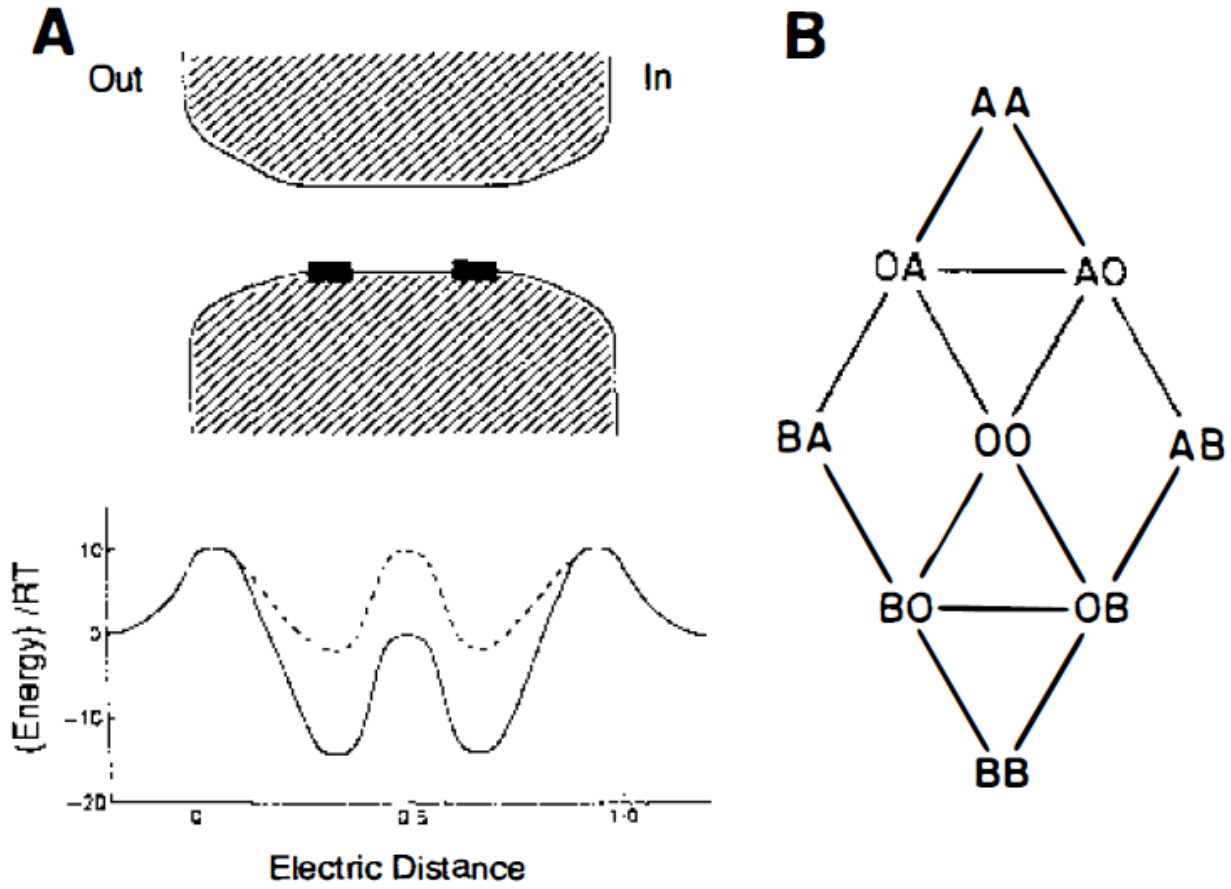

Figure 1.7 Model of Permeation through a Two-site Calcium Channel Pore

(A) *Above.* A cartoon of a calcium channel pore with two high-affinity Ca^{2+} channel binding sites. *Below*. Energy profiles for a Ca^{2+} ion (solid curve) and a Na^{+} ions (dashed curve) moving through the calcium channel pore. (B) All possible states of occupancy with two permeant ions, called A and B, in both intracellular and extracellular solutions where 0 indicates an empty site. From (Tsien et al., 1987).

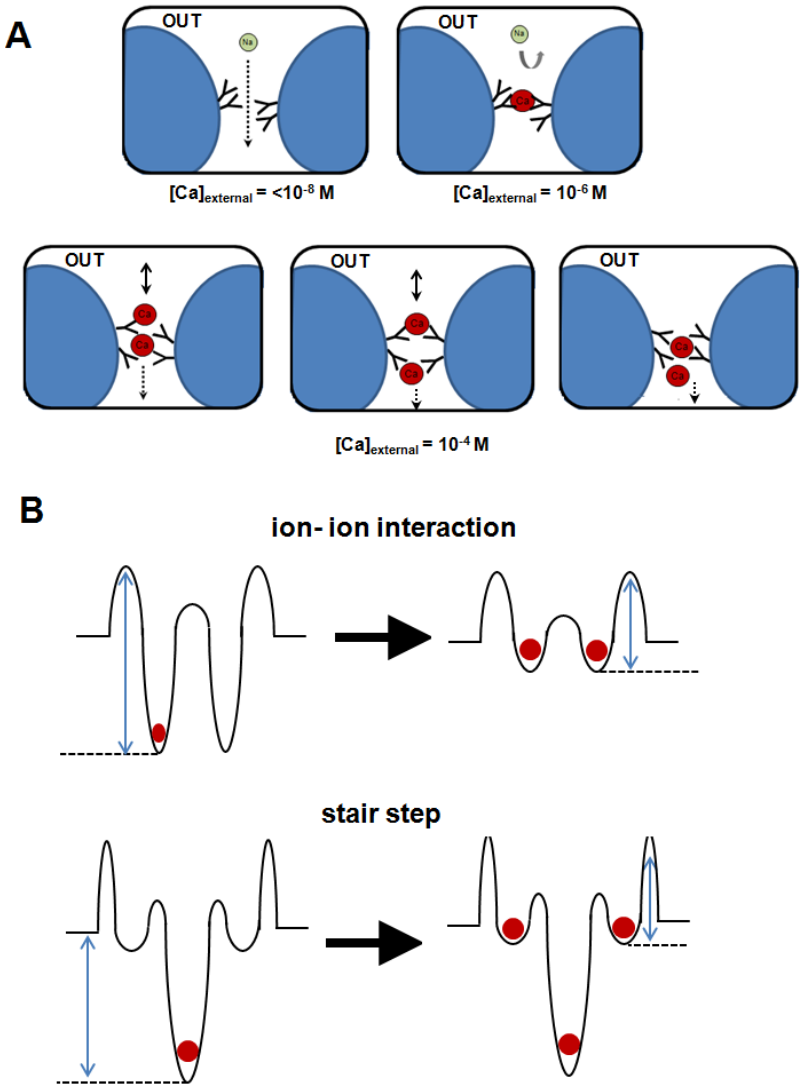

Figure 1.8 Current Theories on Ion Permeation and Selectivity

(A) In the presence of low-levels of Ca^{2+}, calcium channels will pass Na^{+} ions. However, as [Ca^{2+}] increases, Ca^{2+} will bind the pore and block Na^{+}. As more Ca^{2+} approaches the pore, the bound Ca^{2+} will permeate through the pore. This results in Ca^{2+} influx. (B) Ca^{2+} permeation could be accounted for by either the ion-ion interaction mechanism or the stair step mechanism. Shown here are energy diagrams for the two models. Ca^{2+} are shown as red spheres. From (Guan, 2014); adapted from (Shuba, 2014)

ii Structural Evidence to Support the Models of Permeation through Voltage-Gated Ion Channels

The research presented here involves exploring the function and structure of eukaryotic T-type calcium channels, which are categorized as a class of eukaryotic 4x6TM channels. However, the channels of prokaryotic organisms will also appear frequently in our discussions of ion selectivity.

Voltage-gated ion channels from prokaryotes have a different structure, consisting of four 1x6TM subunits. These channels can form homotetrameric structures or heterotetrameric structures (Anderson and Greenberg, 2001). Despite the differences between the eukaryotic 4x6TM channels and the homotetrameric 1x6TM channels from prokaryotes, there are many important similarities between them. In general, it is assumed that all voltage-gated ion channels from all kinds of organisms achieve ion selectivity using related strategies. Importantly, however, the selectivity filter of each channel is tuned to select the appropriate cation. There are important differences between the 4x6TM channels from eukaryotes and the prokaryotic multi-subunit channels. One important difference is the structural asymmetry of the pore in 4x6TM channels, which is absent in homotetrameric prokaryotic channels which possess four identical subunits. The structural symmetry in the pores of bacterial channels results in some obvious limitations when it comes to using prokaryotic channels as models for elucidating mechanisms of ion selectivity and permeation in eukaryotic ion channels. Nonetheless, studying bacterial channels provides important insights for ion selectivity.

Prokaryotic channels have been crystallized to provide insights into structures responsible for the functional behaviours of ion channels. There has been limited success with visualizing the

3-dimensional structures of eukaryotic 4x6TM voltage-gated ion channels, so we rely largely on functional comparisons and models derived from the structures of prokaryotic channels to draw conclusions about the mechanisms of ion selectivity in eukaryotic ion channels. Therefore, an understanding of the mechanisms of selectivity and models derived from both prokaryotic and eukaryotic channels is important in accomplishing the objectives of this thesis. For the most part, the structure of the pore domain (PD) will be discussed to highlight key residues involved in ion selectivity.

iii Ion Selectivity and the Pore Domain

Interestingly, the pore-domain (PD) and voltage-sensing domain (VSD) are semi-autonomous. Some voltage-sensing and pore-forming modules exist as natively expressed stand-alone proteins. One such example is the bacterial KcsA potassium channel, a pH-activated protein that has only the pore modules (Doyle et al., 1998). Truncated subunits of bacterial sodium channels can form *in vitro* functional tetramers without the voltage-sensor domains (McCusker et al., 2011; Shaya et al., 2014; Tsai et al., 2013). There is also a voltage-sensor domain containing phosphatise from *Ciona intestinalis*, called Ci-VSP (Murata et al., 2005). In the 4x6TM channels, the VSD and PD are combined to form a fully functional voltage-gated ion channel.

The pore-domain (PD) is critically important in ion selectivity. Each channel is able to preferentially select particular ion(s) with high affinity and probability, and the residues within the PD are essential for this function. The outer vestibule is made up of S5 and S6 linkers that contain an outer turret, descending helix, a selectivity filter and an ascending helix (See Figures

1.5 and 1.21). The extracellular turret (L5 portion) emerges from the S5 transmembrane helix and then descends into the pore with a descending pore helix, which then turns upwards to a selectivity filter residue. From the selectivity filter residue, there is an ascending pore helix (which creates a loop called L6). Together, the L5-P-L6 structure generates a hairpin shaped P-loop (Catterall, 2000; Hille, 2001; Senatore et al., 2012). The L5 and L6 regions will be particularly important to this thesis (see Figures 1.5 and 1.21).

In general, four residues of the channel contribute to the selectivity filter to determine the K^+, Ca^{2+}, Na^+, or mixed ion selectivity, and divide the ion permeation pathway into an outer pore above and the inner pore below the selectivity filter. The selectivity filter, discussed in the next subsection, is a critical determinant of ion selectivity in all known voltage-gated ion channels.

iv The Role of the Selectivity Filter: Evidence from Crystal Structures

(a) Ion Selectivity in Potassium Channels

Published in 1998, work completed in Roderick Mackinnon's laboratory provided a foundation for understanding the mechanisms of ion selectivity in voltage-gated ion channels (Doyle et al., 1998). The crystal structure of the bacterial potassium channel KcsA from *Streptomyces lividans* indicated a selectivity filter of carbonyl backbones that line the pore of the potassium channel and convey potassium selectivity on the channel (Figure 1.9). The selectivity filter sequence of KcsA is TVGYG, and it is the carbonyl backbone of these residues that line the narrow constricture point of the channel's pore. This narrow pore has five binding sites for potassium (S0-S4) with S0 occurring at the channel's mouth and S1-4 inside the pore. Potassium

ions can occupy every other position in the selectivity filter. So at one time, potassium ions might be bound to positions S0, S2, and S4 or they might be bound to S1 and S3 (Figure 1.9). The driving force and the ion-ion repulsive interactions within the pore allow the potassium ions to flow through the pore in single-file (Nimigean and Allen, 2011).

In general, potassium channels are highly selective for potassium ions. The selectivity filter contributes to this high degree of selectivity. Although sodium ions (Na^+, 0.99 Å ionic radius) and potassium ions (K^+, 1.37 Å ionic radius) are quite similar in radius and charge, the KcsA channel is able to select for K^+ over Na^+ at a ~1000:1 ratio (Noskov and Roux, 2006). This is due to the shape and size of the KcsA selectivity filter. Upon entering the pore of the potassium channel, the hydration shell of K^+ is completely replaced by coordination with the carbonyl oxygen molecules within the selectivity filter in an energetically favorable reaction (Doyle et al., 1998). The sodium ions, on the other hand, cannot be favorably dehydrated by the carbonyl oxygen molecules within the selectivity filter (Payandeh et al., 2011; Stephens et al., 2015; See Figure 1.10). Ion selectivity based on complete or partial dehydration in a favorable step seems to be a common strategy employed by voltage-gated ion channels.

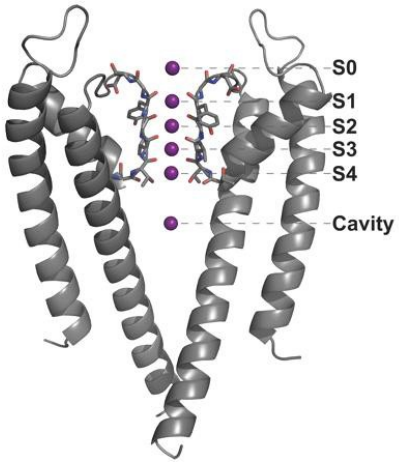

Figure 1.9 Side View of the KcsA Channel Pore with K+ Binding Sites Indicated

There are 5 binding sites (S0-S4). S0 is located extracellularly and S1-S4 are intracellular. K^+ becomes dehydrated upon entering the inner cavity and binds to the selectivity filter's carbonyl oxygen atoms. A traditional outward K^+ current migrates from the pore cavity 'transitioning from positions S1-S3 and S2-S4 binding sites as a dehydrated ion and then rehydrated at position S0 on the extracellular side of the channel pore. Subunits 2 and 4 shown for clarity. Reproduced from (Nimigean and Allen, 2011)

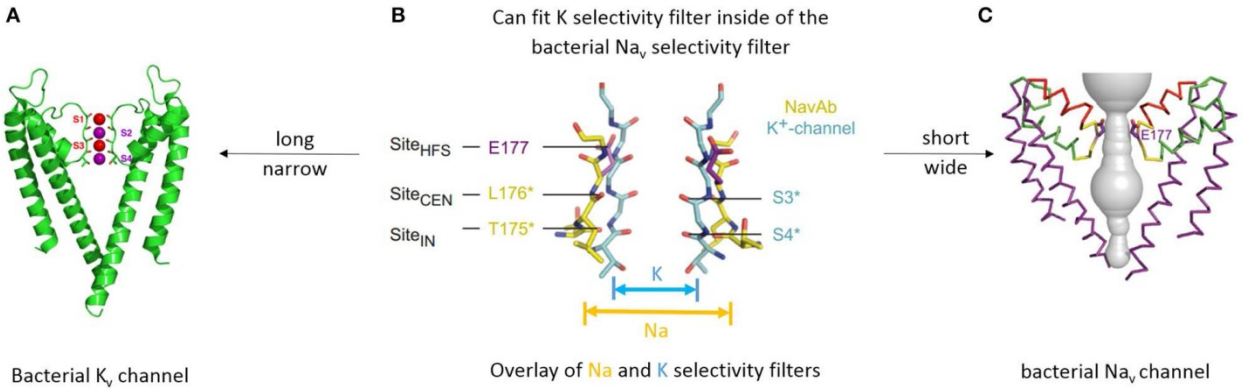

Figure 1.10 Different Structures Underlying Different Mechanisms of Selectivity in Potassium and Sodium Channels

(A) Bacterial K_v channel. See Figure 3. (B) The narrow K_v channel pore fits into the pore of the bacterial NaChBac channel, Na_vAb. The selectivity filter of the K_v channel consists of backbone carbonyl oxygen atoms from the residues of the selectivity filter, whereas the glutamate residues (E177) make up the selectivity filter of the broader Na_vAb channel. The broad Na^+ cannot pass through the K_v channel, whereas K^+ ions are completely dehydrated by the K_v channel pore. (C) Side view of the Na_vAb channel, showing the pore-loops creating the HFS site of the Na_vAb channel (E177 residues). In each, only 2 subunits are shown for clarity. (B,C) Reproduced from (Payandeh et al., 2011)

(b) Ion Selectivity in Prokaryotic Sodium channels

Prokaryotic sodium-selective voltage-gated ion channels have been crystallized and studied (Figure 1.10). The first prokaryotic sodium channel to be crystallized is from *Arcobacter butzleri,* and is referred to as Na_vAb. The structure of Na_vAb reveals a homotetrameric channel with a selectivity filter composed of four glutamate residues (EEEE) within the P-loop (Payandeh et al., 2011). Soon after, other prokaryotic sodium-selective channel structures were determined and follow a similar strategy for sodium selectivity (McCusker et al., 2011; Zhang et al., 2012). Prior to the crystallization of sodium channels, the importance of the selectivity filter residues within the P-loops was established with the NaChBac channel from *Bacillus halodurans* (Ren et al., 2001; Yue et al., 2002; Zhang et al., 2012).

The strategy employed for sodium selectivity in the prokaryotic sodium channels is markedly different from the strategy of K^+ selectivity in KcsA (Doyle et al., 1998; Payandeh et al., 2011). Most notably, the Na^+ ions seem to move through the pore in a mostly hydrated from, whereas K^+ ions are fully dehydrated by the KcsA selectivity filter (Figures 1.9 and 1.10). In describing the movement of Na^+ ions through the Na_vAb pore, Payandeh et al. divided the permeation-pathway into three parts, named $Site_{HFS}$, (the high-field-strength site), $Site_{CEN}$ (the central site), and $Site_{IN}$ (the intracellular site). The relative locations of these sites can be seen in Figure 1.10. A partially-dehydrated Na^+ ion can coordinate with $Site_{HFS}$ through interactions with the glutamate residues (E177); the E177 side-chain of one subunit interacts with the Na^+ ion directly, while the E177 side-chains from the other subunits participate in hydrogen-bonding with the surrounding water molecules. This transition complex is inherently asymmetric. When the Na^+ ion escapes the $Site_{HFS}$ (presumably repelled by an incoming Na^+ ion), the permeating

Na^+ ion is fully rehydrated as it moves through $Site_{CEN}$ and $Site_{IN}$. This permeation mechanism probably reflects the high free energy of Na^+ hydration, where further removal of solvating waters would present too high an energy barrier.

The mechanisms for sodium selectivity in prokaryotic sodium channels are not fully understood, but mutating the LESWAS selectivity filter (resulting in an EEEE site in the fully-formed channel) of the homotetrameric NaChBac channel from *Bacillus halodurans* to LDDWAS results in reduced sodium selectivity and increased Ca^{2+} permeation (Yue et al., 2002). A similar mutational study involved substituting glutamate residues for aspartate residues in the selectivity filter of Na_vAb, and the results were consistent i.e. Ca^{2+} permeability increased (Tang et al., 2014). The EEEE ring forms the narrowest level of the open pore with the flexible carboxylate side chains facing toward the pore axis. The conformational flexibility of the carboxylate side chains stabilizes multiple ionic occupancy states, helping sodium ions to pass through the selectivity filter via the knock-on mechanism (Chakrabarti et al., 2013; Tang et al., 2014). Computations of 2-D PMFs suggest that the degree of ion stabilization in two of the three proposed binding sites present in the EEEE filter of the wild-type Na_vAb channel are significantly affected by mutation to DDDD (Finol-Urdaneta et al., 2014); the destabilization caused by the DDDD mutation contributes to less Na^+ selectivity and higher K^+ permeation.

Interestingly, the selectivity filter of the prokaryotic sodium channels is similar to the selectivity filter of the highly-calcium-selective eukaryotic Ca_v1/Ca_v2 channels; these channels both have a ring of glutamate residues at their high field strength (HFS) constricture point created by the P-loops (EEEE; see Figure 1.11). Despite their resemblance to Ca_v1/Ca_v2, prokaryotic sodium channels are able to select for sodium with high probability (Figure 1.11). There are differences between the Na_vAb and Ca_v1/Ca_v2 channel pores; in particular, the Ca_v

channels all seem to have an extra negatively charged aspartate residue in Domain II (i.e., D2p51). Nonetheless, the similarities between prokaryotic Na_vs and eukaryotic Ca_vs suggest that we should look outside of the HFS to explain Na^+ versus Ca^{2+} selectivity in these channels. Experimental studies and computational work involving molecular dynamics (MD) and 1- and 2-D potentials of mean force (PMF) suggest that the bacterial sodium channels are similar to eukaryotic Na_vs in terms of selectivity and ion conduction, although ion interactions within the pore and occupancy are more like those of eukaryotic Ca_v and K_v channels (Finol-Urdaneta et al., 2014). To understand the mechanisms of ion selectivity within these channels with certainty, structural data for the Ca_v1/Ca_v2 channels will be required.

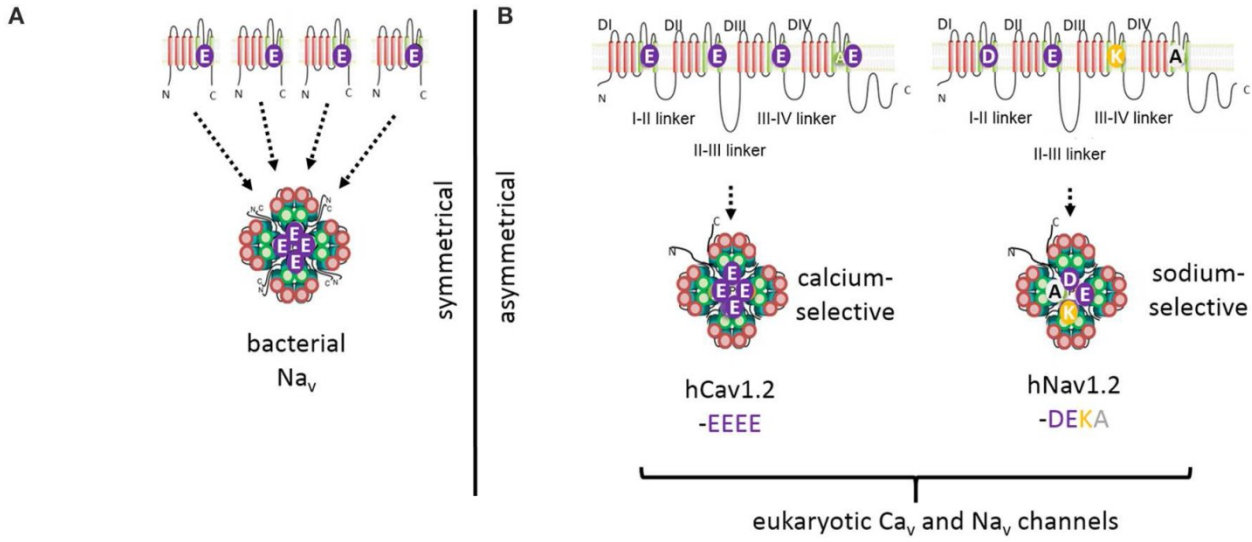

Figure 1.11 High Field Strength (HFS) sites of Prokaryotic Na_vAb and Eukaryotic $Ca_v1.2$ and $Na_v1.2$

The High Field Strength (HFS) site EEEE formed by selectivity filter glutamates (E177) in the homotetrameric bacterial sodium channel Na_vAb is equivalent to the EEEE site in Ca_v1 and Ca_v2 calcium channels, and different from the eukaryotic Na_v1 channel HFS of DEKA (A) Residues to the EEEE HFS site in bacterial sodium channels are contributed by four identical gene products. (B) Residues to asymmetric selectivity filters in eukaryotic calcium and sodium channels are contributed by four homologous repeat domains. From (Stephens et al., 2015)

(a) Selectivity Filter Residues in Eukaryotic Sodium and Calcium Channels

The selectivity filters of eukaryotic 4x6TM voltage-gated ion channels occur within the P-loop of the pore domains, at the narrowest level of the open pore. In the eukaryotic Na_v1 channels, the selectivity filter residues are DEKA, arranged around the narrow opening (Figure 1.11). The protonatable lysine (K) in the third repeat and a neutral alanine (A) in the fourth position seem to be critical for sodium selectivity (Favre et al., 1996; Grigoriev et al., 1996; Lipkind and Fozzard, 2008; Spafford et al., 1998). This arrangement is highly conserved in eukaryotic Na_v1 channels, with the exception of cnidarians, which possess a DKEA ring (Spafford et al., 1998). The critical importance of the selectivity-filter residues was established in experiments where the DEKA ring in the $Na_v1.2$ channel was replaced by the EEEE ring to create calcium-selective channels (Heinemann et al., 1992; Schlief et al., 1996; Sun et al., 1997). Na_v1 channels likely evolved as an offshoot of calcium-selective Na_v2 channels, which possess a selectivity filter of DEEA or DEES (Gur Barzilai et al., 2012; Zhou et al., 2004). Notice that these Na_v2 channels are missing the critical lysine residue.

The HFS site of the Ca_v1 and Ca_v2 calcium channels is a highly conserved arrangement of four glutamate residues (EEEE; See Figure 1.10). This negatively charged HFS site allows for extremely high calcium selectivity (See Figure 1.16). The related Ca_v3 channels, however, possess a selectivity filter in which aspartate residues have replaced glutamate residues in the third and fourth repeats (EEDD; see Figures 1.13 & 1.14). The channels of the Ca_v3 family display ~10-fold less calcium-selectivity over sodium compared to the Ca_v1 and Ca_v2 channel (Shcheglovitov et al., 2007; Shcheglovitov and Shuba, 2006; Shuba, 2014). T-type channel isoforms also display wide variability in calcium- over sodium-selectivity. For example, among

the human T-type channel isoforms, $Ca_v3.1$ is the most sodium impermeant and $Ca_v3.3$ is least sodium impermeant (Shcheglovitov et al., 2007). The EEDD selectivity filter may contribute to the differences between Ca_v1/Ca_v2 channels and Ca_v3 channels in terms of calcium- over sodium-selectivity.

NALCN channels are related to the Na_vs and Ca_vs, but they are non-voltage activated. They possess a 4x6TM channel structure highly similar to the Na_vs and Ca_vs, but the NALCN channels possess HFS sites that resemble either calcium channels (EEEE) or sodium channels (EEKE and EKEE; See Figure 1.12). For example, NALCN channels in basal multicellular organisms (sponge, placozoan and cnidarians) and non-vertebrate chordates (the cephalochordates) possess an EEEE HFS site (Senatore et al., 2013). However, in other animals, NALCN channels resemble sodium channels with a lysine in Domain II or III of the HFS site, respectively. Examples include the EKEE ring in schistosome flatworms and Helobdella leech and the EEKE ring in non-myriapod arthropods and vertebrates (Senatore et al., 2013). A separate group of non-vertebrates retain dual calcium channel and sodium channel character at the HFS site, through mutually exclusive splicing, and these evolved completely independently in at least two different animal lineages. Almost all lophotrochozoan invertebrates (mollusks, annelids) and non-vertebrate deuterostomes (echinoderms, hemichordates) possess two forms of exon 15 in their expressible NALCN transcripts, generating alternative calcium HFS site (EEEE) with exon 15a or a sodium HFS site (EKEE) with exon 15b (Senatore et al., 2013). The presence of alternative splicing in these animals, which may contribute to a switch from calcium- to sodium- selectivity by altering the HFS, provides support to the argument that the HFS site is of critical importance in ion selectivity in 4x6TM channels (Figure 1.12).

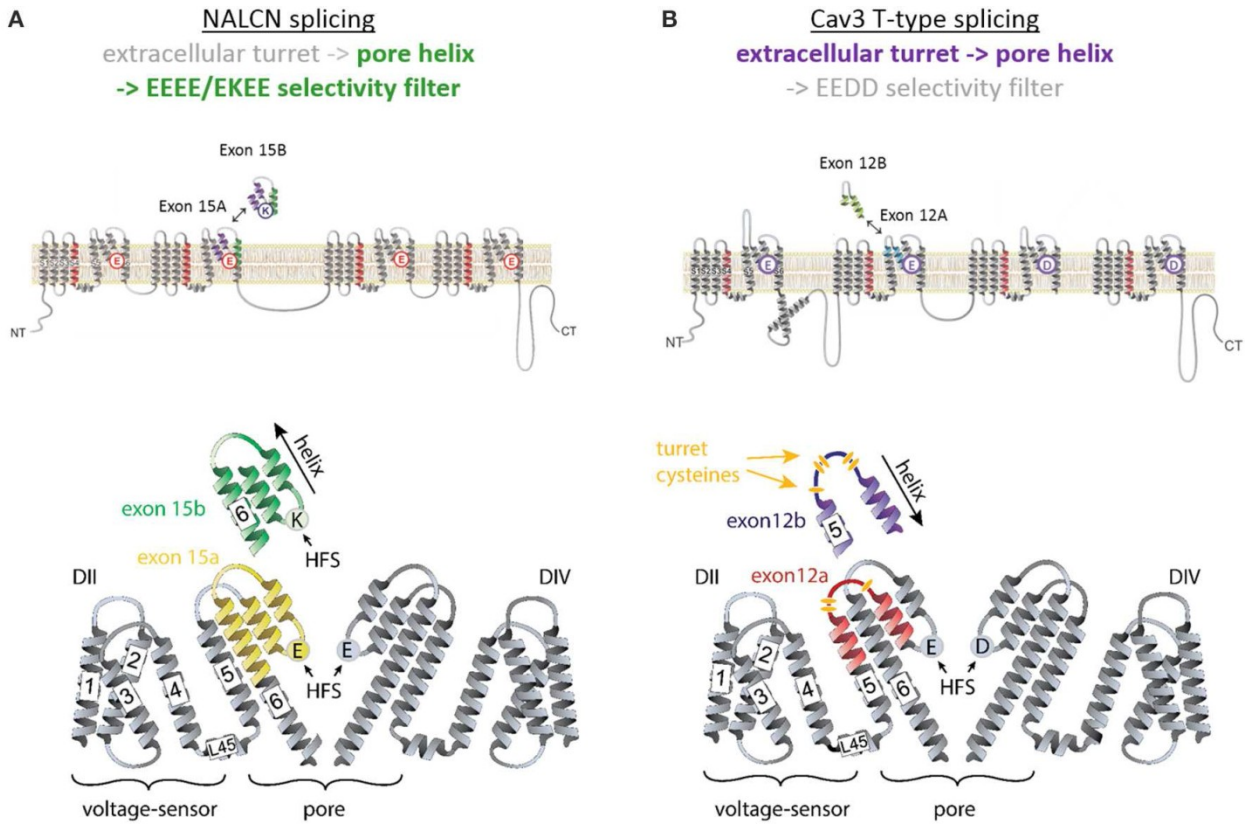

Figure 1.12 Alternative Splicing in NALCN and LCav3 Channels in the Pore Domains (PD) of Domain II (DII) Alters Ion Selectivity

(A) NALCN displays alternative splicing in the pore domain of Domain II, in exon 15, which contains the high field strength site (HFS). The two alternative isoforms are exon 15a and exon 15b. With exon 15a, NALCN has an HFS of EEEE and displays Ca^{2+} selective character. With exon 15b, NALCN has an HFS of EEKE and displays Na^{+} selective character. (B) LCa_v3, from *Lymnaea stagnalis*, displays alternative splicing in exon 12 (the turret), which occurs just upstream of the HFS site and does not include the HFS residues. With exon-12a, LCa_v3-12a passes sodium current. With exon 12b, LCa_v3-12b displays a mixed Ca^{2+}/Na^{+} current. The turrets of LCa_v3-12a and LCa_v3-12b differ in length and cysteine contribution. From (Stephens et al., 2015)

v Extracellular Loops (Turrets) as Determinants of Ion Selectivity

As mentioned previously, there is a wide variability among T-type channel isoforms in their calcium- over sodium-permeability, even though they all possess the HFS site of EEDD in their selectivity filters. Also, the EEDD-possessing Ca_v3 channels are ~10-fold less selective for calcium over sodium as compared to their Ca_v1 or Ca_v2 relatives with EEEE HFS sites. Paradoxically, mutating the EEDD filter in T-types to EEED, EEDE, or EEEE creates T-types that are less, not more, selective for calcium (Park et al., 2013; Senatore et al., 2014; Talavera et al., 2003, 2001). Thus, it appears that the selectivity filter is not the only determinant of ion selectivity in T-type Ca^{2+} channels. Recent studies have indicated that another extracellular loop between S5 and the P-loop (see Figure 1.5), dubbed the turret (L5-P-L6), plays a critical role in ion selectivity (Senatore et al., 2014). Further analysis (preliminary to the analysis included in this thesis) suggests that other turrets, possibly the turret from Domain IV, could reasonably be involved in ion selectivity in T-type channels.

The results of experiments conducted in the Marban lab have explored the role of P-loop residues outside of the selectivity filter in Na_v1 sodium channels. The Marban group found that the introduction of cysteine residues within the extracellular turret region affects the pore properties of Na_v1, including sensitivity to TTX and Cd^{2+} block (Bénitah et al., 1996), and that neutralizing negative charges within the extracellular P-loop region reduces the size of currents that are conducted by Na_v1 channels (Li et al., 2000). The results of the Marban experiments suggest that it is reasonable to explore the role of P-loop residues outside of the selectivity filter and their influence on pore properties. Furthermore, the role of the extracellular turrets in

determining ion selectivity may not be unique to T-types, and instead might extend to Na_v1 channels as well.

(a) The Role of the Domain II Extracellular Turrets (S5P) in the Ion Selectivity of the T-type Calcium Channel from *Lymnaea stagnalis*

Recent studies have indicated that another extracellular structure between S5 and the P-loop, dubbed the turret, plays a critical role in ion selectivity (Guan, 2014; Senatore et al., 2014). In the great pond snail *L. stagnalis* the turret region of LCa_v3 resides within an alternatively spliced exon, termed exon 12, generating exon 12a and alternative exon 12b (see Figures 1.13 & 1.14). The resultant splice isoforms are referred to as LCa_v3-12a and LCa_v3-12b. LCa_v3- 12a is highly sodium permeant; LCa_v3- 12b, however, is much less sodium permeant (see Figure 1.14). The striking differences between exon 12a and 12b (Figure 1.13) is that exon 12b has a penta-cysteine structure C...CxC...CxC (most protostomes) or CxxC…C…CxC (some nematodes) and is always longer (range: 48 to 55 aa long, average = 52 aa) than exon 12a, which is shorter (38 to 46 aa long, average = 41 aa) with a nearly invariant tri-cysteine structure: CxxC…C. Human Ca_v3 channels (Figure 1.13) also have a short exon 12 (38 or 39 aa long) with a single cysteine (Senatore et al., 2014). Intervening residues between the cysteines can be highly variable even amongst closely related invertebrate species with T-type channels; this suggests that the key structural features of exon 12a and exon 12b, which govern the ion selectivity differences, is their differing arrangements of cysteines and their turret sizes (Stephens et al., 2015).

(b) The Extracellular Loops (Turrets) of Domain II and Domain IV

The turrets in Domain II and Domain IV may play a critical role in ion selectivity in the T-type channels from other organisms as well. Some jellyfish species have two splice isoforms in Domain IV (Figure 1.15). Domain II and Domain IV may be related as products of the same duplication event (Figure 1.6) and are highly conserved in cysteine composition (Figure 1.18), so it might be reasonable to hypothesize that the Domain IV splice isoforms are contributing to changes in ion selectivity as well (Figure 1.15). Moreover, the Domain IV turret splice isoforms in jellyfish also differ from one another based upon their length and cysteine composition.

Interestingly, T-type calcium channels have uniquely cysteine-rich extracellular loops. In general, the cysteine arrangement of extracellular loops in the 4x6TM ion channels is 4-0-2-2 (DI-DII-DIII-DIV, respectively). With the exception of T-types and some vertebrate sodium channels, this 4-0-2-2 arrangement is highly conserved in 4x6TM channels. In T-types, however, the turrets are enriched with 8 to 14 additional cysteine residues. For example, the LCa_v3-12a and LCa_v3-12b turret cysteine arrangements are 6-3-2-6 and 6-5-2-6, respectively. In human Ca_v3 channels the cysteines are arranged as 6-1-2-4 in Cav3.1 and Cav3.2, and 7-1-2-4 in $Ca_v3.3$ (Figure 1.16 and 1.17). Although all known T-types are enriched with cysteines, there are marked differences between the cysteine arrangements of vertebrate T-type DII/DIV and invertebrate T-type DII/DIV turrets (Figures 1.16 and 1.18). The calcium versus sodium selectivity of vertebrate and invertebrate channels is also markedly different, although they share the same EEDD selectivity filter. Perhaps, the differences between the vertebrate and invertebrate turret structures can help to explain the differences in ion selectivity between these channels.

Aside from the cysteine composition of these turrets, their length may be critical in influencing ion selectivity. As mentioned above, LCa_v3-12a and LCa_v3-12b are different in length. LCa_v3-12b is longer (range: 48 to 55 aa long, average = 52 aa) than exon 12a (38 to 46 aa long, average = 41 aa). In Figure 1.16, we see relative lengths of the turrets from prokaryotic and eukaryotic voltage-gated ion channels. In general, voltage gated ion channels from eukaryotes have elongated turret structures compared to prokaryotes. Furthermore, there is asymmetry in the lengths of the 4x6TM eukaryotic turret sequences, which is absent in the prokaryotic channels. The elongation of Domain I and Domain III turrets is striking, especially compared to the turrets of prokaryotes (Figure 1.16). The turrets of Domain II and Domain IV, however, are consistently shorter than those of Domain I and Domain III (although longer than the turrets of most prokaryotic channels). This places most of the residues within the Domain II and Domain IV turrets closer to the pore, in a position which allows them to influence ion selectivity. There is some evidence to suggest that the turrets are playing particular roles, and some have suggested that the turrets may be involved in attracting Ca^{2+} ions to the pore or acting as a pre-filter for ions (Miller and Long, 2012; Wu et al., 2015).

(c) Extracellular Loops of Some Prokaryotic and Eukaryotic Ion Channels Appear to Contribute to Structures above the Channel Pore

In 2001, Sato et al. were able to produce a cryo-EM image (19 Å resolution) of the sodium channel from *Electrophorus electricus* (Sato et al., 2001). This image revealed that the sodium channel is a bell-shaped structure with a narrow extracellular upper region above the pore cavity (Figure 1.19). This region likely corresponds to the collection of extracellular turrets

from Domains I-IV. Although it is difficult to draw any conclusions from this image due to the limited resolution, the top-down view appears to support the idea that the extracellular regions (i.e., the turrets) are in a position to influence ion selectivity, either by binding ions above the selectivity filter (like a pre-filter) or influencing the residues of the selectivity filter.

In 2012, the structure of the human two-pore domain potassium channel, K2P1, was resolved at a resolution of 3.4 Å (Miller and Long, 2012). An extracellular structure extends from the turret above the pore, creating a large extracellular cap domain (Figure 1.20). This extracellular structure consists of an extended turret domain of 59 amino acids in the first of two pore domains in these channels, which is ~5 fold larger than a typical Shaker potassium channel, or the second of two pore domains in K2P1 channels. The dimeric K2P1 channel structure is capped at its apex, with conserved cysteines from the two extended turrets forming a disulphide bridge which contributes to a helical cap that emerges 35 Å above the plasma membrane and encloses the transmembrane pore below (Figure 1.20). The extracellular cap of the K2P1 channel creates an ion pathway that is different from those observed for other K^+ channels. The 3-dimensional structure suggests that ions are funneled through side portals lined by negative charges, formed by the helical cap. Thus, as suggested by Miller and Long, the K2P1 channel may be an example of extracellular turrets influencing ion selectivity in a human ion channel (Miller and Long, 2012).

In December 2015, a cryo-EM structure of the human calcium channel complex $Ca_v1.1$ was published (Wu et al., 2015). In this structure, the elongated DI and DIII turrets (i.e., $L5_I$ and $L5_{III}$) protrude extracellularly, and are involved in docking of the $\alpha_2\delta$ subunit. The Domain II and Domain IV turrets, however, are near the channel pore and are probably not involved in docking of subunits. Instead, they could be involved in ion selectivity and channel functions at the pore.

The Domain II extracellular loop, $L5_{II}$, is quite short and appears to be facing the central axis of the channel just above the pore (Figure 1.21). The Domain IV turret is longer, with a surprisingly long $L6_{IV}$ extracellular loop. The $L5_{II}$, $L5_{IV}$, and $L6_{IV}$ loops are positioned in a way that might allow them to influence ion selectivity. A model for a proposed mechanism of the $L5_{II}$ and $L5_{IV}$ regions' influence on ion selectivity involves a highly conserved aspartate near the HFS site, dubbed $D2_{P51}$ (See Figures 1.23 and 1.24).

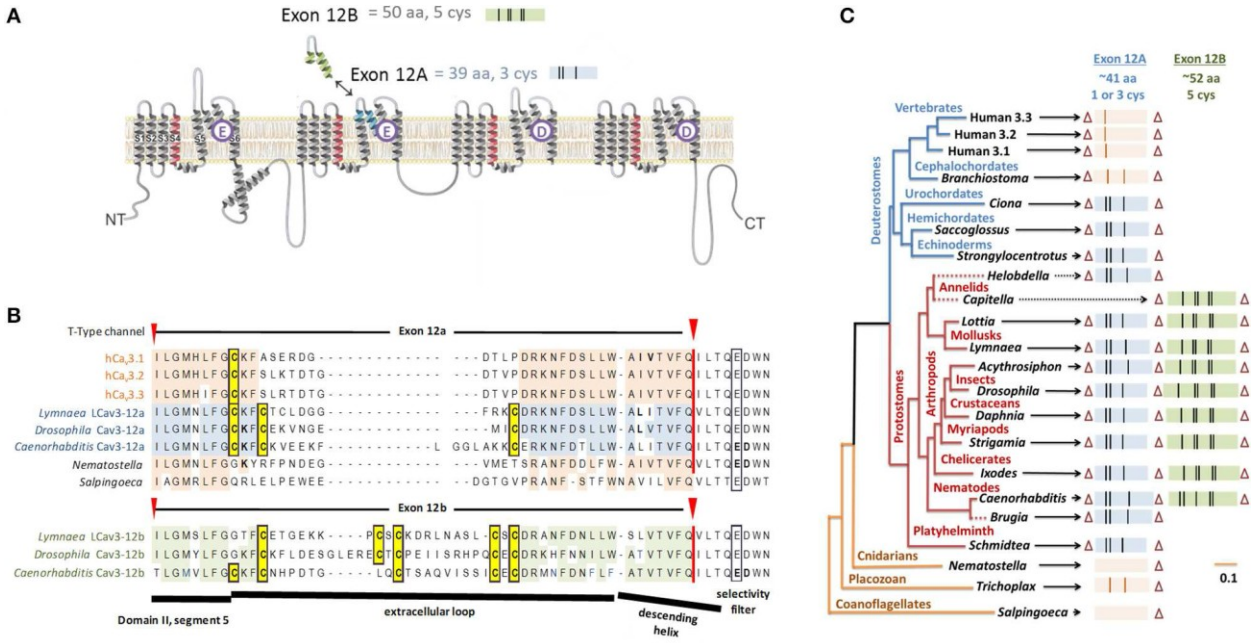

Figure 1.13 Cysteine-Rich Extracellular Turrets in Domain II of Cav3 T-type Channels Influence Ion Selectivity

LCa$_v$3, the T-type calcium channel from *Lymnaea stagnalis*, has alternative splicing in exon 12. This is the location of an extracellular turret in Domain II (A). LCa$_v$3-12a passes sodium currents, wheras LCa$_v$3-12b passes mixed calcium/sodium currents like the Ca$_v$3 channels from mammals (Ca$_v$3.1, Ca$_v$3.2, Ca$_v$3.3). Exon-12a 3 cysteines and is a shorter sequence, whereas LCa$_v$-12b is a longer sequence with 5 cysteine residues (B). Many other invertebrates also have two versions of exon 12, a tri-cysteine version and a penta-cysteine version. Humans have a unicysteine structure in their Domain II turret (C). From (Stephens et al., 2015)

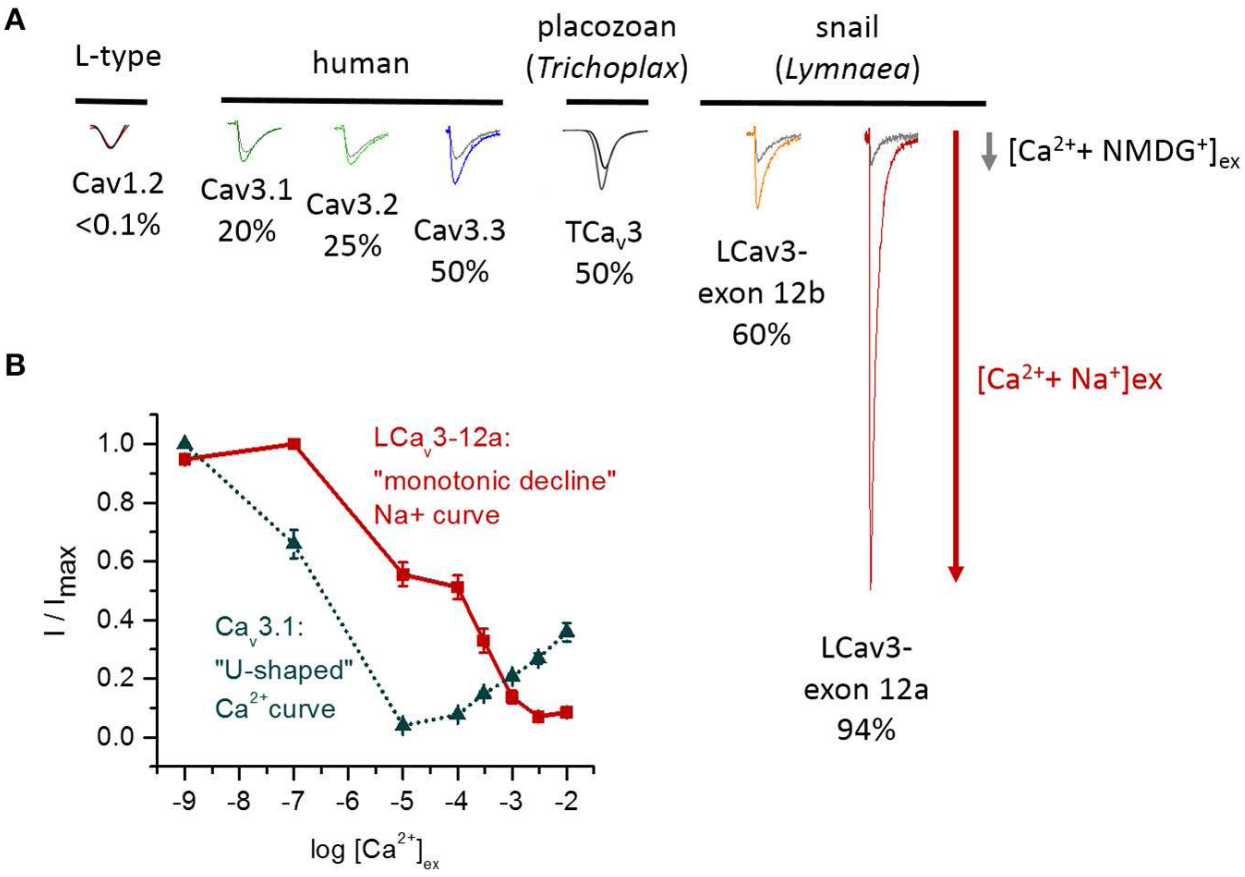

Figure 1.14 Calcium versus Sodium Currents Through T-type Calcium Channels from Humans, Trichoplax adherens, and Lymnaea stagnalis

(A) Results of $NMDG^+/Ca^{2+}$ versus Na^+/Ca^{2+} currents in Ca_v3 channel variants from humans, *T. adherens,* and *L. stagnalis*. $NMDG^+/Ca^{2+}$ represents the calcium current (grey) and Na^+/Ca^{2+} represents the current from both Ca^{2+} and Na^+ (coloured). LCa_v3-12a has the greatest sodium current, and $Ca_v1.2$ has the smallest sodium current. (B) Anomalous effect experiment results. $Ca_v3.1$ has a U-shaped curve, representing a $Ca2^+$ block of Na^+ current as $[Ca^{2+}]$ increases, followed by a Ca^{2+} current at $[Ca^{2+}] > 10^{-5}$ M. LCa_v3-12a, on the other hand, has a monotonic decline representing a weaker Ca^{2+} block of Na^+ currents. From (Stephens et al., 2015).

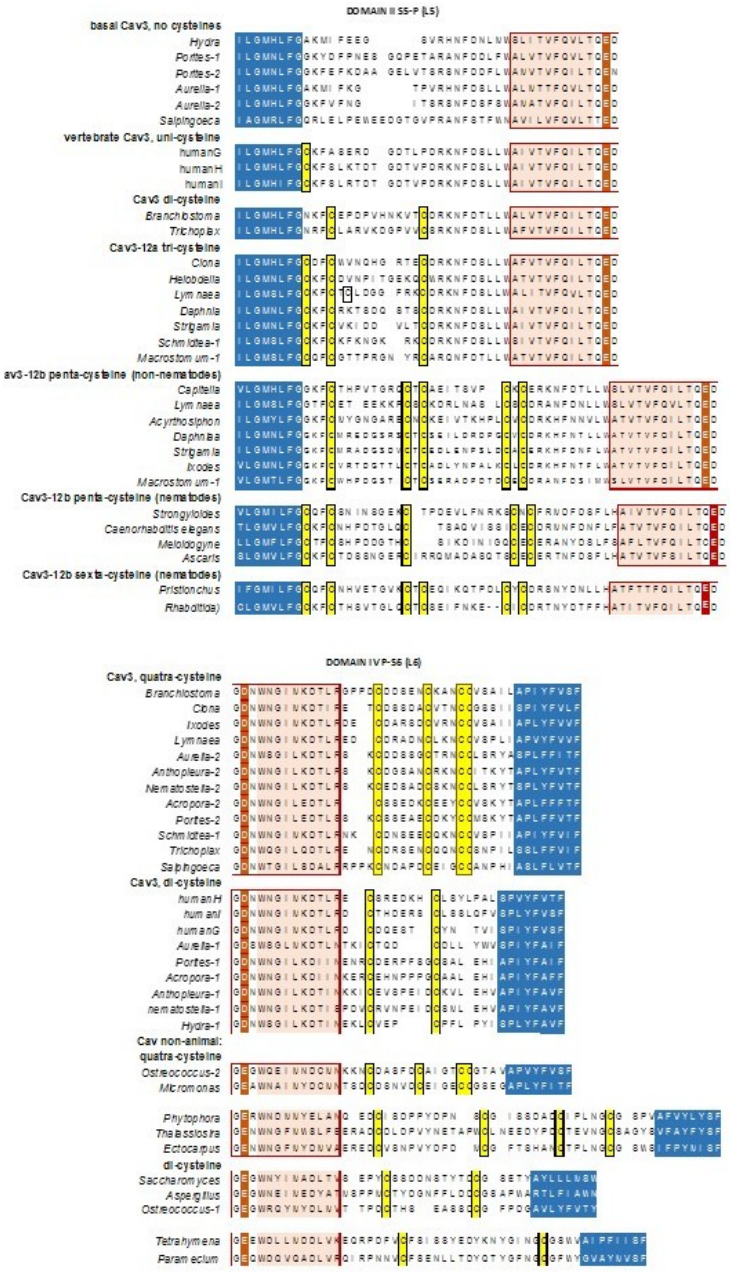

Figure 1.15 Sequences of Domain II and IV Turrets with Conserved Cysteine Contribution

Alignments of Domain II and Domain IV extracellular turret sequences display highly conserved cysteine residues with some organisms having two isoforms of either Domain II or Domain IV turrets. Domain II isoforms from *L. stagnalis* have differences in Ca^{2+} versus Na^{+} selectivity.

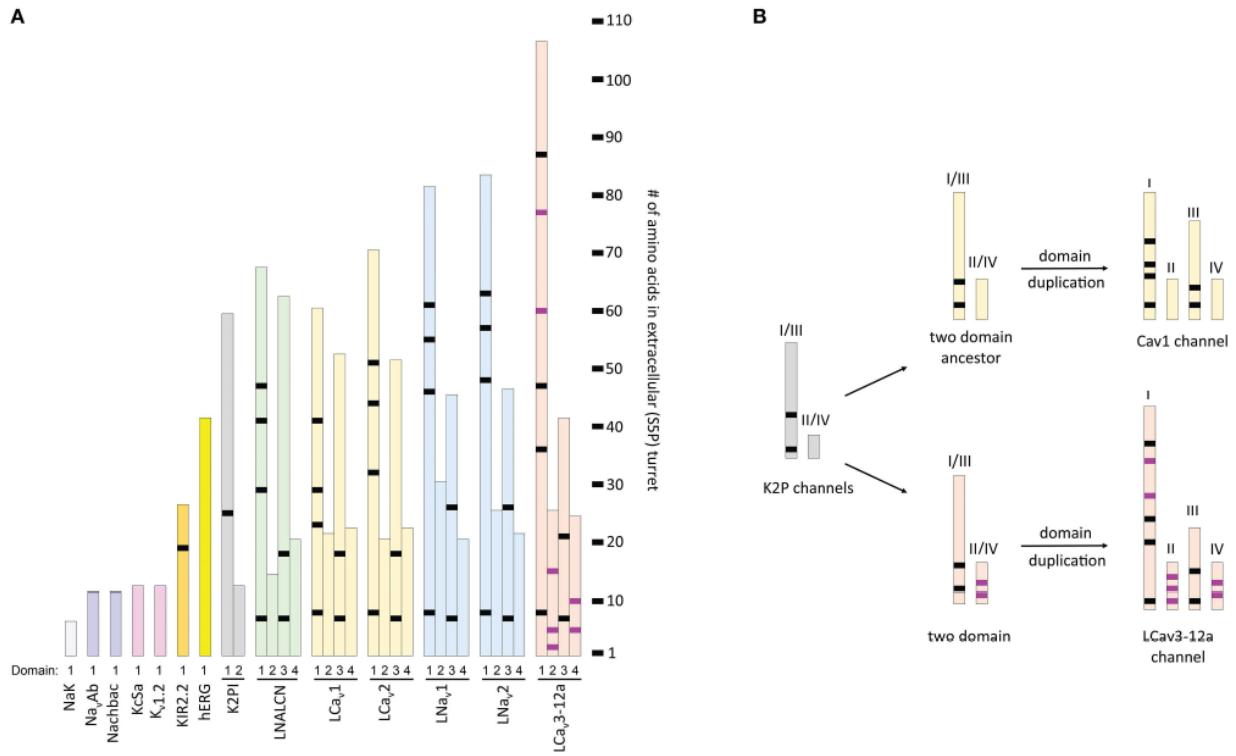

Figure 1.16 Relative Lengths of Extracellular Loops in K+ channels, two-pore K2P1 channel, and representative 4x6TM channels from the giant pond snail, Lymnaea stagnalis

Locations of shared cysteines are shown in black, while the T-type channel specific cysteines are shown in purple. (A) Short (6-12 residues) extracellular turrets in bacterial K and Na channels, and Shaker-type voltage-gated K channel (Kv1.2). Longer turrets (26 residues) in the human inward rectifying potassium channel, $K_{ir}2.2$, which changes the external landscape of the outer vestibule. Domain D1 turret in of the K2P1 channel is much longer (60 residues) than domain D2 turret (12 residues). The long D1-D1 turrets form a helical cap above the pore, bridged by a disulphide bond (Brohawn et al., 2012; Miller and Long, 2012). (B) Configuration of loops in DI-DII-DIII-DIV of 4x6TM channels resembles that in the K2P1 channel, after undergoing a domain duplication event. T-type channels differ from other 4x6TM channels by having a longer DI loops with additional cysteines and presence of T-type channel specific cysteines in the DII-S5P: DIV-S5P pair. From (Stephens et al., 2015)

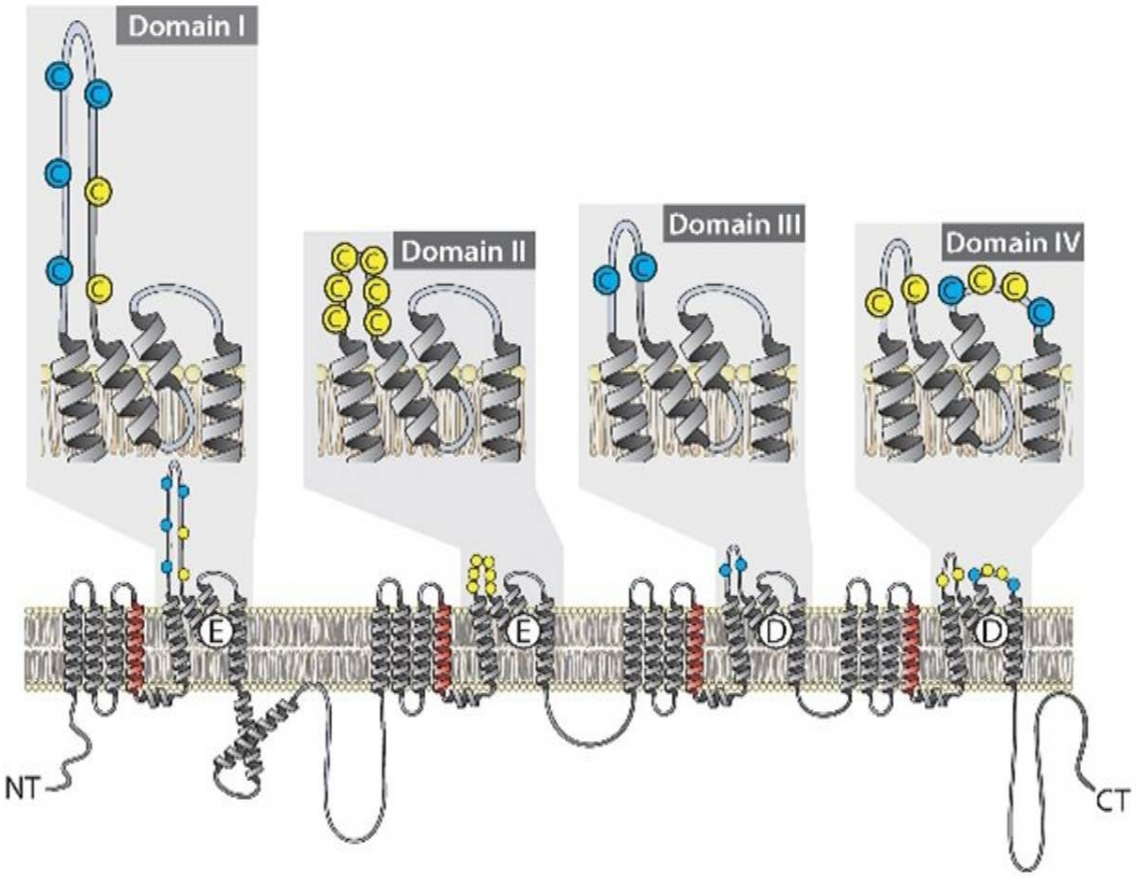

Figure 1.17 Conserved Cysteine Residues in Extracellular Loops of 4x6TM Channels

T-type channels have 8–14 additional cysteines (yellow) above the core eight cysteines (blue), which are conserved amongst all 4x6TM channels (Cav1, Cav2, Cav3, Nav1, Nav2, NALCN). From (Stephens et al., 2015).

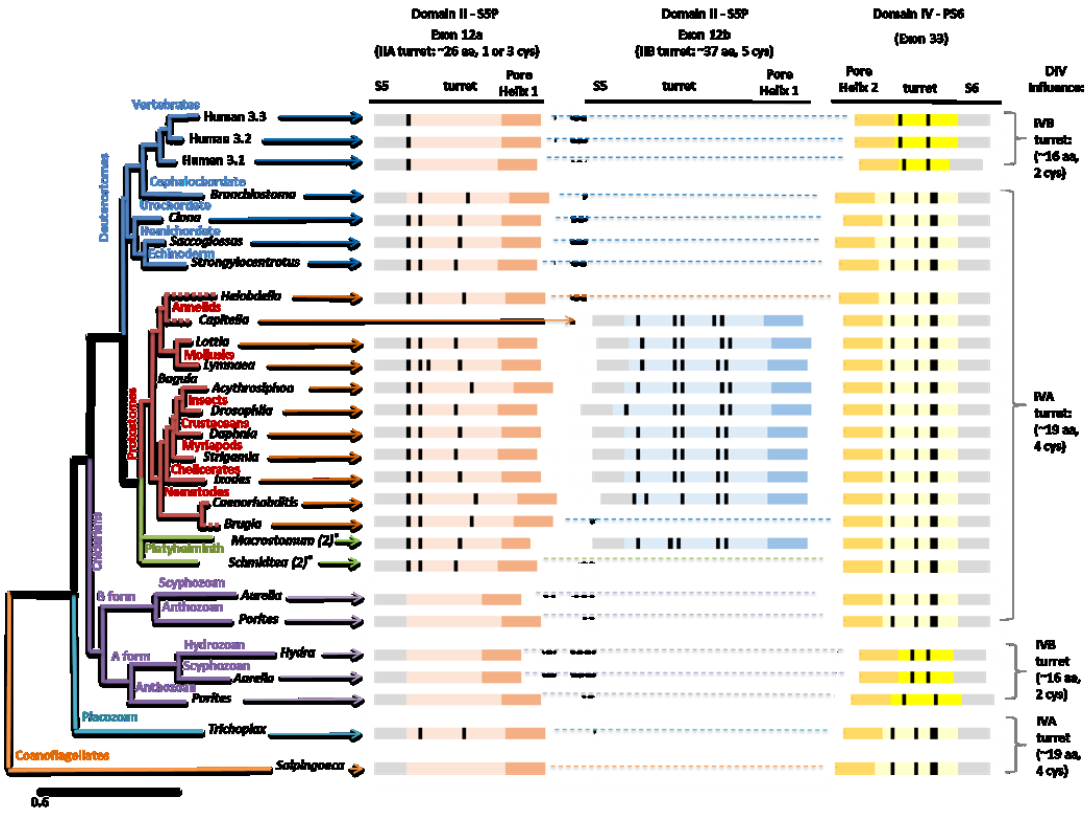

Figure 1.18 Highly Conserved Length and Cysteine Contributions of T-type Channels within Deuterostomes, Protostomes, and Cnidarians

A phylogenetic distribution illustrates the conservation of the relative lengths of the Domain II and Domain IV turrets, with cysteine residues indicated as black bars. Representative organisms of deuterostomes, protostomes and cnidarians are included. The placozoan *Trichoplax adherens* and Coanoflagellate *Salpingoeca rosetta* are also included. The Domain IV turret is indicated with varying shades of yellow and orange. The pore helix is orange. The version Domain IVA is indicated as a pale yellow, while Domain IVB is indicated as a bright yellow. The S6 helix is grey. Domain II versions are indicated with shades of pink and red (Domain II exon 12a) and shades of blue (Domain II exon 12b). The turret of exon 12a is a pale pink, while the pore helix is red. The turret of Domain II exon 12b is a pale blue, while the pore helix is a darker blue. The S5 helix of Domain II is grey.

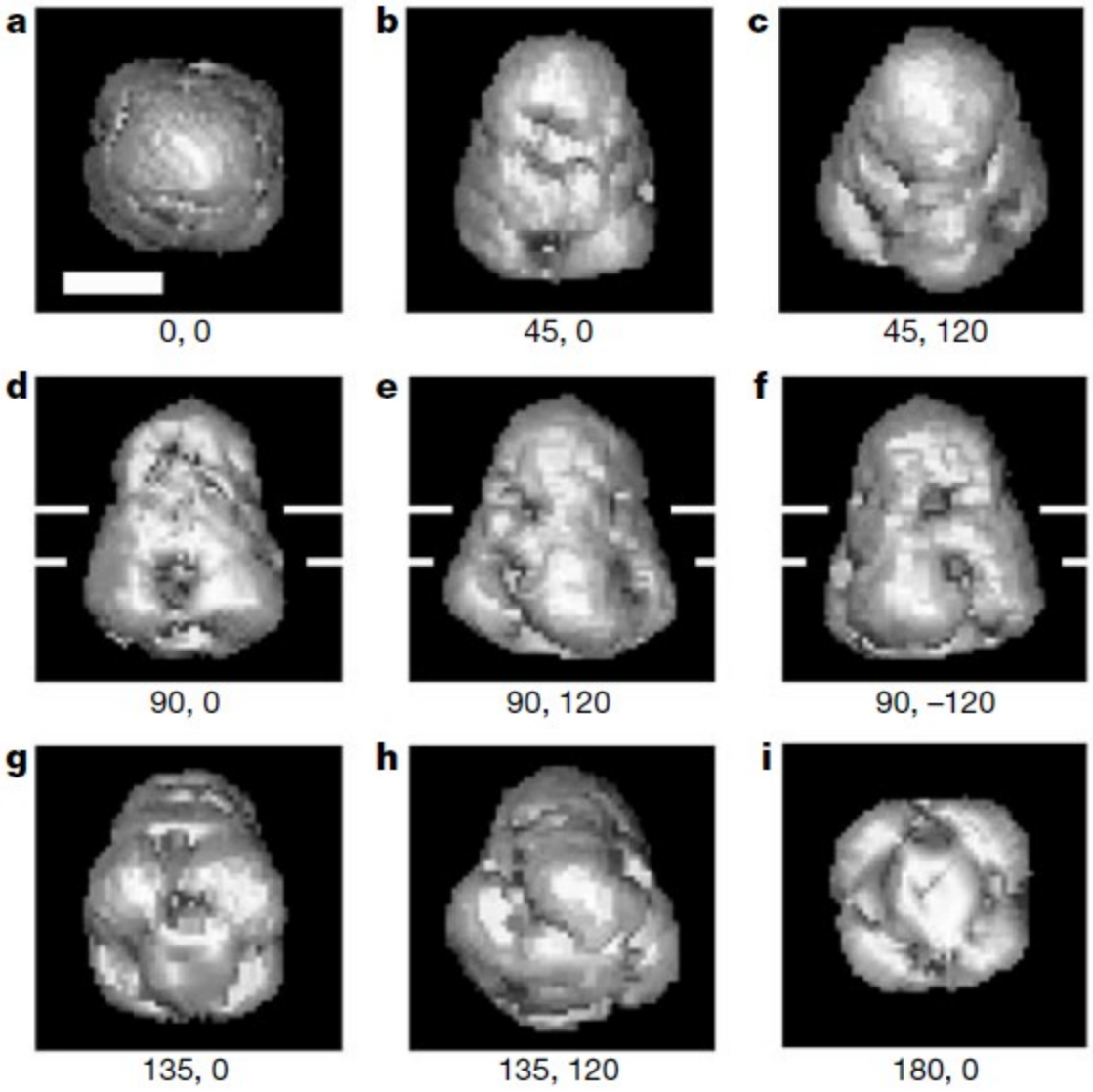

Figure 1.19 Surface Representation of Nav1 from *Electrophorus electricus*

(A) Top view. (B) View at oblique angle, related to A by +45^{o} rotation about the horizontal axis. (C) View at oblique angle, related to B by a +120^{o} rotation about the vertical axis. (D-F) Three side views rotated by 120^{o} intervals around the vertical axis. (G) View at oblique angle, related to D by a +45^{o} rotation about the horizontal axis. (H) View at oblique angle, related to G by +120^{o} rotation about the vertical axis. (I) Bottom view. An extracellular structure above the pore of the channel can be observed, corresponding to the location of the extracellular turrets. From (Sato et al., 2001).

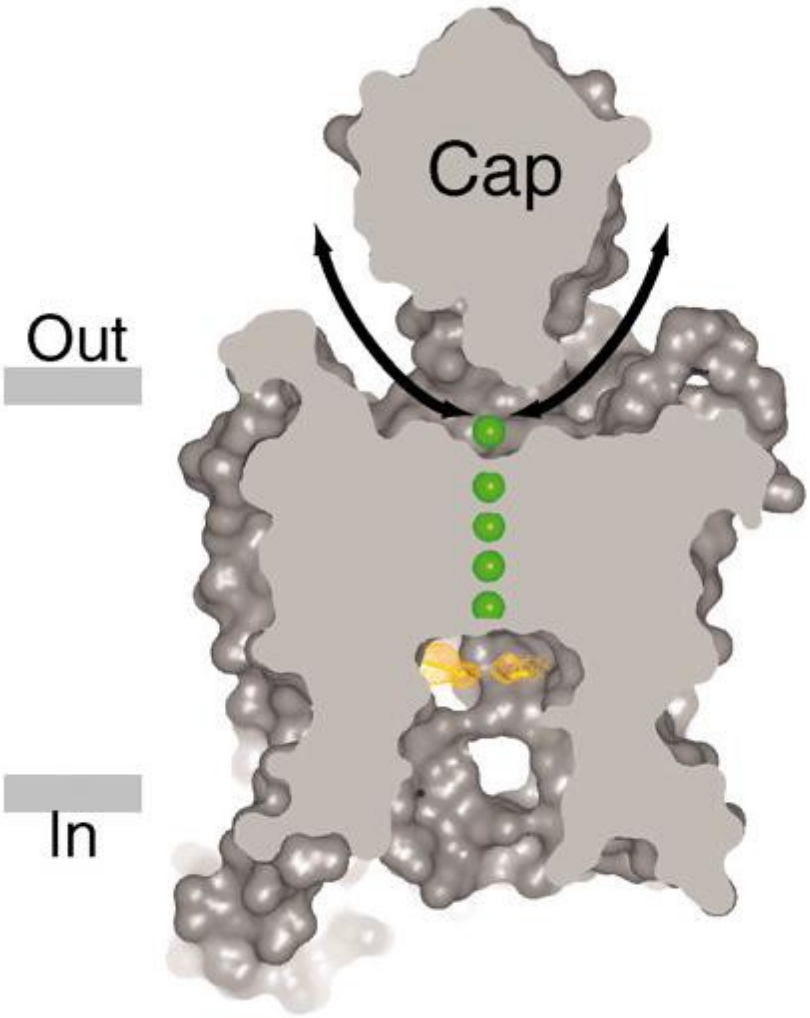

Figure 1.20 Side view K2P1 channel.

Turrets from the two-pore potassium channel form together to create an extracellular helical cap. Extracellular ions are pre-filtered by the helical cap, which lies just above the pore and ions access the selectivity pore from side portals. Approximate boundaries of the lipid membrane are shown as horizontal lines. K^+ ions (four sites in the selectivity filter and one external site) are shown as green spheres. Side portals (arrows) located beneath the extracellular cap connect the selectivity filter with the extracellular solution. From (Guan, 2014; Miller and Long, 2012)

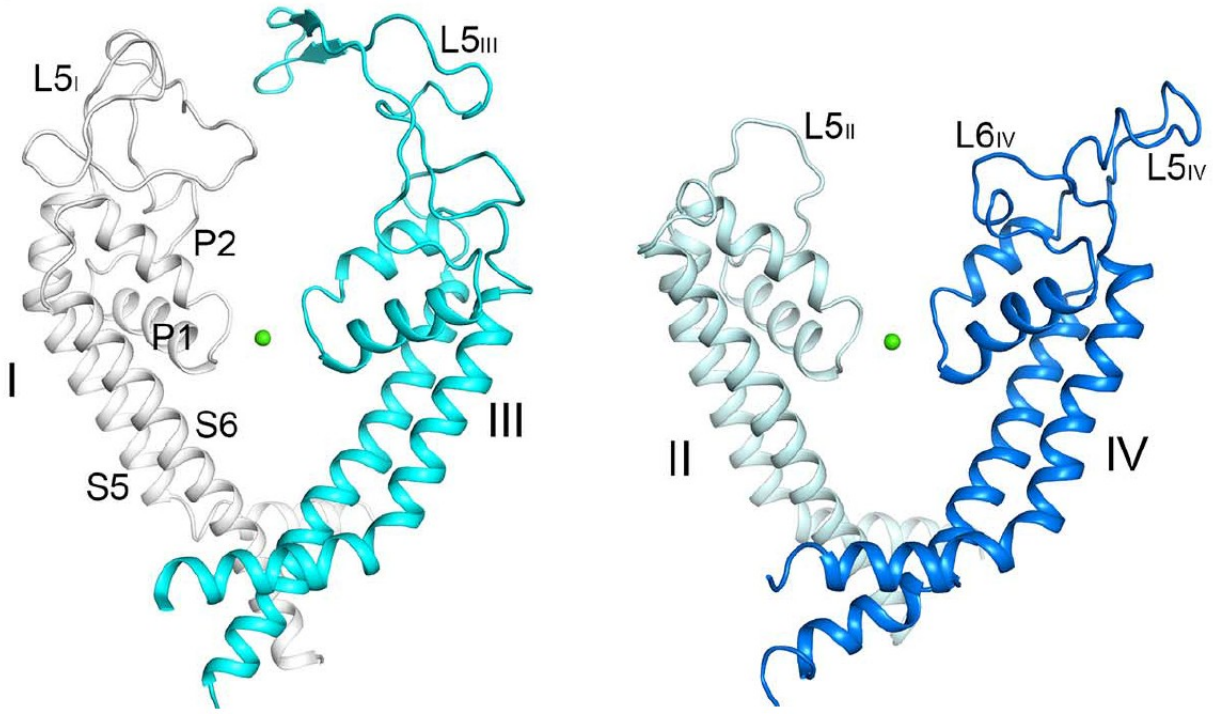

Figure 1.21 The Selectivity Filter and Extracellular Turrets of the $Ca_v1.1$ Channel

The structural elements that constitute the ion conduction channel of Cav1.1. Two diagonal repeats are shown in each panel. Similar to the bacterial homotetrameric Cav and Nav channels, the selectivity filter of Cav1.1 is supported by two pore helices (P1 and P2). A sphere-shaped density was found in the SF vestibule, which was tentatively assigned to a Ca2+ ion (green sphere). The extracellular loops (i.e., turrets) are indicated as $L5_I$, $L5_{II}$, $L5_{III}$, $L5_{IV}$ and $L6_{IV}$. The Domain II $L5_{II}$ turret and Domain IV $L6_{IV}$ turret are both facing the pore, and are positioned to influence ion selectivity. From (Wu et al., 2015)

(d) Highly Conserved Aspartate at Position 51 of Domain II in all Known Calcium Channels

In close proximity to the residues of the selectivity filter in T-type calcium channels there is an exceptionally well conserved tryptophan at p52, and an aspartate residue in DII at position p51 that is ubiquitous in all calcium channels (Senatore et al., 2012). It is predicted that the tryptophan residues at p52 participate in inter-repeat H-bonds with other amino acid residues in the pore to stabilize the outer pore structure. The aspartate residue in DII at p51 is well-position to serve as a "molecular beacon" to attract incoming calcium ions to the pore (See Figure 1.22). This aspartate residue is present in all known calcium channels. In engineering a calcium channel from a Na_vAb sodium channel, the substitution of a serine with an aspartate was necessary. The selectivity filter of Na_vAb from *Arcobacter butzleri* (^{175}TLESWSM^{181}) was mutated to ^{175}TLDDWSD^{181} to create Ca_vAb – a calcium selective bacterial sodium channel (Tang et al., 2014). The D^{178} residue, immediately adjacent to the D^{177} selectivity filter HFS residue, is analogous to the "molecular beacon" residue $D2_{p51}$ found in all eukaryotic calcium channels.

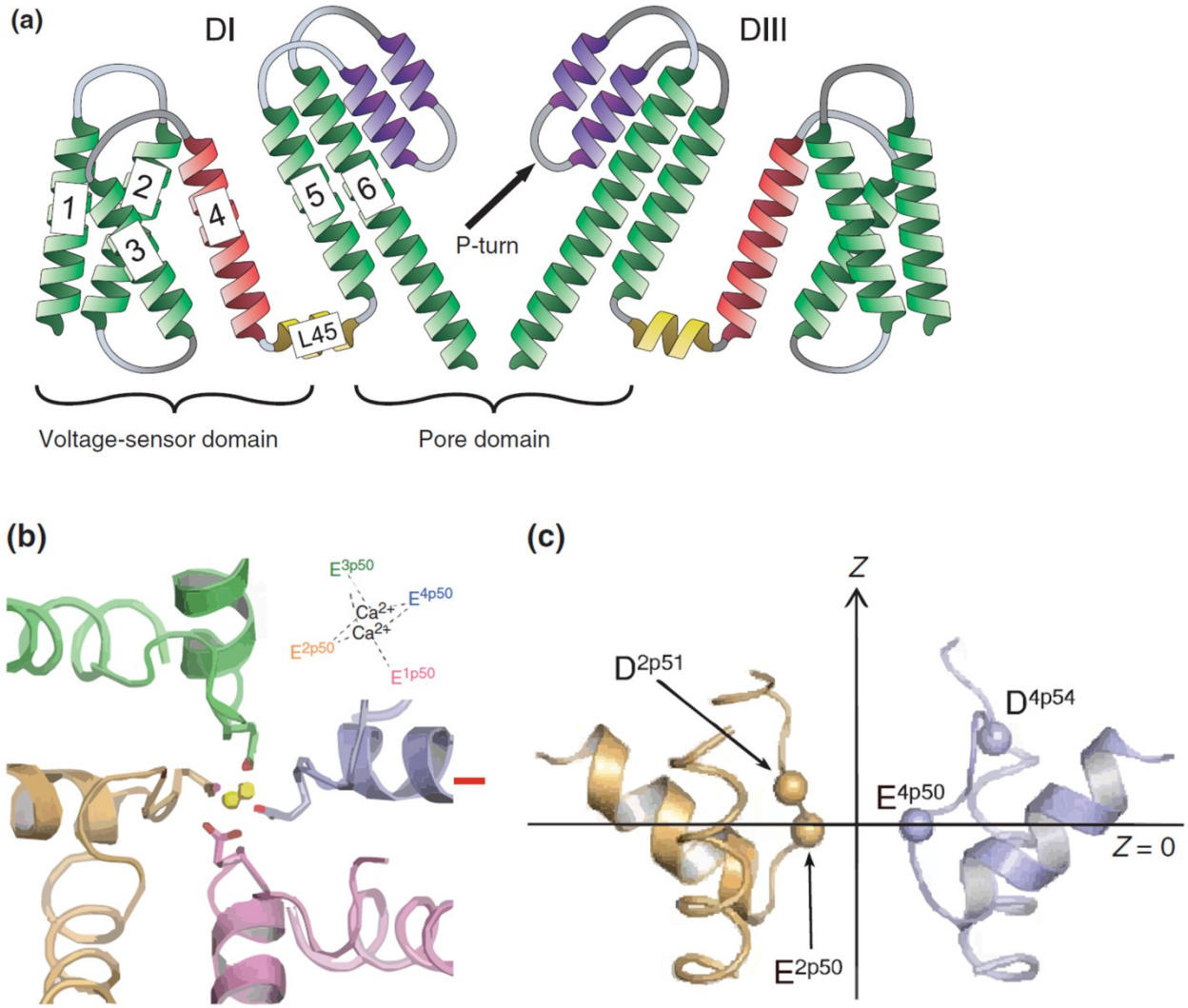

Figure 1.22 Critical Structural Features of the Pore Domain in Ca_v3 Channels

(A) Illustration of how P-loops between segments 5 and 6 project into the pore to form the selectivity filter. Shown only are domain I and II. (B) Illustration looking from the extracellular side into the pore of a voltage-gated L-type calcium channel, showing the predicted coordination of two calcium ions in the pore by the four glutamates present in the P-loops of each domain. (C) Illustration of the Domain II position 51 aspartate ($D2_{p51}$), projecting into the pore above the p50 selectivity filter glutamate. From (Senatore, Zhorov & Spafford, 2012).

vi A Possible Mechanism for the Involvement of Domain II and Domain IV in Sodium Permeation through T-type Calcium Channels

Dr. David Spafford and Dr. Boris Zhorov recently collaborated to determine a model (unpublished) that could reasonably be used to explain the influence that Domain II has on ion selectivity in LCa_v3 T-type calcium channels. Using the $Ca_v1.1$ cryo-EM structure (Wu et al., 2015) as a template and performing Monte Carlo simulations, structural models of the Domain II and Domain IV turret regions of $Ca_v1.1$ are provided (Figure 1.23 and 1.24).

Figure 1.23 provides a picture of the Domain II turret region of the $Ca_v1.1$ channel (halpha1S). The Domain II S5P turret ($L5_{II}$) in the human $Ca_v1.1$ structure loops towards the selectivity filter. The selectivity filter residues (EEDD) are indicated as red spheres. The closest residues of $L5_{II}$ that approach the selectivity filter are two arginine residues (R1 and R2). In Monte Carlo simulations, the positively charged R2 (also present in T-type channel) makes contact with the $D2_{p51}$ aspartate residue (i.e. "molecular beacon"). If the sequences of LCa_v3-12a and LCa_v3-12a are superimposed onto the model of $Ca_v1.1$ in Figure 1.23, differences in ion selectivity are explained; the configuration of LCa_v3-12a would allow for better neutralization of the $D2_{p51}$ residue by the R2 residue, thus minimizing calcium selectivity and allowing for sodium permeation.

A model of the Domain IV turret region of $Ca_v1.1$ is provided (Figure 1.24), with the locations of corresponding cysteine residues in LCa_v3 indicated (C1-C5 in Figure 1.24). The closest residue in the $L5_{IV}$ turret that approaches the selectivity filter (central red spheres) corresponds to a unique cysteine in T-type channels (labelled C2). Compared to $Ca_v1.1$, T-type channels have a longer $L5_{IV}$. Thus, the C2 residue might conceivably approach the selectivity

filter residues quite closely, affecting the positions of the selectivity filter residues. As reported by a few independent groups, the positions of the selectivity filter residues around the central pore axis are critically important in determining calcium versus sodium selectivity (Chakrabarti et al., 2013; Ellinor et al., 1995; Finol-Urdaneta et al., 2014; Hille and Schwarz, 1978; Hille, 1975; Talavera et al., 2001; Tang et al., 2014; Tsien et al., 1987; Yue et al., 2002). Previously, the cross-sectional asymmetry in eukaryotic Na_v channels has been noted and is likely contributing to Na^+ selectivity at the selectivity filter (Hille, 1971). Therefore, changes in the position(s) of selectivity filter residues caused by differences in the position of C2 of the $L5_{IV}$ turret might influence calcium/sodium ion selectivity.

Compared to $L5_{IV}$, the long $L6_{IV}$ region of the $Ca_v1.1$ structure is further away from the selectivity filter (Figure 1.24). The LCa_v3 cysteine residues (C3,C4, and C5) within the $L6_{IV}$ region might be influencing the C1 and C2 residues of $L5_{IV}$, altering the approach of the $L5_{IV}$ region towards the pore selectivity filter. Another way that the $L6_{IV}$ region might be influencing ion selectivity is by allosterically affecting the orientation of the $L5_{IV}$-P-$L6_{IV}$ region as a whole, changing the position of the $L5_{IV}$ C2 residues and selectivity filter residues.

Based on the models provided by Dr. Spafford and Dr. Zhorov, it is possible that the Domain IV turret region is influencing ion selectivity in T-type calcium channels. Based on these models, the $D2_{p51}$ residue and the position of the arginine residue, R2, in $L5_{II}$ are important factors in determining the ion selectivity of T-types. In Domain IV, the overall structure and orientation of the $L5_{IV}$-P-$L6_{IV}$ is probably important in determining ion selectivity in T-type calcium channels. The position of C2 in $L5_{IV}$ seems to be critical, because it is in a position to interact with the selectivity filter residues. Interestingly, the LCa_v3 channel has an additional cysteine residue (C4) in $L5_{IV}$, which is not present in the human Ca_v3 channels.

Before the orientations of the Domain II and Domain IV turrets proposed in Figures 1.23 and 1.24 can be accepted, it is necessary to experimentally confirm that the Domain IV turret and $D2_{P51}$ residue do, in fact, influence ion selectivity in T-type channels.

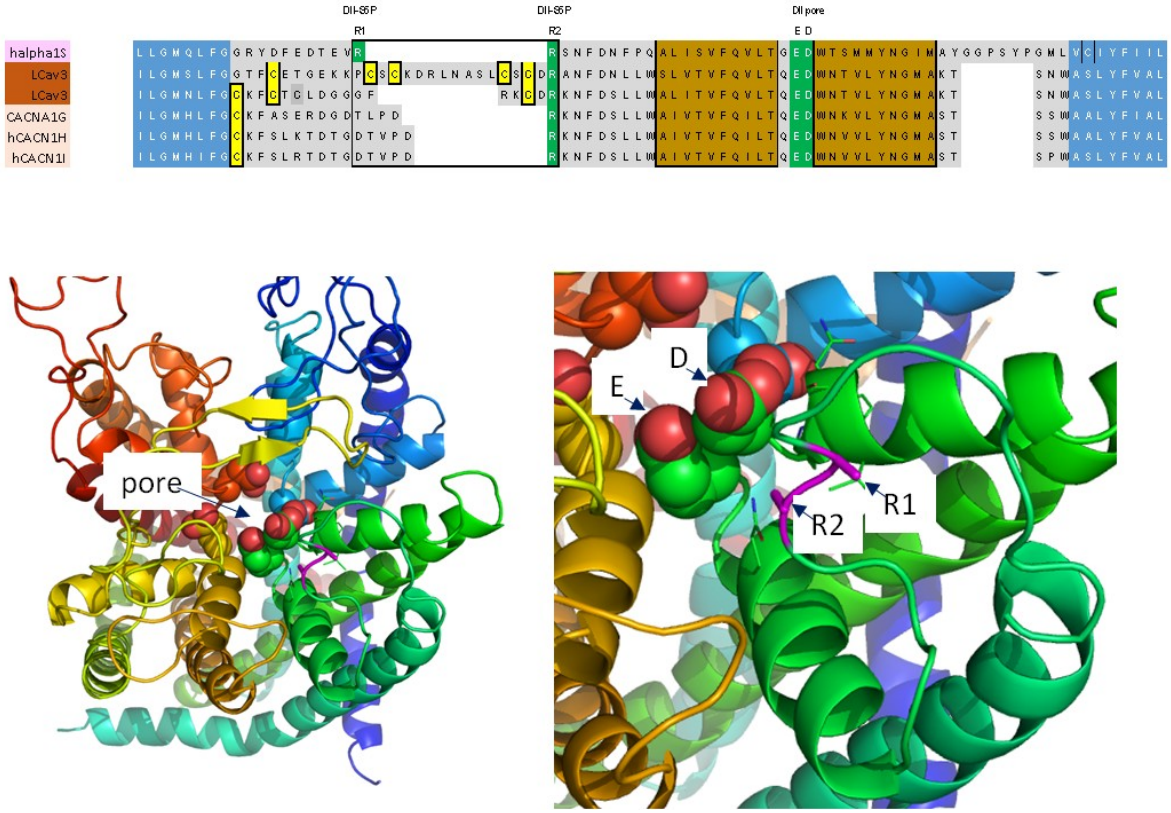

Figure 1.23 Model of Domain II Turret Involvement in Ion Selectivity Based upon the Structure of $Ca_v1.1$

The Domain II S5P turret in the modeled human Cav1.1 structure (see Figure 1.20) loops towards the selectivity filter. The closest residue in the DII turret that approaches the selectivity filter is near two arginine residues (R1 and R2). The positively-charged side chain of R2 contacts the "molecular beacon" aspartate (D) near the Domain II selectivity filter, which regulates calcium selectivity (See Figure 1.21; Cheng et al., 2010). If snail LCav3-12a and LCav3-12b sequences are superimposed on the structure, LCav3-12a would place R2 in a position to neutralize the molecular beacon aspartate residue better than the LCav3-12b turret, and would thus make the LCav3-12a channel more sodium selective. Monte Carlo simulations of the lowest energy conformation were used to determine probable side change movements.

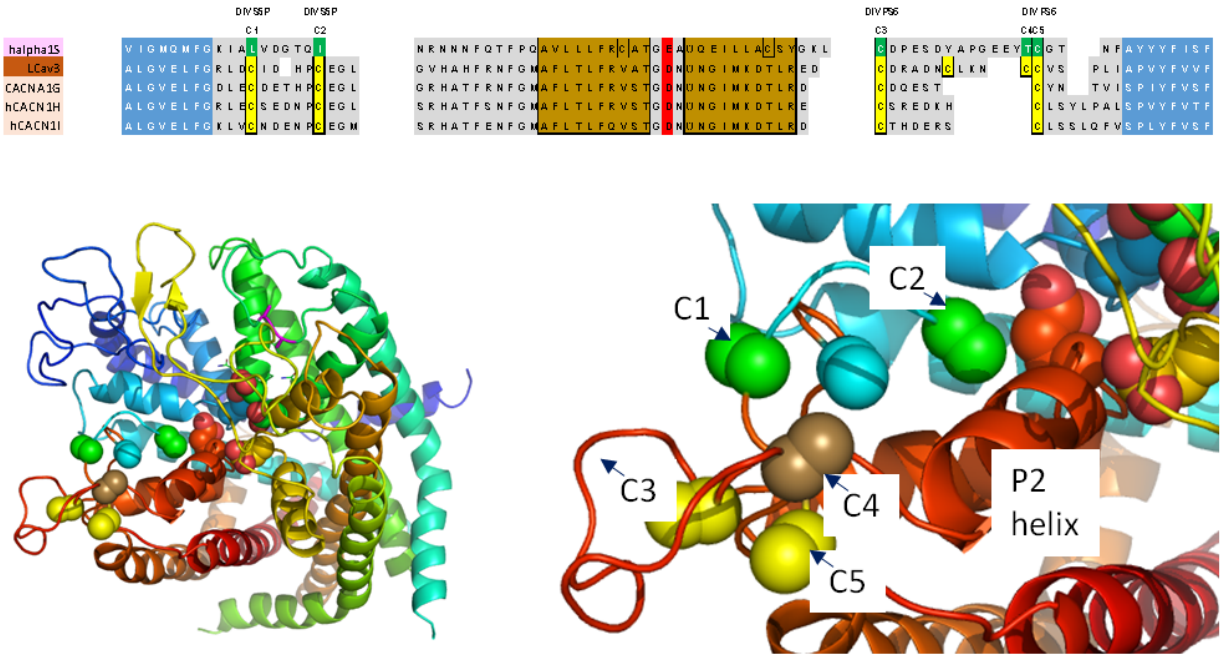

Figure 1.24 Model of Domain II Turret Involvement in Ion Selectivity Based upon the Structure of $Ca_v1.1$

The Domain IV S5P turret in the modeled human Cav1.1 structure loops towards the selectivity filter. The closest residue in the DIV S5P turret that approaches the selectivity filter is near a cysteine residue that is unique to T-type channels, C2. T-type channels have a longer S5P turret than L-type channels, and thus may closely approach the selectivity filter residues opposite DII S5P turret, affecting calcium/sodium ion selectivity. The region surrounding C3, C4 and C5 cysteines in Domain IV PS6 is far away from the selectivity filter. The region between C3-C5 cysteines (in PS6) interacts with the region near the C1 and C2 cysteines (S5P), altering the approach of DIV S5P turret towards the pore selectivity filter. Alternatively, PS6 (C3-C5 cysteine region) allosterically affects the orientation of C1-C2 in the S5P region, affecting its approach to the selectivity filter. Monte Carlo simulations of the lowest energy conformation were used to determine probable side change movements.

2. Objectives & Hypothesis

The objectives of this MSc research project involve exploring structures of T-type calcium channels and determining their role(s) in ion selectivity.

The focus of my research is the structure of the extracellular turret. The turret of Domain II is within a region of the alternatively spliced exon 12, which generates the highly sodium permeable LCa_v3-12a and the calcium-selective LCa_v3-12b (Senatore et al., 2014). Given the highly conserved cysteine arrangement of both Domain II and Domain IV turrets (Figure 1.18), the presence of alternative splicing in the Domain IV turrets of certain groups of cnidarians (both anthozoans and scyphozoans; Figures 1.15 and 1.18), the evolutionary relatedness of Domain II and Domain IV (Figure 1.3), and a feasible model for the involvement of Domain II and Domain IV in ion selectivity (Figure 1.23 & 1.24), we hypothesize that the turrets are interacting with residues of the high-field strength site (HFS, i.e., selectivity filter) to influence ion selectivity in T-type calcium channels. The research will be executed by 1) creating chimeric LCa_v3 channels in which Domain IV turrets from LCa_v3 have been replaced with Domain IV turrets from the human channel $Ca_v3.2$, and 2) using whole-cell patch clamp electrophysiology of transfected T-type channels and derivative chimeras in mammalian HEK293T cell lines to explore the influences that the turret regions have on ion selectivity. Based on the results of the previous studies and preliminary data obtained by Wendy Guan in Dr. David Spafford's Lab at the University of Waterloo, the following hypotheses are proposed:

1) The LCa_v3 chimeras with Domain IV replaced by the Domain IV turret from $Ca_v3.2$ will become more $Ca_v3.2$-like in terms of Ca^{2+} versus Na^{+} selectivity (i.e. the chimeras will have higher calcium permeability).

2) The LCa$_v$3 channel chimeras with Domain IV L6 from Ca$_v$3.2 will influence ion selectivity regardless of the character of the Domain II turret.
3) These turrets are interacting with the "molecular beacon" at D2$_{p51}$ (Cheng et al., 2010) to influence ion selectivity, so a mutant in which the aspartate at position 51 in Domain II is substituted for an asparagine residue (i.e. Ca$_v$3.2 DII$_{D975N}$) will become non-selective or less-selective for calcium ions.
4) There will be small changes in gating kinetics in the chimeras (compared to the wild-types). The changes are expected to be minimal because the turrets are not in a position to significantly affect the movement of the helices of the voltage sensor domain (VSD). However, Wendy Guan found that the ΔCys mutants and LCa$_v$3-DII$_{\alpha 1hL}$ influenced channel kinetics, suggesting the turrets might have a minimal influence on gating in some way that is not yet understood.

Chimeric and mutagenized channels from snails will compared to their original counterpart channels and the expression of the three human Ca$_v$3 homologs. They will also be compared to the cysteine-substitution (ΔCys) mutants explored in Wendy Guan's Master's thesis (Guan, 2014). The overall goal of this research is aimed at creating a comprehensive structural model that could explain how variations in the extracellular turrets of T-type channels could affect the pore to alter ion permeability and selectivity. If the hypotheses are supported by the results of this research, support will be provided for the mechanisms proposed by the structural models proposed in Figures 1.23 and 1.24.

3. Materials and Methods

I General Cloning Methods

The full length snail LCa_v3 calcium channels presented in this thesis (LCa_v3-12a and LCa_v3-12b) contain extracellular turrets with "a" and "b" splice isoforms of exons 12 were cloned by Dr. Adriano Senatore (Senatore and Spafford, 2010). The LCav3 calcium channel chimera containing a Domain II extracellular turret from $Ca_v3.2$ (α1H) is dubbed as LCa_v3- $DII_{\alpha 1hL}$. It was constructed and cloned during my undergraduate Senior Honours Project and summer studentship (NSERC USRA) in the Spafford laboratory. During this time, I also completed cysteine substitutions with alanine residues in the LCa_v3 Domain II turrets coding for exon 12a and exon 12b isoforms, herein referred to as LCa_v3- 12a ΔCys and LCa_v3- 12b ΔCys. The calcium channel chimera, LCa_v3- 12b $DIV_{\alpha 1hL}$ which contains the Domain IV turret of $Ca_v3.2$ (α1H) within LCa_v3 calcium channel was constructed and cloned by Omar Mourad, a fourth year undergraduate project student in the Spafford lab. Human $Ca_v3.1$, $Ca_v3.2$ and $Ca_v3.3$ calcium channels were a gift to the Spafford laboratory from Edward Perez-Reyes (University of Virginia).

i Preparing Electrocompetent *Escherichia Coli* Cells (CopyCutter™ and ElectroMAX™ Stbl4)

In order to transform *Escherichia coli* cells with cloning vectors containing calcium channel cDNA inserts, pure populations of electrocompetent *E. coli* cells were required. To

obtain these cells, a modified Hanahan competent cell preparation method was used (Hanahan, 1983). The entirety of the procedure was carried out using proper aseptic technique.

First, non-selective Luria-Bertani (LB) agar plates and flasks containing 250 mL of non-selective super broth (SB) were prepared. The LB agar plates were inoculated with Electrocompetent CopyCutter^{TM} cells (Epicenter Biotechnologies, #C400EL10) or ElectroMAX^{TM} Stbl4 Electrocompent cells (Invitrogen, #11635-018) using a streak-plate method, and then the plates were inverted and incubated at 37^{o}C for 24-36 hours. Following the incubation period, the plates were inspected and the smallest colony was extracted; this colony was used to inoculate 10 mL of SB in a test tube. The inoculated SB culture was placed in a shaking incubator (300 rpm) at 37^{o}C and left overnight (~12 hours). The next day, 5 mL of the SB *E. coli* culture was added to 250 mL of SB. This 250 mL SB culture was incubated at 37^{o}C, shaking at 300 rpm. A Nanodrop® ND-1000 (Thermo Scientific NanoDrop Products, Wilmington, Delaware USA) was used to measure the optical density of the culture at 600 nm (OD_{600}), until an OD_{600} of 0.3-0.6 was obtained which corresponded with early to mid log phase of bacterial growth. Once the desired OD_{600} was reached, the *E. coli* cell culture was chilled on ice for 20 minutes and then transferred to an ice-cold centrifuge bottle. The culture was centrifuged at 4000 g for 15 minutes at 4^{o}C in a refrigerated Beckman Coulter Allegra 25R centrifuge (Beckman Coulter Canada LP, Mississauga, Ontario, Canada). Following centrifugation, the supernatant SB was carefully poured off and discarded in a bleach solution for disinfection. The remaining pellet of *E. coli* cells was gently washed with ice-cold, sterile 10% v/v glycerol (Fischer Scientific, #56-81-5). The pellet of cells was resuspended in 250 mL of ice-cold, sterile 10% v/v glycerol, and then subjected to centrifugation at 4000 g for 15 minutes at 4^{o}C. The supernatant glycerol solution was discarded in bleach. The wash step was repeated

again. Following the second wash, the pellet of *E. coli* cells was resuspended in 20 mL of ice-cold, sterile 10% v/v glycerol and transferred to a 50 mL Falcon tube. The Falcon tube containing suspended cells was centrifuged for 15 minutes at 4000 g and 4°C. This pellet was resuspended in 1-2 mL of ice-cold, sterile 10% glycerol to a concentration of ~1-3 x 10^9 cells/mL (a 1:10 dilution of the suspension had an OD_{600} of approximately 0.01-0.03, as measured by the ND-1000). The suspension of electrocompetent cells was quickly aliquoted into 0.2 mL PCR tubes at 50 uL per tube, and then rapidly frozen in liquid nitrogen and stored at -80°C until use.

ii Bacterial Transformations

Two different *Escherichia coli* strains were used for bacterial transformations: Electrocompetent CopyCutter™ cells were used for transformations of LCa_v3 channel cDNAs and the chimeras derived from these channels, and ElectoMAX™ Stbl4 electrocompetent cells were used for all other channel cDNAs. These cells were prepared and stored at -80°C until use (see section 3.I.i). Generally, two transformations were done at a time – one of these transformations was a control transformation. The transformation procedure is described below.

A 0.2 mL PCR tube containing 40 µL of frozen *E. coli* cells was removed from storage at -80°C and allowed to thaw on ice. 1-2 µL of plasmid cDNA was mixed with 20 µL of the thawed *E. coli* cell suspension. The mixture was kept within a pre-chilled 1.5 mL microfuge tube. This mixture was incubated on ice for 5-10 minutes. Following this brief incubation period, the mixture was transferred to a pre-chilled 90 µL electroporation cuvette (VWR, #89047-206 stored at -20°C). The cuvette was then placed in an Eppendorf Electroporator 2510 (Eppendorf Canada,

Mississauga, Ontario, Canada) and 1200 mV was applied to the *E. coli*-plasmid mixture, allowing for electroporation of the *E. coli*. 1 mL of pre-heated (37^{o}C) super broth media (SB) without antibiotics was added to the cuvette and mixed with the transformed *E. coli* cells. This mixture was transferred to a 1.5 mL microcentrifuge tube and incubated at 37^{o}C for 1 hour, shaking at 600 rpm. After the 1 hour incubation period, the mixture was centrifuged at 4000 g for 2.5 minutes. 900 µL of the supernatant was removed, and the pellet was resuspended in the remaining SB supernatant. This culture was transferred to an LB agar plate, selective with either kanamycin antibiotic (OmniPur, #5880) at 50 µg/mL or ampicillin antibiotic (BioShop, #AMP201) at 100 µg/mL , depending on the plasmid. Bacteria were spread on the plate with a spreader, and the plates were inverted and placed into a 37°C incubator for 30-36 hours for bacterial colonies to form.

iii Plasmid Isolation and Purification

Larger preparations of plasmids were isolated from *Escherichia coli* cloning vectors and purified using a mini-prep protocol. This protocol consisted of alkaline lysis followed by purification, which involved the removal of unwanted RNA molecules and proteins (Birnboim and Doly, 1979). Often, many bacterial colonies were grown and prepared, in parallel, to amplify larger quantities of the plasmid DNA construct(s) of interest; the procedure for bacterial growth and plasmid amplification and purification from a single colony is outlined here.

E. coli cells were transformed with the desired plasmid DNA, as described in section 3.I.ii. A single, pin-sized colony was selected from an antibiotic-selective agar plate. Based on assumptions of metabolic load, the smallest colony was chosen to increase the probability that

plasmid DNA was being synthesized by the host cells (Glick, 1995). A test tube with 10 mL of a selective super broth media containing 50 μg/mL of kanamycin or 100 μg/mL of ampicillin (depending on the selective marker present on the desired plasmid) was inoculated with the chosen colony. The culture was allowed to grow for 12-36 hours in a 37^{o}C incubator, shaking at 350 rpm. For LCa_v3 channel constructs, which tend to undergo recombination in *E. coli* host cells, only those cultures that reached optimal density between 30-36 hours were used in a mini-prep. The plasmid products may have been toxic to the *E. Coli* host, so the slowest growing cells were the most likely to be synthesizing the plasmid DNA constructs of interest (Senatore, 2012).

When the cultures reached an optimal density, the test tube was removed from the incubator. Using a 7.5 mL transfer pipet, ~2 mL of the culture was transferred to a 2.0 mL microcentrifuge tube and centrifuged at 4000 g for 2 minutes at 4^{o}C (Eppendorf Centrifuge 5415 R). The supernatant was discarded in bleach for disinfection. This process was repeated 5 times, at which time all of the culture media had been centrifuged. The pellet of *E. coli* cells was placed on ice, and then resuspended in chilled 270 μL of solution I (50 mM glucose, 25 mM Tris-HCl, pH 8.0 and 10 mM EDTA, pH 8.0, stored at ~4^{o}C). After the cells were resuspended, 540 μL of solution II was added to the microcentrifuge tube (1% v/v sodium dodecyl sulfate and 0.2M NaOH). Solution II lyses *E. coli* cells and leads to the denaturation of proteins and nucleic acids. The contents were mixed by gently tapping the tube. After the cells were thoroughly mixed with solution I and solution II, a third solution (solution III: 3M potassium acetate and 11.45% v/v of glacial acetic acid, stored at -20^{o}C) was added to the mixture. The contents of the tube were briefly but vigorously mixed by inversion, tapping, and vortexing. Mixing produced a flocculent white precipitate. The microcentrifuge tube was quickly placed in the 4^{o}C centrifuge and subjected to ~9000 g for 3 minutes. The supernatant was transferred to a new 2.0 mL

microcentrifuge tube and the pellet of cellular debris was discarded. 600 µL of 2-propanol was added to the tube containing the supernatant. The contents of the tube were mixed by vortexing and then incubated at -20^{o}C overnight.

The next day, a white precipitate was visible in the solution within the 2.0 mL microcentrifuge tube. The tube was centrifuged at >16000 g for 20 minutes at 4^{o}C. A white pellet was clearly visible at the bottom of the microcentrifuge tube. The supernatant was discarded and the tube was inverted for ~5 minutes to allow the pellet to dry. Then, the pellet was resuspended in 400 µL of autoclaved MilliQ water (resistivity ~18.2 MΩ x cm). The contents of the tube were vortexed to allow for optimal mixing. 400 µL of ice-cold 5M LiCl (stored at -20^{o}C) was added and the solution was vortexed for mixing, and then incubated on ice for 30-60 minutes to allow for precipitation of RNA molecules. Following the incubation period (a precipitate may or may not be visible), the microcentrifuge tube was centrifuged at >16000 g for 20 minutes at 4^{o}C. The supernatant was transferred to a 1.5 mL microcentrifuge tube and the RNA pellet was discarded. 600 µL of 2-propanol was added to the new 1.5 mL microcentrifuge tube with supernatant. The mixture was incubated at -20^{o}C overnight to allow for precipitation.

The next day, the tube was centrifuged in a 4^{o}C centrifuge for 20 minutes at >16000 g. After centrifugation, a white pellet was clearly visible. The supernatant was discarded and the tube was inverted to dry the pellet. Then, the pellet was resuspended in 400 µL autoclaved MilliQ water. In some cases, 2 µL of this solution was removed and used in a diagnostic restriction enzyme digest (see section 3.I.iv). 2 µL of a 20 mg/mL RNAseA (BioShop, #RNA675) solution was added. The final concentration of RNAseA was ~100 µg/mL in solution. This solution was incubated at 37^{o}C to allow for the RNAseA enzyme to digest the RNA molecules within the solution. If the purified DNA (i.e., the final product of the mini-prep) was

to be used in downstream mammalian cell transfection reactions, the tube was transferred to 4°C and incubated overnight.

After the incubation period, phenol/chloroform extraction was used to separate the desired DNA product from any proteins present in the mixture (including the RNAseA protein previously added). 400 µL of 50:50 phenol/chloroform was added to the microcentrifuge tube. The tube was vortexed for 12 seconds and then centrifuged for 3 minutes at >20000 g at room temperature. This resulted in phase separation, with the denser phenol/chloroform layer on the bottom and the aqueous DNA solution in the top phase. The aqueous layer was transferred to a new 1.5 mL microcentrifuge tube. The tube containing the phenol/chloroform layer was properly discarded. The 50:50 phenol/chloroform extraction procedure was repeated. Then, in an attempt to remove any residual phenol in the aqueous DNA solution, the process was repeated with pure chloroform in place of 50:50 phenol/chloroform. After following the above steps, 400 µL of and aqueous DNA solution was within a new 1.5 mL microcentrifuge tube. To precipitate the plasmid DNA product present, 21 µL of 10M ammonium acetate and >99% ethanol was added to the microcentrifuge tube. The mixture was vortexed and then incubated at -20°C overnight.

The next day, a white precipitate was visible. The microcentrifuge tube was centrifuged at >16000 g for 20 minutes in a 4°C microcentrifuge. A white pellet was clearly visible on the bottom of the tube. The supernatant was discarded and 200 µl of ice-cold 70% ethanol was added to the microcentrifuge tube to wash the pellet, removing excess salts and debris. Then the tube was centrifuged for 5 minutes at 4°C and >16000 g. The supernatant was discarded. The 70% ethanol wash was repeated. Then, the microcentrifuge tube containing the pellet of purified plasmid DNA was inverted for 5 minutes on a paper towel and then incubated at room temperature for 5 minutes to remove any ethanol. The dry pellet was resuspended in 30 µL of

autoclaved MilliQ water and the concentration and purity of DNA was measured using the Nanodrop ND-1000. Absorbance at 280 nm (A_{280}) was used to assess DNA concentration and $A_{260/280}$ was used to assess DNA purity. $A_{260/280}$ of 1.8-1.9 was deemed acceptable and considered to be pure DNA (Wilfinger et al., 1997). If $A_{260/280}$ was >1.9, the RNAseA digest and all downstream purification steps were repeated. The final, purified plasmid DNA solution was stored at -20^{o}C until use.

iv Restriction Enzyme Digests to Confirm Proper Sequences of cDNA Starting Materials

Diagnostic restriction enzyme digests were used to confirm the identities of the cloned plasmids. The restriction enzymes were ordered from New England Biolabs (NEB). Generally, 1 unit of restriction enzyme can be used to digest 1 μg of plasmid DNA. Typically, more restriction enzyme was used to ensure complete digestion of the DNA, as long as the amount of restriction enzyme did not exceed 1/10 the volume of the solution. All reactions were carried out in 0.2 mL PCR tubes incubated at 37^{o}C. A total volume of 10 μL was used. 1 μL of a 10X buffer and 1 μL of 10X bovine serum albumin (BSA) were always included. Where possible, an uncut plasmid was run in parallel as a control. Also, where possible, a positive control was digested in parallel. For the plasmids constructed as part of this research project, there was also often a precursor plasmid available to be used as a negative control.

The wild-type LCa_v3 variant used in this project was configured with optional exon 8, but lacking optional exon 25c +8b/-25c/12a (LCa_v3-12a) and +8b/-25c/12b (LCa_v3- 12b). All full length LCa_v3-12a and LCa_v3-12b plasmids were digested in 1μL of 10X NEB buffer

3.1(#B7203), 1µL of 10X bovine serum albumin (BSA) (#B9000), 0.3µL BglII (#R0144), 0.3µL MluI (#R0198), 0.3µL SalI-HF (#R3138) and 1µL of plasmid. A total volume of 10 µL was used for this reaction; the remaining volume was filled by water. The expected bands consisted of ~2500 bp, 2300 bp and 8500 bp for LCa_v3-12a and LCa_v3-12b in pIRES2 vector backbones.

The wild-type human $Ca_v3.2$ channel DNA was digested in 1µL of 10X NEB Cutsmart® buffer (#B7204), 1µL of 10X bovine serum albumin (BSA) (#B9000), 1µL ScaI-HF (#R3122), and 1µL of plasmid. A total volume of 10 µL was used for this reaction; the remaining volume was filled by water. The expected bands consisted of ~6800 bp, 2600 bp, 2000 bp, 1400 bp and 400 bp for $Ca_v3.2$ channel DNA in pcDNA3.1 vector backbones.

Once restriction digest reactions were completed, each reaction solution had a 6X loading dye mixed in; the volume added varied depending on the total reaction volume. For example, 2µL of the loading dye was added to the 10µL reactions. Each mixture was loaded onto a 1% w/v agarose gel containing 70 mL of Tris-acetate buffer, 0.70g of agarose (BioShop, #AGA001-250) and ethidium bromide (EtBr). A GeneRuler 1 kb Plus DNA ladder (ThermoFisher Scientific #SM1331) was also added as a standard. The agarose gel electrophoreses ran on a Bio-rad Power Pac200 power supply (Bio Rad, Mississauga, Ontario, Canada) set at 100 mV for 45 minutes. Gel bands were illuminated with a UV light source on an Alpha Innotech AlphaImager HP gel documentation system (San Leandro, California, USA). The banding pattern was visually inspected, and samples with the same, positive banding pattern were pooled together and stored at -20^{o}C.

v Gel Extraction and T4 DNA Ligase Reaction

For gel extractions, larger-volume restriction enzyme digests with larger quantities of DNA were completed. These digests consisted of 20-30 μg of plasmid DNA (between 15-40 μL), 8 μL of an NEB buffer, 8 μL of bovine serum albumin (BSA), and 3 μL of each restriction enzyme. A total volume of 80 μL was used for these reactions, the remaining volume was filled by water. All reactions were carried out in 0.2 mL PCR tubes incubated at 37^{o}C. In most cases, the vector DNA digest was treated with 1 μL of shrimp alkaline phosphatase (SAP; Thermo Fisher Scientific, # EF0651) for 30 minutes at 37^{o}C.

Once restriction digest reactions were completed, each mixture had 16 μL of a 6X loading dye added. Each mixture was loaded onto a 1% w/v agarose gel containing 150 mL of Tris-acetate buffer, 1.5g of agarose (BioShop, #AGA001-250) and ethidium bromide (EtBr). A GeneRuler 1 kb Plus DNA ladder (ThermoFisher Scientific #SM1331) was also added as a standard. The agarose gel electrophoreses ran on a Bio-rad Power Pac200 set at 100 mV for 45 minutes. Gel bands were illuminated with a UV light source on an Alpha Innotech AlphaImager HP gel documentation system.

An E.Z.N.A. ® gel extraction kit (Omega Bio-Tek, # D2500) was used to isolate purified DNA from the agarose gel. The protocol supplied with the gel extraction kit was used. After the extraction and DNA purification was complete, the concentration of digested DNA fragments was measured with the Nanodrop ND-1000 at the wavelength for maximal absorbance of DNA (A_{260}).

For ligation reactions, a 3:1 molar ratio of insert: vector was determined using a ligation calculator (http://www.insilico.uni-duesseldorf.de/Lig_Input.html). In some cases, a total

reaction volume of 30 µL was used. This required vector and insert DNA solutions, the volumes of which were determined using the ligation calculator. 3 µL of 10X Reaction Buffer (400 mM Tris-HCl, 100 mM MgCl2, 100 mM DTT, 5 mM ATP, pH 7.8) and 1 µL of T4 DNA Ligase (BioBasic # B1125) were added. The final volume was worked up to 30 µL with MilliQ water. When lower volumes of vector and insert DNA solutions were required, a 20 µL reaction volume was used. This required vector and insert DNA solutions, the volumes of which were determined using the ligation calculator. 2 µL of 10X Reaction Buffer and 1 µL of T4 DNA Ligase (BioBasic, #B1125) were added. The final volume was worked up to 20 µL with MilliQ water. These T4 DNA ligase reactions were incubated in an Eppendorf Mastercycler EP Gradient S on a program that held the temperature at 16^{o}C for 4 hours, and then lowered the temperature by 1^{o}C every half hour until 4^{o}C was reached. A negative control reaction without insert DNA was also run in parallel.

The following day, the ligation product and negative control DNA was transformed into *E. coli* cells and a mini-prep was performed (see section 1.1.3).

II Constructing T-type Calcium Channel Chimeras

This thesis project involved the characterization of snail LCa_v3 channel constructs with Domain IV turrets from $Ca_v3.2$ (α1H): LCa_v3-12a $DIV_{\alpha 1h}$, LCa_v3-12b $DIV_{\alpha 1h}$, and LCa_v3- $DII_{\alpha 1h}$ $DIV_{\alpha 1h}$. Omar Mourad constructed LCa_v3-12b $DIV_{\alpha 1h}$. From this construct and the wild-type LCa_v3-12a, I was able to construct LCa_v3-12a $DIV_{\alpha 1h}$. During my undergraduate thesis and NSERC: USRA project, I constructed LCa_v3- $DII_{\alpha 1h}$. From LCa_v3- $DII_{\alpha 1h}$ and LCa_v3- 12b

$DIV_{\alpha 1h}$, I was able to construct LCa_v3- $DII_{\alpha 1h}$ $DIV_{\alpha 1h}$. The strategy for constructing these channel chimeras is outlined in the following Section 1.21.

i Replacing DIV with $DIV_{\alpha 1hL}$ in pIRES2 containing LCa_v3- 12A

Swapping the DIV region from pIRES2- LCa_v3- $DIV_{\alpha 1hL}$ into pIRES2- LCa_v3- 12a allowed for the creation of pIRES2- LCa_v3- 12a $DIV_{\alpha 1hL}$. The DIV region within both of these cDNA sequences is flanked by restriction sites, SalI and MluI. The plasmids were digested with SalI-HF (#R3138) and MluI (#R0198) for extraction and ligation in NEB Buffer 3.1 (see section 3.I.v). Digestion of both plasmids resulted in bands at ~11600 bp and 2330 bp. From the digestion of pIRES2- LCa_v3-12a the band at ~11600 bp was extracted. From the digestion of pIRES2- LCa_v3- $DIV_{\alpha 1hL}$, the band at ~2330 bp was extracted. These two fragments were bound together using the T4 DNA Ligase reaction (see section 3.I.v) and then transformed into *E. coli* cells for cloning, isolation and purification of the plasmid DNA.

To ensure that the correct construct was cloned, two separate diagnostic restriction enzyme digests were done to confirm the identity of the pIRES2- LCa_v3- 12a $DIV_{\alpha 1hL.}$ The enzyme used in the first reaction was XhoI (#R0146) in NEB Buffer 3.1 (#B7203), because the insertion of $DIV_{\alpha 1hL}$ introduced another XhoI site. The positive banding pattern resulted in two bands at ~7600 bp and 6290 bp. The enzymes used in the second reaction were BamHI-HF (#R3136) and SalI-HF (#R3138) in Cutsmart® Buffer (#B7204). The positive banding pattern resulted in two bands at ~7600 bp and 6290 bp.

ii Replacing DIV with $DIV_{\alpha 1hL}$ in pIRES2:LCav3- $DII_{\alpha 1hL}$

Swapping the DIV region from the pIRES2 construct: LCa_v3- $DIV_{\alpha 1hL}$ into the pIRES2 construct LCa_v3- $DII_{\alpha 1hL}$ allowed for the creation of pIRES2- LCa_v3- $DII_{\alpha 1hL}$ $DIV_{\alpha 1hL}$. The DIV region within both of these cDNA sequences is flanked by restriction sites, SalI and MluI. The plasmids were digested with SalI-HF (#R3138) and MluI (#R0198) for extraction and ligation in NEB Buffer 3.1 (see section 3.I.v). Digestion of both plasmids resulted in bands at ~11600 bp and 2330 bp. From the digestion of pIRES2 construct, LCav3-$DII_{\alpha 1hL}$, the band at ~11600 bp was extracted. From the digestion of pIRES2 construct, LCav3- $DIV_{\alpha 1hL}$, the band at ~2330 bp was extracted. These two fragments were bound together using the T4 DNA Ligase reaction (see section 3.I.v) and then transformed into *E. coli* cells for cloning, isolation and purification of the plasmid DNA.

To ensure that the correct construct was cloned, two separate diagnostic restriction enzyme digests were done to confirm the identity of the pIRES2- LCa_v3- $DII_{\alpha 1hL}$ $DIV_{\alpha 1hL}$. The enzymes used in the first reaction were XhoI (#R0146), SalI-HF (#R3138) and AgeI (#R0552) in Cutsmart® Buffer (#B7204). The insertion of $DIV_{\alpha 1hL}$ introduced another XhoI site. The positive banding pattern resulted in bands at ~7600 bp, 3190 bp, 1990 bp, 1110 bp, and 13 bp (rarely visible). The enzymes used in the second reaction were SpeI (#R0133) and AgeI (#R0552) in NEB Buffer 1.1 (#B7201). The positive banding pattern resulted in bands at ~8210 bp, 2650 bp, 2490 BP, and 550 bp.

III Mammalian cell culture

Human embryonic kidney (HEK293T) cells were cultured in Dulbecco's modified Eagle's medium (DMEM; Sigma, D5796) supplemented with heat-inactivated 10% fetal bovine serum (FBS; Sigma, #F1051), 1% sodium pyruvate (Sigma, #S8636) and 250 μg/mL of penicillin/streptomycin (Sigma, #P4458). Media was pre- warmed in a 37°C water bath prior to use. All manipulations of HEK293T cells were performed under a laminar flow hood. Fetal bovine serum was heat-inactivated by a 56°C water bath incubation period of 30 minutes.

Human embryonic kidney cells (HEK293T) cells were received as a generous gift from Dr. Christophe Altier (University of Alberta) and were subsequently ordered from the American Tissue Culture Collection (ATCC® CRL-11268™). ATCC® CRL-11268 cells are constitutively expressed with simian virus 40 (SV40) large T antigen, and clone 17 was selected for its high transfectability.

i Freezing HEK cells

When the HEK293T cells were received from Dr. Altier (University of Calgary) and the American Tissue Culture Collection (ATCC® CRL-11268™), they had to be cultured, passaged, and then frozen for long-term storage in liquid nitrogen.

The cells were received from Dr. Altier and the ATCC frozen in cryopreservation vials. These cells were thawed in a 37^{o}C water bath for 1-2 minutes. Pre-warmed Dulbecco's Modified Eagle's Medium (DMEM; Sigma, #D5796) was added drop-wise to the vials, slowly diluting them with DMEM. The slow dilution ensured that the cells were not subjected to rapid changes

in osmotic pressure, because this could damage them. Once diluted in ~1 mL of DMEM, the cells were transferred to a tissue culture treated flask with a 25 cm^2 growth surface (Cell Star, VWR International # 82051-074) and diluted further to a total volume of 7 mL. The flasks were transferred to a HEPA-filtered 37^oC, 5% CO_2 incubator (ThermoFisher, Forma Series II #3110) and were allowed to grow for 3-4 hours. Following this brief incubation period, the media was removed from flasks and replaced with fresh 37^oC DMEM. The cells were placed back into the 37^oC, 5% CO2 incubator and were incubated for 2-3 days (until the cells were ~80% confluent in the flask).

When the cells reached ~80% confluence, they were transferred to larger flasks. The cells were removed from the incubator and the media was removed. Then, the cells were washed briefly with 1 mL of 0.25% trypsin EDTA to remove any excess DMEM; this was to ensure that there was not any DMEM present to dilute the trypsin to concentrations of inactivity. The trypsin was removed from the flask, and then 500 μL of 0.25% trypsin EDTA (Sigma, #T4049) was added to the flask, and then the flask was placed in the 37^oC, 5% CO_2 incubator for 2 minutes. After the brief incubation period the flask was removed from the incubator and the cells were viewed under the microscope to ensure that they were lifted sufficiently from the surface of the flask. Then 6 mL of DMEM was added to the flasks, and the cells were thoroughly mixed with the media and transferred to a tissue-culture treated flask with a 75 cm^2 growth surface (Cell Star, VWR International # 82050-856). 11 mL of fresh DMEM was added to the flask (total volume = 17 mL). This flask was incubated at 37^oC until the cells became ~80% confluent.

When the cells in the 75 cm^2 TC-treated flask reached ~80% confluence, they were split 1:5 into 5 different 75 cm^2 TC-treated flasks. The procedure for splitting HEK cells was outlined and visually demonstrated in a JoVE publication (Senatore et al., 2011). Following this protocol,

the cells were split into 5 flasks each with a total volume of 17 mL of DMEM and then incubated in 37^{o}C, 5% CO_2. When the cells reached ~60-70% confluence a VenorGeM® mycoplasma PCR test (Sigma-Aldrich # MP0025) was performed with a small amount of the media. The media in the flasks was also changed at this time, and the flasks were incubated for another 12-24 hours. When the cells in the TC-treated 75 cm^2 flask reached ~90% confluence, the flasks were observed using the light-microscope to ensure that there were no visible contaminants. The media was removed from the flasks, and then washed with 10 mL of 37^{o}C autoclaved phosphate-buffered saline (PBS). The PBS was removed and then the cells were trypsinized with 1 mL of 0.25% trypsin with EDTA, and incubated at 37^{o}C for 3-5 minutes (view cells under the microscope to ensure they have lifted off from the surface of the flask). 10 mL of DMEM without antibiotics was added to the flask, and the cells were mixed with the media by gentle pipetting. The cells and media were then transferred to a 15 mL Falcon tube.

In a refrigerated Beckman Coulter Allegra 25R centrifuge (Beckman Coulter Canada LP, Mississauga, Ontario, Canada) the cells were centrifuged at ~150 g for 5 minutes at 4^{o}C. After centrifugation, the media supernatant was removed from the Falcon tube and then 2 mL of cryopreservation media (10% DMSO [Dimethyl Sulfoxide, Sigma, #D2650], 50% FBS, 40% DMEM with no antibiotics) was added to the Falcon tube and the cells were resuspended, gently, in the cryopreservation media. 1 mL of cells in cryopreservation media were transferred to cryovials (ThermoFisher Scientific, #4000200) and then placed in an isopropanol freezing container (Nalgene® Cryo 1°C "Mr. Frosty" Freezing Container, Thermo Scientific, VWR International, #55710-200). The cells, inside the freezing container, were placed in the -80^{o}C freezer for ~24 hours. After ~24 hours the cells were transferred to liquid nitrogen for long-term storage.

ii Thawing HEK cells

HEK293T cells suspended in cryopreservation media were stored in 1 mL aliquots, frozen in liquid nitrogen for long-term storage. A new batch of HEK-293T cells were used after 20 to 30 passages, depending on the health of the cells. One aliquot of stored HEK293T cells in liquid nitrogen were thawed in a 37°C water bath rapidly (1- 2 minutes). 1 mL of pre-warmed DMEM media was mixed with the cells and placed in 5 mL of warm media in a 50mL, 25 cm^2 tissue culture flask (Cell Star, VWR International, # 82051-074). Afterwards, cells were incubated in a 37°C CO_2 incubator for 3-4 hours to facilitate the adherence of cultured cells. The media surrounding the cells were then replaced with 6 mL of fresh warm media and the cultured cells were placed back into the 37°C CO_2 incubator until fully confluent.

iii Cell culturing

The original protocol for HEK cell culturing and transfections was adapted from a JoVE online publication (Senatore et al., 2011), although some modifications were made. Cells were split bi-weekly from a monolayer that was ~80-90% confluent, typically to a 1:8 dilution on Monday and a 1:12 dilution on Thursday. However, sometimes the cells were growing more quickly and were split 1:20 on Monday and 1:20 on Thursday. The cells were split before they were ~90% confluent and only to passage numbers between 20-30 to ensure their electrophysiological stability (Thomas and Smart, 2005). To split the HEK-293T cells, media was aspirated and 1 mL of 0.25% Trypsin with EDTA (Sigma, #T4049) solution was added. The flask was inverted and gently rocked by hand to help de-attach the cells from the flask surface

and to remove any remaining DMEM (any remaining DMEM could dilute the trypsin solution). Then, the trypsin was removed and 500 µL of trypsin was applied directly onto the cells and the flask was incubated at 37°C, CO_2 incubator for 2 minutes. Afterwards, 6 mL of media was added to the flask to dilute and inactivate the trypsin, and the cells were re-suspended and mixed by pipetting up and down ~10 times. To achieve the desired split ratios, different ratios of cells to fresh media were added into a new flask. For maintenance, the cells were split at ratio of 1:8, 1:12, 1:16 or 1:20, depending on growth-rates and confluence. For transfections, cells were split to ratios of 1:4 for a same-day transfection, 1:6 for transfections done the following day, and 1:8 for transfections done two days after splitting. A 1:4 split (for a same-day transfection) from an ~80-90% confluent flask was carried out 4 hours prior to a transfection to allow for sufficient cell attachment and recovery.

iv Transfection of recombinant ion channels cDNA

A standard calcium phosphate protocol was used for transfections, which has been fully described in an online video experiment publication (Senatore et al., 2011). Typically, 1µg/mL of the ion channel cDNA in frame within an expression vector construct was introduced into HEK cells, for a total of 10µg of DNA in 600 µL of transfection solution in each flask.

Each transfection requires two 1.5 mL sterile microcentrifuge tube, one containing buffer and the other containing calcium ions. The ion channel construct DNA was added to a tube containing autoclaved MilliQ water and 30 µL of 2.5M $CaCl_2$, for a total volume of 300 µL. This calcium ion/DNA mixture was added to a second tube containing 300 µL of HES buffer. The contents of the first tube was added drop-wise to the HES buffer, and then the formation of

calcium phosphate crystals was facilitated by blowing air-bubbles with a pipette into the tube five times, and then pipetting the solution to mix five times. The microcentrifuge tube containing the calcium phosphate treated plasmids was left to incubate for 20 minutes at room temperature before being added in a drop-wise zigzag motion [See JoVE video (Senatore et al., 2011)] into the flask; the zigzag motion was to ensure that the local concentration of calcium phosphate within the flask did not exert unfavourable osmotic pressure on the cells. Then, the flask containing media was incubated overnight in a 37°C CO_2 incubator.

The next day, the transfected flask was washed three times with warm media to remove the calcium phosphate solution, which can be toxic to cells after prolonged exposure (Jiang and Chen, 2006). The flask was inverted, and the old media was aspirated and replaced with 6 mL of fresh DMEM pre-warmed at 37^{o}C. The flask was then slowly turned over, and rocked gently to cover the attached cells with media, and then the media was removed. This washing procedure was repeated three times, and then fresh DMEM was added to the flask. The flask was placed back into the 37°C CO_2 incubator for 2-4 hours, at which time the flask was transferred to a 28°C CO_2 incubator for several days. Incubation at 28°C facilitated the heterologous expression of the ion channel proteins, and limited the cell division of HEK293T cells. The time duration for incubation at 28°C depended on the efficiency of expression of the particular ion channels being expressed. Typically, snail LCa_v3 channels and the chimeras constructed from this channel were ready to record two days after transfection. Human $Ca_v3.2$ and other co-transfected channels required six days of incubation at 28°C before adequate expression was achieved for electrophysiological recording. Successful transfections of LCa_v3 channels and chimeras derived from LCa_v3 were confirmed using epifluorescence microscopy, because all LCa_v3 ion channels were contained in a bicystronic vector pIRES2-eGFP which expressed enhanced green

fluorescent protein (eGFP). $Ca_v3.2$ channels were co-transfected with eGFP in a modified pMT2 vector (pTRACER or pEGFP-C1), so successful co-transfections of this channel could also be assessed using an epifluorescence microscrope. Cells emitting a green fluorescence when exposed to mercury lamp excitation were an indicator of positive transfection of the ion channels.

v Plating transfected HEK cells for electrophysiological recordings

One hour prior to recording, transfected HEK cells were de-attached from the flask by trypsin enzyme. The same trypsinization procedure used to split cells in cell culturing (Section 3.III.iii) was used here. However, after the 37°C incubation, the cells were re-suspended in 10 mL of fresh media and plated onto uncoated circular glass coverslips for electrophysiological recording (Fischer Scientific, Circles No.1 – 0.13to 0.17 mm thick, size: 12mm, #12-545-80). Coverslips were placed in a 60 mm petri dish (Corning Life Sciences, #430166), 2.5 mL of fresh media and 2.5 mL of cells was added to each dish. Petri dishes were then placed in a 37°C CO_2 incubator for one hour, to allow the cells time to recover from trypsinization and become attached to the coverslips.

IV Electrophysiological Analysis and Solutions

In preparation for electrophysiological analysis, 35 mm petri dishes (Falcon, #3109617) were filled with an external bath solution. The external solution was dependent on the type of experiment to be carried out, and will be specified in the sections below. Coverslips containing attached cells were removed from the DMEM media contained in the 60 mm petri dishes prior to recordings, and then the coverslips were lifted by tweezers into the petri dish containing external bath solution. The ground electrode contained 1.25% agarose in 3M cesium chloride (CsCl) filled with 3M CsCl. Pipettes were pulled prior to recordings with a Sutter P-1000 micropipette puller containing a trough-shaped platinum filament (FB255B, 2.5 mm square x 2.5 mm wide) for Glass outer diameter < or equal to 2.0mm. An outer diameter of 1.5 mm and an inner diameter of 0.86 mm borosilicate capillary glass containing filament were used for pulling pipettes (Sutter Instruments, #BF150-86-15). Each pipette was fire polished with a microforge (Narishige, #MF-830). Internal recording solutions were used to fill the polished pipettes; like the external recording solutions, the internal solutions were dependent on the nature of the experiment being performed.

Whole cell patch clamp recordings were performed at room temperature. Recordings were obtained using an Axopatch 200B amplifier, sampled through a Digidata 1440a A/D converter to a PC computer. The pipette resistance was set between 2-5 MΩ. Only cells with a typical access resistance of <10 MΩ, recordings with minimal leak (<10%) and small current sizes (<1nA) were used for analysis. A holding potential of -110 mV was set for all protocols employed in this research. For all recordings, offline leak subtraction was carried out and data was filtered using a

500 Hz Gaussian filter in Clampfit 10.5. Microsoft Excel, SPSS, and Origin 9.1 were also used to manage and analyze the data.

i Characterization of basic kinetics

All recordings of basic kinetics for the channels studied in this thesis were obtained from cells bathed in 3 mL of an external solution containing 2mM $CaCl_2$, 160 mM tetraethylammonium chloride (TEA-Cl) and 10 mM 4-(2-hydroxyethyl)-1-piperazineethanesulfonic acid (HEPES), pH to 7.4 with TEA-OH. The internal solution for studying T-type channel kinetics contained 110 mM CsCl, 10 mM HEPES, 10mM ethylene glycol tetraacetic acid (EGTA) 3 mM MgATP and 0.6 mM LiGTP (pH to 7.2 with CsOH), and was filtered through a Nalgene 0.2 μm cellulose acetate syringe filter prior to use (Nalgene, #171). The internal and external solutions used in these protocols was described by Chemin et al. for their recordings of human T-type calcium channels (Chemin et al., 2002, 2001).

(a) Current-Voltage Relationships (I-V) and the Kinetics of Activation and Inactivation

To evaluate the voltage-dependent current responses of the channels in each cell recorded, a voltage-step protocol was used. This protocol began at the resting potential of -110 mV and increased by 5 mV per step from -100 mV to +80 mV. Current traces were observed on-screen in picoamps (pA) and were saved in .abf (Axon Binary File) format. Offline, these current traces were filtered and leak subtracted, and this data was used to determine current-voltage (I-V) relationships. This involved determining the peak inward or outward current at each voltage,

and then normalizing these currents to the maximal inward current over the entire range of voltage-steps (I/I_{max}). Plotting I/I_{max} for each voltage step produced an I-V curve. The peak of this curve was noted as a distinguishing property of the channel kinetics.

To determine the activation profile of the channel over the given voltage-range, the whole-cell conductance at each voltage step was calculated. The whole cell conductance is the rate of ions flowing across the membrane (presumably, through the channels). Whole-cell conductance can be calculated from the I-V data using the equation:

$$g = \frac{I}{\left(v_{command} - E_{rev}\right)} \qquad \text{Eq.1}$$

Where g is the whole-cell conductance, I is the normalized current at the given voltage-step, $V_{command}$ is the command voltage at the given voltage-step, and E_{rev} is the reversal potential determined from the IV curve. The reversal potential (E_{rev}), also known as the equilibrium potential, is the voltage at which the outward ion flux is equal to the inward ion flux – at this point, the detectable net flow of ionic currents through the cell membrane is zero. The linear portion of the I-V curve (for the channels studied herein, this was typically between +10 and +45 mV) was plotted to determine the slope (m) and y-intercept (b) using the equation y=mx +b (i.e., a linear fit), and the E_{rev} was determined at the abcissa when y = 0.

After determining the conductance, g, at each voltage step, the conductance was normalized to the maximal conductance over the entire range of voltage-steps ($G = g/g_{max}$). Then, a GV relationship was determined and plotted for each cell and. This was fitted to the Boltzmann equation to produce an activation curve:

$$activationcurve = \frac{g}{g_{\max}} = \frac{1}{\left(1 + e^{\frac{-v_{command} - v_{1/2}}{K}}\right)}$$ Eq. 2

$V_{1/2}$ represents half-maximal activation and K is the slope of the activation curve.

Using the data collected from each current-voltage (I-V) protocol, the time-to-peak activation (ms) and tau inactivation (τ_{inact}) were also determined. Time-to-peak activation is the time required for the average channel to activate following a depolarization, which is represented in whole-cell configuration by the net of those currents producing a maximal (i.e., peak) current for the trace. The time-to-peak is measured as the time from the capacitive transient (representing the onset of the voltage-step) to the peak of the current trace in milliseconds. The τ_{inact} is a time constant representing the decay of whole-cell current caused by inactivation of the channels. It is a measurement of the time required for the activated channels within a cell to inactivate to $1/e \cong 37\% \cong 1/3$ of their peak state. It is measured as a function of the exponential decay of a whole-cell current, from the peak back to baseline (~0 current). The portion of decay is fit to the following standard exponential equation in Clampfit 10.5:

$$f(x) = \sum_{i=1}^{n} A_i e^{-t/\tau_i} + C$$ Eq .3

To determine the steady-state inactivation kinetics, another voltage-step protocol was employed. This protocol involves a voltage step (-40 mV) to peak (peak #1) followed by a long period at a holding pre-pulse level (-110 mV for 10 seconds). This provides a maximal peak current measurement to be used in comparisons. Following the 10 second holding period, the channels in the cell should be fully recovered from inactivation. Then, a pre-pulse voltage step is applied, followed immediately by another step to peak (peak #2). The pre-pulses range from -105 mV to -35 mV in 5 mV increments. The pre-pulse activates a population of channels, and then these channels enter the refractory state of inactivation and are unable to be recruited during the second step to peak. The current generated from peak #2 is expressed as a percentage of peak #1, i.e. I/I_{max} where I is the current of peak #2 (after the pre-pulse) and I_{max} is the current generated at peak #1. The I/I_{max} values from each sweep are plotted against the pre-pulse potentials for those sweeps. The fraction of maximal currents generated from the steady state inactivating pre-pulse was fitted with the Boltzmann equation:

$$h_{\infty}(V) = \frac{1}{\left(1 + e^{\frac{-V_{command} - V_{1/2}}{K}}\right)} \quad \text{Eq. 4}$$

Where $V_{1/2}$ is the half-maximal inactivation and K is the slope of the inactivation curve.

(b) Recovery from inactivation

Recovery from inactivation measures the time it takes for the average ion channel to recover from a refractory state. The recorded cell is subjected to a depolarization step that produces the peak current (i.e., -40 mV), which maximally activates ion channels (peak #1). Following activation, the channels enter a refractory state i.e. they inactivate. Then, after a given recovery period, the cell was subjected to a second depolarization to -40 mV (peak #2). The durations of the recovery periods varied between sweeps; these periods were (in ms) 10, 25, 50, 100, 150, 200, 250, 375, 500, 750, 1000, 1250, 1500, 2000, 2500, 3000, 35000, 4000, 6000, and 8000 ms. During the waiting period between pulses, the ion channels recover from inactivation at -110 mV for 10 seconds. The maximal currents generated by peak #2 (following the recovery period) can be expressed as a percentage of the maximal current at peak #1. This provides an approximation of the proportion of channels that were able to recover from inactivation in the given recovery period. In general, the relationship between the proportion of recovered channels and the given recovery periods is fitted with an exponential function.

(c) Deactivation

Deactivation refers to the measurement of the rate of ion channel closure from their open state. Due to the effects of inactivation on the channels, measuring rates of deactivation is achieved by measuring the rate of decay of "tail currents" (Carbone and Lux, 1987; Matteson and Armstrong, 1986). In the deactivation protocol, the cell is subject to a step depolarization to generate its peak current, which will results in maximal activation of the channels. Once

maximally opened, the cell is subjected to a range of hyperpolarizing steps to differing potentials. Because of the increase in driving force with steps to lower potentials, a “tail current" is visible. At this point, inactivation has not occurred to any significant degree, so the measurement of the decay of the tail current at differing hyperpolarized potentials is the rate of the channels migrating from the open to the closed state (i.e., deactivation). The hyperpolarizing potentials used in this protocol were between -110 mV and 0 mV in 10 mV increments. The time constants (τ_{deac}) from the decay of the tail currents are measured by a standard exponential equation (Eq. 3):

$$f(x) = \sum_{i=1}^{n} A_i e^{-t/\tau_i} + C$$

These time constants (τ_{deac}) in milliseconds (ms) were plotted against the values of the hyperpolarizing potentials in millivolts (mv).

ii Investigating ion selectivity and permeability in Ca_v3 channels in HEK293T cells

In order to test the hypothesis of this research, it was necessary to conduct valid experiments to determine the ion selectivity properties of the chimeric and mutated voltage-gated ion channels. Ideally, these experiments could detect changes in monovalent ion permeability vs. divalent ion permeability with high sensitivity and reproducibility, and could suggest

mechanisms responsible for any changes observed. Furthermore, the results of such experiments had to be compared to the wild-type channels (LCa_v3-12a, LCa_v3-12b, $Ca_v3.2$), mutant channels (LCa_v3-12b $DII_{\Delta cys}$ and LCa_v3-12a $DII_{\Delta cys}$), and chimeric channel (LCa_v3- $DII_{\alpha 1hL}$) that were previously recorded and analyzed by Adriano Senatore and Wendy Guan. Three experimental conditions met these criteria and were utilized for this research; these are permeability experiments using $Ca^{2+}/NMDG^{+}$ versus Ca^{2+}/Na^{+} external solutions, bi-ionic reversal potential experiments, and the $[Ca^{2+}]_{ex}$ dose-response with 60 mM $[Na^{+}]_{ex}$ - a modified version of the anomalous mole fraction effect to detect changes in the degree that calcium blocks sodium permeability at the pore (Almers and McCleskey, 1984; Senatore et al., 2014).

The $Ca^{2+}/NMDG^{+}$ versus Ca^{2+}/Na^{+} permeability experiments and the experiments to determine the calcium-dependent block of sodium currents required perfusion. The various external solutions were fed into different lines flowing by gravity across the cells, under the control of a Valvelink8.2® controller, with Teflon valves (AutoMate Scientific, Berkeley, CA) used to toggle between the solutions.

(d) Inward Sodium Permeability Experiments

The channels' permeability to sodium was investigated using $Ca^{2+}/NMDG^{+}$ versus Ca^{2+}/Na^{+} experiments. External calcium ion concentrations are kept consistent in both solutions at 2 mM. In the presence of external calcium, high voltage-activated calcium channels are highly calcium selective, and lacking any permeability to external sodium ions. The degree of sodium selectivity can be gauged in the substitution of sodium ions with equimolar NMDG, a large, and weakly permeating monovalent ion.

External solutions to measure sodium selectivity were perfused to transfected cells patch clamp recorded in the whole-cell configuration to voltage-steps capable of generating peak currents (i.e., -40 mV). These voltage-steps were repeated every 10 seconds, with a holding potential of -110 mV between sweeps. While recording the peak currents, the cells were bathed in Ca^{2+}/$NMDG^{+}$ external solution or Ca^{2+}/Na^{+} external solution. A minimum of three stable sweeps were obtained with each external solution before switching to the next solution. The order of the solutions was altered from one recording to the next, to ensure that the sequence of the solutions was not having an effect on peak-current sizes observed. For example, if starting with Ca^{2+}/$NMDG^{+}$ and then switching to Ca^{2+}/Na^{+} for one cell, then the second cell would be bathed in Ca^{2+}/Na^{+} first followed by Ca^{2+}/$NMDG^{+}$.

After collected the data for sweeps in each solution, the peak current of Ca2+/Na+ was divided by the peak current of Ca2+/NMDG+ to determine the fold increase in current size when Na+ is introduced. This provided an approximation for the inward sodium permeability of each channel.

The solutions used in recording are summarized in Table 3.1.

Table 3.1 Inward Sodium Permeability Experiments: External and Internal Solutions

External

$CaCl_2$	NaCl	$NMDG^+$	TEA	HEPES
2	0	135	25	10
2	135	0	25	10

pH 7.4 with TEA-OH

Internals

#	CsCl	$NMDG^+$	EGTA[#]	Mg-ATP	Li-GTP	HEPES
1	110	0	10	3	0.6	10

[1]**pH 7.2 with CsOH**

From (Senatore et al., 2014)

(e) Bi-ionic Reversal Potential Experiments

The bi-ionic reversal potential is used to measure the relative permeability of an inward calcium current (with 2 mM external calcium) compared to the relative permeability of outward monovalent ions (with 100 mM external monovalent ion). In these conditions, the cell in whole-cell configuration is subjected to an I-V protocol (See section 3.IV.i.a) to generate a current-voltage (I-V) relationship curve. The higher the permeability of the monovalent ions, the larger the outward monovalent ion current compared to the inward calcium current. The reversal potential is a good indicator of relative permeability and is used as a factor in the following equation (Eq. 5) to calculate the approximate relative permeability.

$$\frac{P_{Ca}}{P_X} = \frac{[X]_i}{4[Ca]_o} \exp\left(\frac{E_{rev}F}{RT}\right)\left\{\exp\left(\frac{E_{rev}F}{RT}\right)+1\right\} \quad \text{Eq. 5}$$

Where [X] is the concentration of the monovalent ion, [Ca] is the concentration for calcium, E_{rev} is the reversal potential, F is the Faraday constant (9.65 ×104 C mol−1), R is the universal gas constant (8.31 J K−1 mol−1) and T is absolute temperature, at 298K. See section 1.4.1.1 on how to calculate E_{rev}.

Four different monovalent ions were tested, lithium (Li^+), sodium (Na^+), potassium (K^+) and cesium (Cs^+). See Table 3.2 for a list of internal and external solutions.

Table 3.2 Bi-ionic solutions for reversal potential experiments

External

$CaCl_2$	TEA-Cl	HEPES
4	155	10

pH 7.4 with TEA-OH

Internals

#	CsCl	NaCl	KCl	LiCl	EGTA[#]	TEA-Cl	HEPES
1	100	0	0	0	10	10	10
2	0	100	0	0	10	10	10
3	0	0	100	0	10	10	10
4	0	0	0	100	10	10	10

pH 7.2 with XOH where X= Cs, Na, K, or Li.

[#] pH 8.0 with XOH

From (Senatore et al., 2014)

(f) $[Ca^{2+}]_{ex}$ dose-response with 60 mM $[Na^{+}]_{ex}$

The anomalous mole fraction effect was first observed by Almers and McCleskey in 1984 with skeletal muscle from frogs (Almers and McCleskey, 1984). The results of this experiment are used to approximate the consequences of calcium ions competing with sodium ions for permeation through the pore. This experiment was performed to determine the degree of calcium block of the sodium current. This study required the perfusion of differing concentrations of external calcium solutions using a gravity-flow perfusion system. Solutions

were prepared from low $[Ca^{2+}]_{ex}$ (1 x 10^{-9} M) to high $[Ca^{2+}]_{ex}$ (1 x 10^{-2} M), each in the presence of 60 mM external sodium. The internal and external solutions can be found in Table 3.3. To test which voltage step level generated the peak current, the cell is stepped to a range of voltage close to its peak (usually +/- 20 mV) in 10 mV increments (e.g., -65 mV, -55 mV, -45 mV, -35 mV, and -25 mV). This is because the channels within the cell respond differently to depolarizations depending on the $[Ca^{2+}]_{ex,}$ and this results in the peak occurring at different voltage-steps depending on which solution the cell is exposed to. It is believed that differing external divalent ion concentrations provide external ionic shielding that biases the voltage sensor, shifting the voltage-dependence of activation.

After a set of five sweeps, solutions were switched. To clarify, for example, the solution of 1 x 10^{-9} M external calcium was washed over the cell for five sweeps (e.g., -65 mV → -25 mV in 10 mV increments) before the solution was switched. The concentrations of free calcium in the external solutions were calculated using the following website: http://maxchelator.stanford.edu/CaEGTA-TS.htm.The peak current for each solution was divided by the largest current overall to obtain the fraction of maximal current (I/I_{max}) value of differing calcium solutions. These I/I_{max} results were plotted against $[Ca^{2+}]_{ex}$ to visualize the calcium-dependent block of the sodium current (at 60 mM external sodium).

Table 3.3 $[Ca2+]_{ex}$ dose response with 60 mM $[Na+]_{ex}$

External

in mM	Ca^{2+} free	$CaCl_2$	NaCl	EGTA	HEPES	Glucose
1	$1x10^{-9}$	0.01	60	1.246	10	26.3
2	$1x10^{-7}$	1.00	60	2.236	10	20.4
3	$1x10^{-5}$	1.00	60	1.002	10	24.1
4	$1x10^{-4}$	0.10	60	0	10	29.7
5	$3x10^{-4}$	0.30	60	0	10	29.1
6	$1x10^{-3}$	1.00	60	0	10	27.0
7	$3x10^{-3}$	3.00	60	0	10	21.0
8	$1x10^{-2}$	10.00	60	0	10	0.0

pH 7.4 with TEA-OH

Internal

CsCl	EGTA	Mg-ATP	Li-GTP	HEPES
110	10	3	0.6	10

pH 7.4 with CsOH

From (Senatore et al., 2014)

iii Statistical Analyses

Numerical values in all electrophysiological experiments were compared using a parametric one way ANOVA when three or more data sets were compared in SPSS. If the one way ANOVA results were statistically significant, a Student-Newman-Keuls *post hoc* test was performed and reported, unless otherwise stated. Alternatively, a one-way ANOVA with summary data was performed utilizing the free statistics calculator found at http://www.danielsoper.com/statcalc/calculator.aspx?id=43

4. Results

Prior to the initiation of this MSc thesis project, Dr. David Spafford and Dr. Adriano Senatore isolated and characterized the T-type calcium channel from the pond snail, *Lymnaea stagnalis*, which is referred to as LCa_v3. As a part of his doctoral thesis, Dr. Senatore discovered that *L. stagnalis* expresses two isoforms of the LCa_v3 channel, dubbed LCa_v3-12a and LCa_v3-12b (Senatore et al., 2014). Together, Dr. Senatore and Wendy Guan performed electrophysiological recordings of LCa_v3-12a and LCa_v3-12b with heterologous expression in HEK293T cells, and determined that LCa_v3-12a is essentially a sodium-selective channel, while LCa_v3-12b is a more conventional T-type calcium channel with relatively low sodium-permeability. Sequence analysis revealed that the Domain II extracellular turrets upstream of the pore selectivity filter (or S5-P / L5 region) of these channel isoforms differ in length and cysteine contribution. They are also markedly different than the Domain II turret sequences found in the human $Ca_v3.1$, $Ca_v3.2$, and $Ca_v3.3$ channels.

Wendy Guan explored mutants in which the cysteine residues in Domain II of LCa_v3 have been substituted with alanine residues (LCa_v3-12a ΔCys and LCa_v3- 12b ΔCys) and a chimera in which the Domain II L5 turret of LCa_v3 has been replaced by the Domain II turret from $Ca_v3.2$ (LCa_v3- $DII_{\alpha 1hL}$). I created these mutants as an undergraduate in Dr. Spafford's laboratory. Compared to the wild-type channels, these mutagenized and chimeric channels display significantly different ion selectivity (Guan, 2014).

I Alternative Splicing in Domain II and Domain IV

Dr. Spafford explored the transcriptome and genomic sequences of animals in all major animal phyla and created sequential alignments of Ca_v3 channels. Upon examination of these sequences, Dr. Spafford observed that some invertebrate organisms uniquely possess two genes for T-type channels (most organisms outside of vertebrates only have one T-type channel gene). This means that LCa_v3 is not the only invertebrate organism to possess multiple versions of its T-type channel (i.e., LCa_v3-12a and LCa_v3-12b). Genomes from the organisms of *Macrostomum* and *Strigamia*, for example, suggest that these animals also possess two versions of the Ca_v3 channel, with differences in Domain II (Figures 1.15 and 1.18). Like *L. stagnalis,* the Ca_v3 channel genes within these organisms are different in their Domain II L5 turret sequences; one version is a tri-cysteine configuration (CxxC…C) in exon 12a, which is shorter in overall size, and the other is a penta-cysteine (C…CxC…CxC) arrangement in exon 12b, which is an average of ~13 amino acids longer (Senatore et al., 2014). All nematodes have a different pentacysteine arrangement (CxxC..C...CxC) in exon 12b.

Uniquely, species within the class of anthozoans (e.g., coral and sea anemones) and within the class of scyphozoans (jellyfish) have two Ca_v3 genes which are different from one another due to variations in their Domain IV turret sequences. Anthozoans and scyphozoans are within the phylum of cnidarians. These two different channel genes in cnidarians differ in the size and number of cysteines in the Domain IV turret downstream of the pore selectivity filter (or P-S6 / L6 region). Like in Domain II, the Domain IV sequences have conserved patterns of cysteine residues (Figures 1.16 and 1.18). One version of the Domain IV L6 sequence has a di-cysteine arrangement (C…C) and another version is typically longer by ~2 amino acids and has a

quatra-cysteine configuration (CxxxxxCxxCC). Both Domain II L5 and Domain IV L6 flank the sides of the re-entrant pore (Figures 1.21, 1.23, 1.24).

Given that, most commonly, invertebrate T-type channels with variable extracellular turrets usually have two versions of either Domain II L5 or Domain IV L6, in this thesis project we explored the influences that Domain II L5 and Domain IV L6 turret sequences might have on ion selectivity and permeability. This was achieved by swapping DII-DIV turrets from calcium-selective human $Ca_v3.2$ channels into snail LCa_v3 channels to create chimeras. Through the generation and analyses of turret chimeras we could evaluate the relative contribution of Domain II L5 and Domain IV L6 turrets as determinants for calcium and sodium selectivity. The first of these channels, LCa_v3-12b $DIV_{\alpha 1hL}$, was created by Omar Mourad – a fourth year project student in the Spafford lab. Turret chimeras with the Domain II turret sequences cloned into $Ca_v3.2$ (i.e., $Ca_v3.2$-12a and $Ca_v3.2$-12b) are discussed briefly; these clones were created by Amrit Mehta, an MSc student in the Spafford lab.

II Construction of LCa_v3 Chimeras

Dr. David Spafford designed synthetic oligonucleotide cassettes to be inserted into pBlueScript- LCa_v3 subclones. These oligonucleotides were ordered from BioBasic Canada. The sequences of these oligonucleotides can be found in Appendix I. After creation of the pBlueScript- LCa_v3 DIV subclones, the LCa_v3 inserts (now with the synthetic oligonucleotide sequence in the desired regions) were cloned back into the full length LCa_v3 cDNA sequences (in pIRES2-eGFP expression vectors). For creating pIRES2-eGFP- LCa_v3- $DII_{\alpha 1hL}$ $DIV_{\alpha 1hL}$, the creation of a subclone was not necessary. The final constructs were digested with restriction

enzymes, and then the digestion products were loaded into agarose gels for gel electrophoresis. The resultant banding patterns are found in Figures 4.1, 4.2, and 4.3. All banding patterns were as expected, based on computer generated results in Gene Construction Kit (See Appendix). Therefore, the results were positive and the chimera LCa_v3 channel cDNAs were evaluated for their ion selectivity and other characteristics in recordings of transfected HEK293T cells.

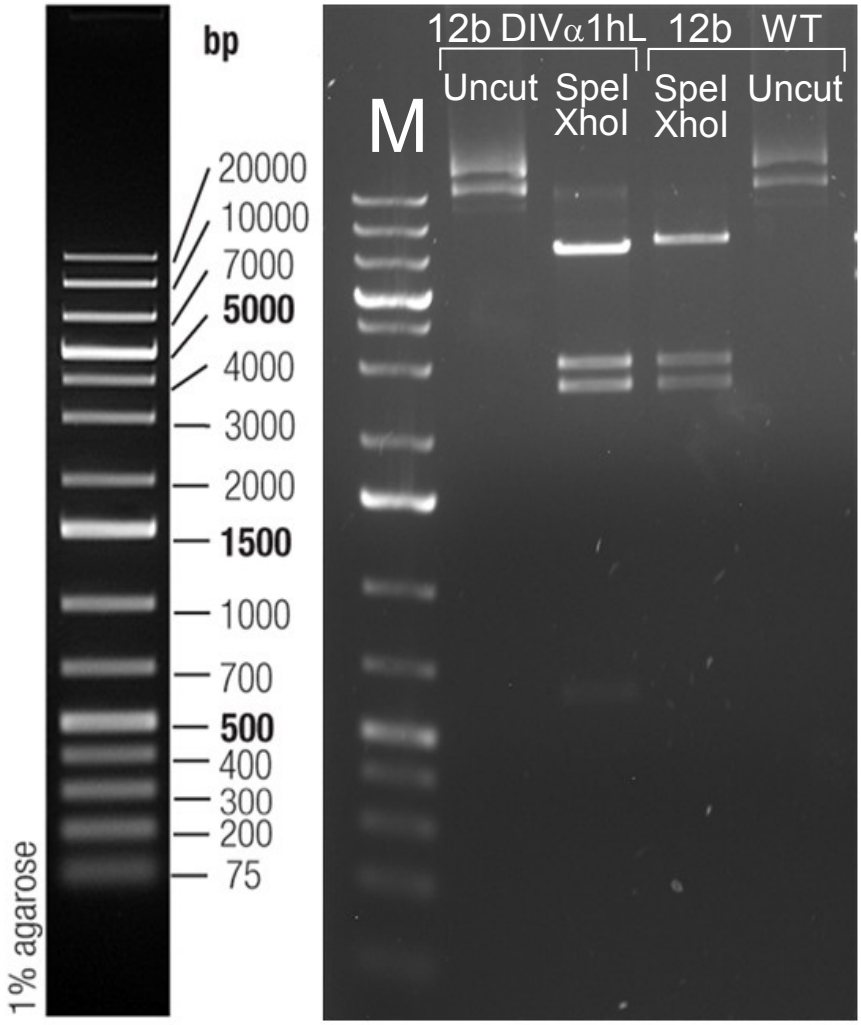

Figure 4.1 Gel Electrophoresis Image after a Restriction Enzyme Digest of LCa_v3-12b $DIV_{\alpha 1hL}$ with SpeI and XhoI

The successful cloning of LCa_v3-12b DIVα1hL was confirmed by restriction analysis. The cDNA of the full-length chimeric channel (pIRES2-eGFP- LCa_v3-12b $DIV_{\alpha 1hL}$) was digested with SpeI and XhoI in CutSmart ® Buffer from New England BioLabs. The wild-type LCa_v3-12b cDNA was used as a negative control. Uncut cDNA was run in parallel for both plasmids. The expected banding pattern is based on results obtained from Gene Construction Kit Version 3.0. The expected bands for LCa_v3-12b $DIV_{\alpha 1hL}$ digested with SpeI and XhoI are: 7610 bp, 3063 bp, 2639 bp, and 615 bp. The marker (M) is GeneRuler 1 kb Plus DNA Ladder.

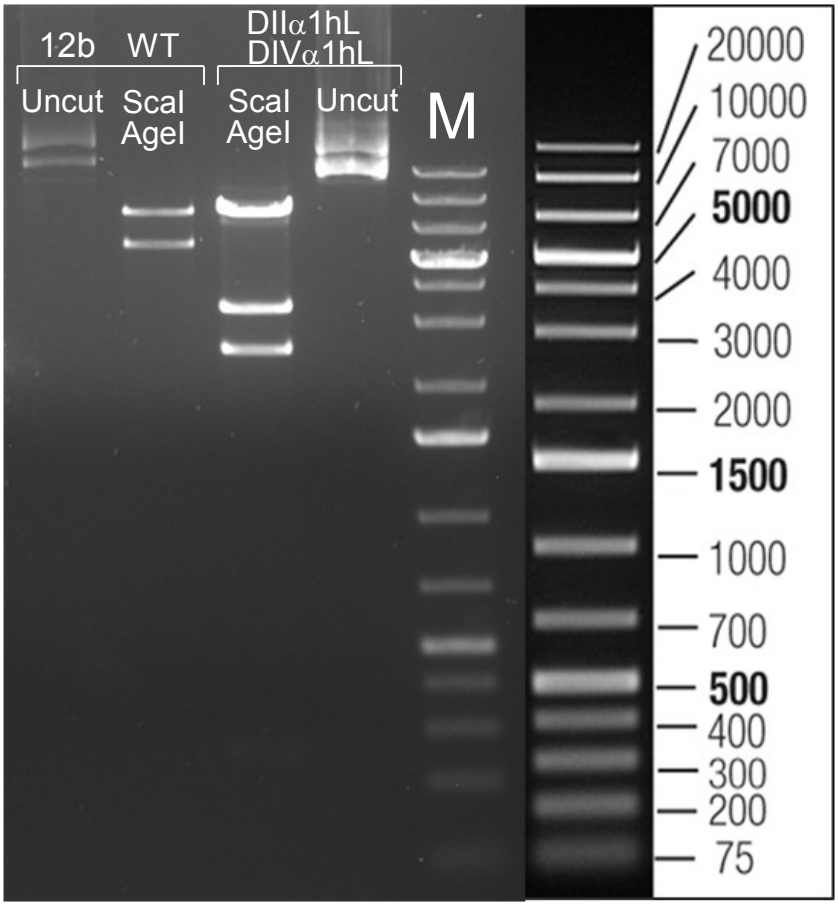

Figure 4.2 Gel Electrophoresis Image after a Restriction Enzyme Digest of LCa_v3-$DII_{\alpha 1hL}$ $DIV_{\alpha 1hL}$ with ScaI and AgeI

The successful cloning of LCa_v3-$DII_{\alpha 1hL}$ $DIV_{\alpha 1hL}$ was confirmed by restriction analysis. The cDNA of the full-length chimeric channel (pIRES2- eGFP-LCav3-$DII_{\alpha 1hL}$ $DIV_{\alpha 1hL}$) was digested with ScaI-HF and AgeI-HF in CutSmart ® Buffer from New England BioLabs. The wild-type LCa_v3-12b cDNA was used as a negative control. Uncut cDNA was run in parallel for both plasmids. The expected banding pattern is based on results obtained from Gene Construction Kit Version 3.0. The expected bands for LCa_v3-$DII_{\alpha 1hL}$ $DIV_{\alpha 1hL}$ digested with SpeI and XhoI are: 8028 bp, 3198 bp, 2431 bp, and 241 bp. The marker (M) is GeneRuler 1 kb Plus DNA Ladder.

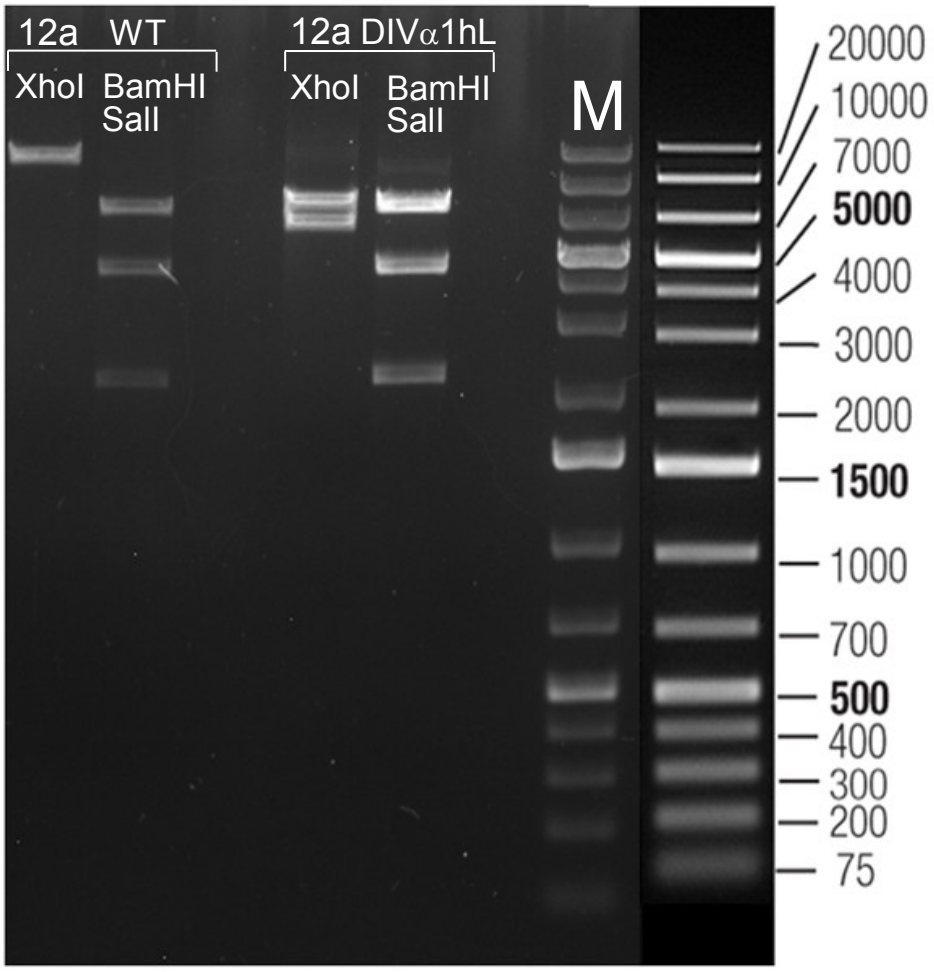

Figure 4.3 Gel Electrophoresis Image after a Restriction Enzyme Digest of LCa_v3-12a $DIV_{\alpha 1hL}$ with BamHI and SalI, and XhoI

The successful cloning of LCa_v3-12a $DIV_{\alpha 1hL}$ was confirmed by restriction analysis. The cDNA of the full-length chimeric channel (pIRES2- eGFP- LCav3-12a $DIV_{\alpha 1hL}$) was digested with BamHI/SalI-HF in CutSmart ® Buffer, and was digested in a separate reaction with XhoI in NEB3.1 Buffer. The wild-type LCa_v3-12a cDNA was used as a negative control. The expected banding pattern is based on results obtained from Gene Construction Kit Version 3.0. The expected bands for LCa_v3-12a $DIV_{\alpha 1hL}$ digested with BamHI and SalI are: 7383 bp, 4343 bp, and 2201 bp. The expected bands with XhoI are: 7610 bp and 6312 bp. The marker (M) is GeneRuler 1 kb Plus DNA Ladder.

III Comparisons of Ion Selectivity and Permeability

i Inward Sodium Permeability Experiments: $Ca^{2+}/NMDG^{+}$ versus Ca^{2+}/Na^{+}

In general, compared to the wild-type channels, the chimeric LCa_v3 calcium channels had altered ion selectivity for calcium and sodium; this was readily apparent from the results of the $Ca^{2+}/NMDG^{+}$ versus Ca^{2+}/Na^{+} experiments. For a summary of the results of this experiment, refer to Figure 4.4. All values reported herein are averages ± standard error of the mean (S.E.M). All values can be found in the table in Figure 4.4C.

The addition of Ca^{2+}/Na^{+} led to an increases in current size for all channels investigated, and the fold-increase ranged from 1.27 (± 0.09) in $Ca_v3.1$ channels to 19.83 (± 0.71) in LCa_v3-12a ΔCys. Of the human channels, $Ca_v3.2$ is of particular importance to the objectives of this thesis because it was used as a donor in the turret swaps. The $Ca_v3.2$ channel has relatively high calcium selectivity, passing ~3/4 to 4/5 of its current as calcium ions. LCa_v3-12a, on the other hand, is very permeant to sodium ions (~90% of the current was due to permeating Na^{+}); it is the most sodium permeant of the wild-type T-type channels under consideration. The LCa_v3-12b channel has a 2.53 fold current increase when Na^{+} replaces $NMDG^{+}$ (50:50 Ca^{2+} and Na^{+}). Interestingly, the chimera LCa_v3- DII_{a1hL} is more calcium selective than LCa_v3-12a but less calcium selective than LCav3-12b (Guan, 2014). LCa_v3- DII_{a1hL} is almost exactly between LCa_v3-12b and LCa_v3-12a in terms of current increase with an 8.09 (± 0.8) fold current increase in Ca^{2+}/Na^{+} versus $Ca^{2+}/NMDG^{+}$ (passing ~ 3/4 of its current as Na+). This result was the first in which we demonstrate that adding DII and/or DIV turrets from the human $Ca_v3.2$ channel can dramatically alter calcium-selectivity in LCa_v3 (Guan, 2014). It should be noted that cysteine-to-alanine substitutions in Domain II resulted in significantly higher sodium permeability compared

to the corresponding wild-types. LCa_v3-12a ΔCys (replacement of tricysteine to monocysteine configuration in LCav3-12a) was the most sodium permeant channel, with a fold-increase of 19.83 (± 0.71); this is a significant increase over LCa_v3-12a ($P<0.05$). LCa_v3-12b ΔCys (replacement of pentacysteine to monocysteine configuration in LCa_v3-12b with a current fold-increase of 3.42 ± 0.17) has significantly greater sodium permeability compared to LCa_v3-12b (2.53 ± 0.1; $P<0.01$). See Guan 2014 for a complete discussion of the ΔCys mutants.

Replacing the Domain IV L6 turret region of the LCa_v3 channels with the Domain IV turret from $Ca_v3.2$ invariably resulted in decreased inward sodium permeability. Compared to the wild-type LCa_v3-12b (2.53 ± 0.1), the LCa_v3-12b $DIV_{\alpha 1hL}$ chimera has significantly greater calcium-selectivity (1.47 ± 0.04; $P<0.01$). For LCa_v3-12a $DIV_{\alpha 1hL}$ the fold-increase in current is 6.52 ± 0.32, which reflects much weaker sodium selectivity compared to wild-type LCa_v3-12a; LCa_v3-12a possesses a fold-increase in Ca^{2+}/Na^{+} compared to $Ca^{2+}/NMDG^{+}$ of 15.4 ± 0.83 ($P<0.05$). Replacing the Domain IV turret sequence of the LCa_v3-$DII_{\alpha 1hL}$ channel with $DIV_{\alpha 1hL}$ sequence created the double-turret chimera, LCa_v3- $DII_{\alpha 1hL}$ $DIV_{\alpha 1hL}$. LCa_v3- $DII_{\alpha 1hL}$ $DIV_{\alpha 1hL}$ had a 3.01 ± 0.13 fold-increase upon addition of sodium ions, which is a dramatically higher preference for calcium ions compared to LCav3- $DII_{\alpha 1hL}$ (8.09 ± 0.8; $P<0.01$).

The current traces, bars, and table rows in Figure 4.4 are colour-coded according to the DII turret character of the channels, and this highlights the observations that all DII-12b channels (orange) are more calcium selective than all DII-12a channels (red). In Figures 4.9 to 4.13, the relationships between the chimeras, delta-cysteine mutants and wild-type channels are explored in greater detail. Organizing the data in the way presented in Figures 4.9 to 4.13 highlights the changes that alterations in the turrets confer onto the channels.

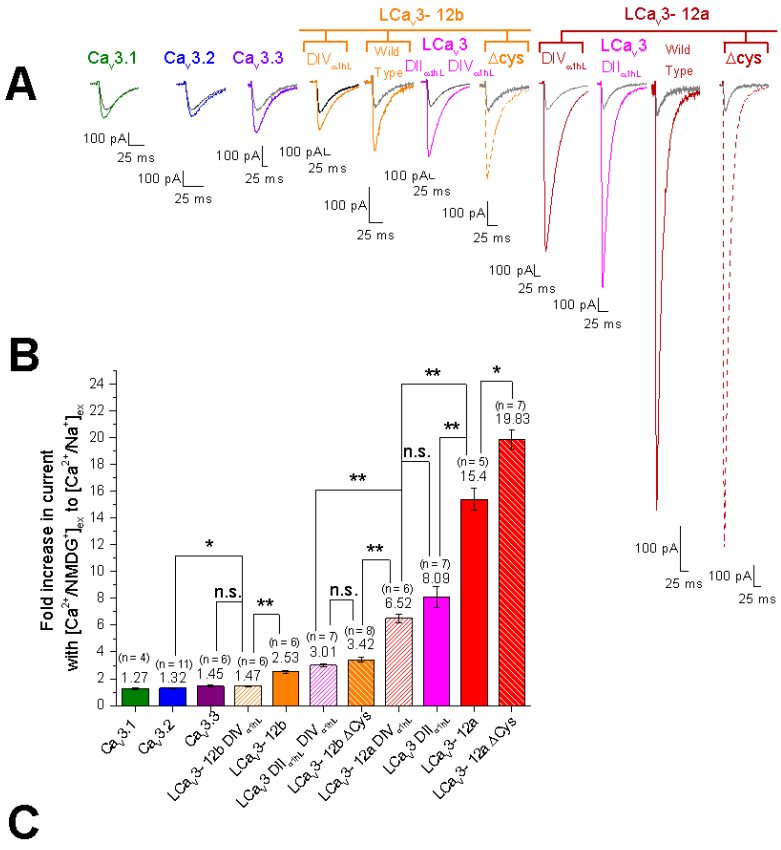

	Increase	SEM	N
$Ca_V3.1$	**1.27**	**0.09**	**4**
$Ca_V3.2$	**1.32**	**0.05**	**11**
$Ca_V3.3$	**1.45**	**0.08**	**6**
LCa_V3 12b $DIV_{\alpha 1hL}$	**1.47**	**0.04**	**6**
LCa_V3 12b	**2.53**	**0.1**	7
LCa_V3 $DII_{\alpha 1hL}$ $DIV_{\alpha 1hL}$	**3.01**	**0.13**	**12**
LCa_V3 12b ΔCys	**3.42**	**0.17**	**8**
LCa_V3 12a $DIV_{\alpha 1hL}$	**6.52**	**0.32**	**6**
LCa_V3 $DII_{\alpha 1hL}$	**8.09**	**0.8**	7
LCa_V3-12a	**15.4**	**0.83**	**5**
LCa_V3-12a ΔCys	**19.83**	**0.71**	7

Figure 4.4 Results of Inward Sodium Permeability Experiments in wild-type T-type Channels, Delta-Cysteine mutant T-type Channels, and chimeric T-type Calcium Channels

(A) Representative T-type currents from whole-cell patch clamp recordings, showing current increases when 2 mM Ca^{2+}/ 135 mM $NMDG^{+}$ (grey) is replaced by 2 mM Ca^{2+}/ 135 mM Na^{+} (colours). (B) Bar graphs displaying sodium permeability of channels and results of one-way ANOVA. (C) Table of average fold-increase in current when sodium replaces the impermeable ion $NMDG^{+}$ (approximation of sodium permeability). SEM = standard error of the mean.

ii Bi-Ionic Reversal Potential Experiments

Another method of investigating relative sodium permeability, besides determining the relative-fold-increase in current size in the presence of Na^+ and Ca^{2+} compared to $NMDG^+$ and Ca^{2+}, is to conduct bi-ionic reversal potential experiments. In this case, bi-ionic conditions involved measurements of monovalent ion flux (e.g., Na^+) as an outward current and calcium flux (Ca^{2+}) as an inward current. A relative change in the reversal potential from a more positive potential to a more negative potential reflects greater permeability of the outward transiting monovalent ion. On the other hand, a relative change in the reversal potential from a more negative potential to a more positive potential reflects a dominance of the inward calcium current relative to the outward monovalent ion (e.g., Na^+) current. Quantification of the relative permeability is calculated from the reversal potentials using the bi-ionic equation (Eq. 5), which generates relative permeability values, reported as $P_{Ca}/P_{X,}$ where X is a monovalent ion (Li^+, Na^+, K^+, or Cs^+).

Representative traces of the current-voltage relationship (I-V) curves gathered from recordings of LCa_v3-12a $DIV_{\alpha 1hL,}$ LCa_v3-12b $DIV_{\alpha 1hL,}$ and LCa_v3- $DII_{\alpha 1hL}$ $DIV_{\alpha 1hL}$ in conditions of 4 mM $[Ca^{2+}]_{ext}$ and 100 mM $[X^+]_{int}$, where X is the stated monovalent ion (Li^+, Na^+, K^+, or Cs^+) are shown in Figure 4.5. Generally, the largest outward currents appear in recordings of Li^+ and the outward currents progressively become smaller to Cs^+. This is the case in the wild-type channels, as well as in LCa_v3-12a ΔCys and LCa_v3-12b ΔCys. In Figure 4.6, I-V curves derived from recordings of the channels $Ca_v3.2$, LCa_v3-12a, LCa_v3-12b, LCa_v3- $DII_{\alpha 1hL}$, LCa_v3- $DII_{\alpha 1hL}$ $DIV_{\alpha 1hL}$, LCa_v3- 12a $DIV_{\alpha 1hL}$ and LCa_v3-12b $DIV_{\alpha 1hL}$ are shown. From these I-V curves, the reversal potential for each channel under each set of conditions was determined. The relative

permeabilities (calculated from the reversal potentials using the bi-ionic equation [Eq. 5]) are displayed in Table 4.1.

The relative permeability values, reported as P_{Ca}/P_X in Table 4.1, indicate the channels' preference for calcium ions versus monovalent ions. All of the channels, except for LCa_v3-$DII_{\alpha 1hL}$ $DIV_{\alpha 1hL}$, follow Eisenman's ion selectivity sequence (Eisenman et al., 1967) with monovalent ion permeabilities in the order of $Li^+ > Na^+ > K^+ > Cs^+$, corresponding to the increasing crystal radii of the monovalent ions (Li^+ = 0.60 Å, Na^+ = 0.95 Å, K^+ = 1.33 Å, Cs^+ = 1.69 Å). LCa_v3- $DII_{\alpha 1hL}$ $DIV_{\alpha 1hL}$ is unique in that it does not follow this selectivity sequence perfectly, instead having a sequence of $Li^+ > K^+ \approx Na^+ > Cs^+$.

The rank order of the channels in terms of average relative permeability can be observed in Table 4.1 as well, with statistically significant differences indicated in Table 4.2 (one-way ANOVA with $P<0.05$* or $P<0.01$**). Bar graphs constructed from this data can be found in Figures 4.9-4.13; these visual representations make it easier to identify relative permeability trends between conditions and between channels.

The P_{Ca}/P_{Na} relative permeabilities of the $DIV_{\alpha 1hL}$ chimeras are significantly different than their wild-type counterparts (Tables 4.1 and 4.2). With the Na^+ internal solution, LCa_v3-12b $DIV_{\alpha 1hL}$ is statistically more calcium-permeant than LCa_v3-12b (P_{Ca}/P_{Na} values of 63.58 ± 9.98 and 41.32 ± 0.75, respectively. $P<0.05$). LCa_v3-$DII_{\alpha 1hL}$ $DIV_{\alpha 1hL}$ has a significantly higher calcium permeability compared to LCa_v3- $DII_{\alpha 1hL}$, except when K^+ is the monovalent ion (e.g., P_{Ca}/P_{Na} values are 70.19 ± 3.66 versus 28.99 ± 1.82, $P<0.05$), and is also significantly different than the relative permeability values of LCav3-12a and LCav3-12b ($P<0.01$). LCa_v3-12a $DIV_{\alpha 1hL}$ also displays higher calcium-selectivity in bi-ionic conditions compared to LCav3-12a, where

Li^+ or Na^+ is the outward-moving monovalent ion. For example, the P_{Ca}/P_{Na} ratios for LCa_v3-12a $DIV_{\alpha 1hL}$ and LCa_v3-12a are, respectively, 41.98 ± 2.35 and 32.01 ± 0.71 ($P<0.05$).

Importantly, the P_{Ca}/P_X relative permeability ratios of LCa_v3-12b $DIV_{\alpha 1hL}$ and LCav3-$DII_{\alpha 1hL}$ $DIV_{\alpha 1hL}$ are not statistically different from those of $Ca_v3.2$ in most conditions (except for P_{Ca}/P_K). The P_{Ca}/P_X relative permeability ratios comparing the wild type channels $Ca_v3.2$ versus LCa_v3-12b are, however, significantly different (Guan, 2014; Senatore et al., 2014). The results indicate that replacing the Domain IV L6 turret from LCa_v3-12b with the Domain IV L6 turret of $Ca_v3.2$ lead to higher calcium selectivity in the channel and make them similar to $Ca_v3.2$.

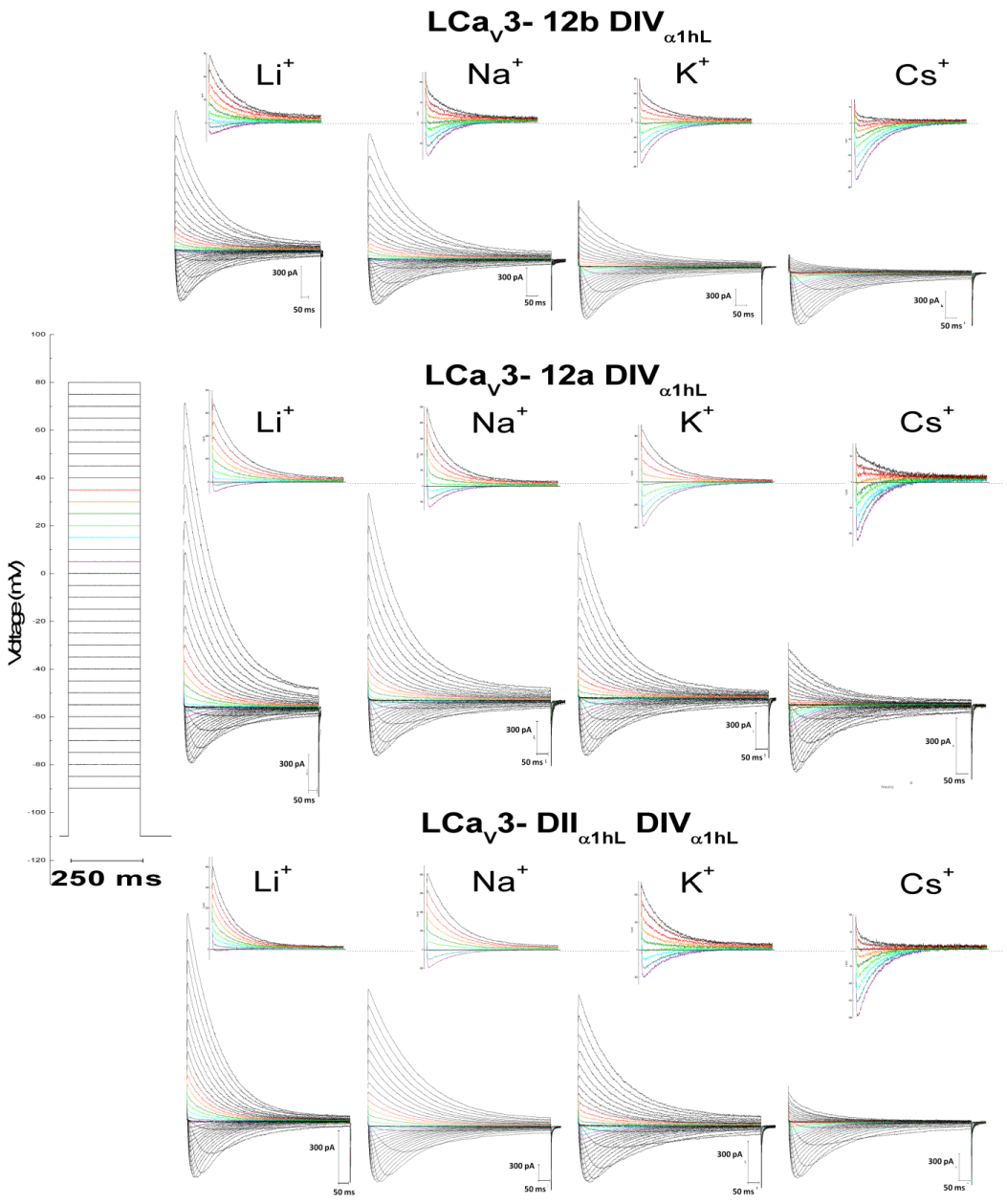

Figure 4.5 Monovalent ion (Li^+, Na^+, K^+ and Cs^+) permeability through chimeric T-type Calcium Channels LCa_v3-12b $DIV_{\alpha 1hL}$, LCa_v3-12a $DIV_{\alpha 1hL}$, and LCa_v3-$DII_{\alpha 1hL}$ $DIV_{\alpha 1hL}$

Inward calcium currents in 4 mM external calcium and outward monovalent T-type currents generated with 100 mM of internal Li+, Na+, K+ and Cs+, elicited by voltage-steps from -90mV to +80 mV in 5 mV increments (-110 mV holding potential).

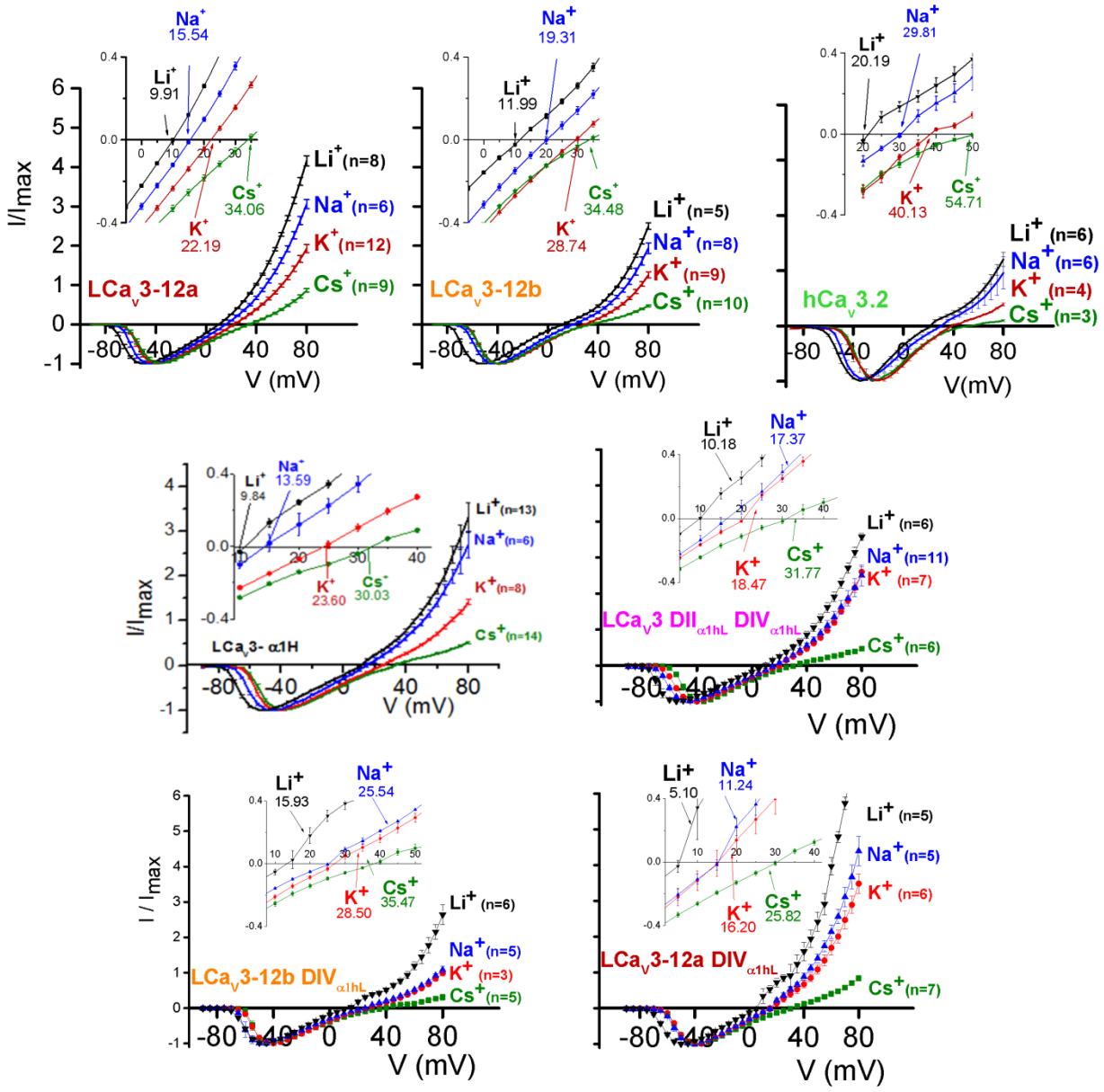

Figure 4.6 Current-Voltage (I-V) Relationships in Bi-ionic Conditions to Determine Reversal Potentials of Wild-Type T-type Channels and chimeric T-type Channels

Insets display a close-up of the X-axis where the I-V curves cross, representing the reversal potential. The reversal potential values are included for each ion. N values are included in parentheses.

Table 4.1Relative Permeability Values Calculated from Bi-Ionic Reversal Potentials

WILD TYPE CHANNELS

Relative Permeability:	P_{Ca}/P_{Li}	s.e.m.	n	P_{Ca}/P_{Na}	s.e.m.	n	P_{Ca}/P_{K}	s.e.m.	n	P_{Ca}/P_{Cs}	s.e.m.	n
Cav3.1	45.28	2.11	6	89.56	8.21	6	140.2	12.02	5	154.7	7.99	5
Cav3.2	44.8	3.79	6	84.3	5.32	6	172.5	9.12	4	180.8	21.06	3
Cav3.3	32.24	0.66	6	55.49	2.22	7	151	6.9	7	166.4	9.64	7
LCav3-12b	25.89	0.59	5	41.32	0.75	6	78.04	2.81	9	113.8	6.97	10
LCav3-12a	22.74	0.41	8	32.01	0.71	6	50.25	1.56	12	114.5	8.85	9

EFFECT OF HUMAN TURRETS (II AND IV) IN SNAIL BACKGROUND

Relative Permeability:	P_{Ca}/P_{Li}	s.e.m.	n	P_{Ca}/P_{Na}	s.e.m.	n	P_{Ca}/P_{K}	s.e.m.	n	P_{Ca}/P_{Cs}	s.e.m.	n
Cav3.2	44.8	3.79	6	84.3	5.32	6	172.5	9.12	4	180.8	21.06	3
LCav3- $DII_{\alpha i1hL}$ $DIV_{\alpha i1hL}$	34.3	0.75	4	70.19	3.66	4	41.7	1.37	4	117	10.39	3
LCav3- $DII_{\alpha i1hL}$	22.77	0.78	13	28.99	1.82	6	55.66	2.88	8	89.71	8.09	14

EFFECT OF 12A TURRET IN α1HL OR LCAV3 BACKGROUND

Relative Permeability:	P_{Ca}/P_{Li}	s.e.m.	n	P_{Ca}/P_{Na}	s.e.m.	n	P_{Ca}/P_{K}	s.e.m.	n	P_{Ca}/P_{Cs}	s.e.m.	n
Cav3.2	44.8	3.79	6	84.3	5.32	6	172.5	9.12	4	180.8	21.06	3
LCav3- 12a $DIV_{\alpha i1hL}$	32.66	2.95	5	41.98	2.38	5	42.97	4.119	6	114.8	8.265	7
LCav3- 12a	22.74	0.41	8	32.01	1.82	6	50.25	1.56	12	114.5	8.85	9
LCav3-12a ΔCys	13.47	0.42	7	16.87	0.77	6	18.85	0.66	9	38.6	2.15	13

EFFECT OF 12B TURRET IN α1HL OR LCAV3 BACKGROUND

Relative Permeability:	P_{Ca}/P_{Li}	s.e.m.	n	P_{Ca}/P_{Na}	s.e.m.	n	P_{Ca}/P_{K}	s.e.m.	n	P_{Ca}/P_{Cs}	s.e.m.	n
Cav3.2	44.8	3.79	6	84.3	5.32	6	172.5	9.12	4	180.8	21.06	3
LCav3- 12b $DIV_{\alpha i1hL}$	34.7	4.83	6	63.58	9.98	3	78.02	7.52	6	129.2	4.46	3
LCav3- 12b	25.89	0.59	5	41.32	0.75	6	78.04	2.81	9	113.8	6.97	10
LCav3-12b ΔCys	15.4	0.51	12	23.41	0.92	11	26.21	0.71	15	33.78	1.06	12

Table 4.2 One-Way Analysis of Variance (ANOVA) Results for Comparisons of Relative Permeability Values

	12a ΔCys	LCav3-12a					LCav3-12b				Cav3.1		Cav3.2
	12b ΔCys	12b	12a ΔCys	3.1	3.2	3.3	12b ΔCys	3.1	3.2	3.3	3.2	3.3	3.3
Li^+	**	**	**	**	**	**	**	**	**	**	n.s.	**	**
Na^+	**	**	**	**	**	**	**	**	**	*	n.s.	**	**
K^+	**	**	**	**	**	**	**	**	**	**	**	n.s.	**
Cs^+	n.s	n.s.	**	*	*	**	**	*	**	**	**	n.s.	**

	LCav3-$DII_{\alpha 1hL}$						
	12a	12b	12a ΔCys	12b ΔCys	3.1	3.2	3.3
Li^+	n.s.	*	**	**	**	**	**
Na^+	n.s.	**	**	**	**	**	**
K^+	n.s.	**	**	**	**	**	**
Cs^+	n.s.	*	**	**	**	**	**

	LCav3-12a $DIV_{\alpha 1hL}$									
	12a	12b	12a ΔCys	12b ΔCys	3.1	3.2	3.3	12b $DIV_{\alpha 1hL}$	$DII_{\alpha 1hL}$ $DIV_{\alpha 1hL}$	$DII_{\alpha 1hL}$
Li^+	**	n.s.	**	**	**	*	n.s.	n.s.	n.s.	**
Na^+	**	n.s.	**	**	**	**	**	*	**	**
K^+	n.s.	**	**	**	**	**	**	**	n.s.	*
Cs^+	n.s.	n.s.	**	**	**	**	**	n.s.	n.s.	n.s.

	LCav3-12b $DIV_{\alpha 1hL}$									
	12a	12b	12a ΔCys	12b ΔCys	3.1	3.2	3.3	12a $DIV_{\alpha 1hL}$	$DII_{\alpha 1hL}$ $DIV_{\alpha 1hL}$	$DII_{\alpha 1hL}$
Li^+	*	n.s.	**	**	n.s.	n.s.	n.s.	*	*	**
Na^+	**	*	**	**	n.s.	n.s.	n.s.	**	*	**
K^+	**	n.s.	**	**	**	**	**	**	**	**
Cs^+	n.s.	n.s.	**	**	n.s.	n.s.	*	**	n.s.	*

	LCav3-$DII_{\alpha 1hL}$ $DIV_{\alpha 1hL}$									
	12a	12b	12a ΔCys	12b ΔCys	3.1	3.2	3.3	12a $DIV_{\alpha 1hL}$	12b $DIV_{\alpha 1hL}$	$DII_{\alpha 1hL}$
Li^+	**	**	**	**	**	n.s.	n.s.	n.s.	n.s.	**
Na^+	**	**	**	**	n.s.	n.s.	**	**	n.s.	**
K^+	**	**	**	**	**	**	**	n.s.	**	**
Cs^+	n.s.	n.s.	**	**	*	n.s.	*	n.s.	n.s.	n.s.

iii $[Ca^{2+}]_{ex}$ Dependent Dose-Response with 60 mM $[Na^{+}]_{ex}$

For each of the channels of interest, a curve for the $[Ca^{2+}]_{ext}$ dependent dose-response in the presence of 60 mM $[Na^{+}]_{ext}$ is presented (Figure 4.7). It is similar to the anomalous mole fraction effect (AMFE) experiment, where anomalous behavior is traditionally observed as a decrease in current size as a result of competition between ions for positions within the channel pore. Our experiment is different from a traditional AMFE, however, because we increased the external concentration of calcium ions without decreasing the mole fraction of external sodium ions to compensate. This strategy allows us to observe the effect of differing $[Ca^{2+}]_{ext}$ in the presence of a constant $[Na^{+}]_{ext}$.

In the classical AMFE experiments by Almers and McCleskey and Tsien et al., they observed a U-shaped dependence, where the normalized current through frog skeletal muscle membrane (presumably, L-type calcium channels) would decrease to near-zero before steadily increasing to ever-higher current levels (Almers and McCleskey, 1984; Tsien et al., 1987). Upon the addition of external Ca^{2+} in the presence of external Na^{+}, the Na^{+} current would be blocked and eventually reach a zero-current level. Then, as $[Ca^{2+}]$ was increased further, the current levels would steadily increase as the Ca^{2+} influx became measurable. The dose-response curve represents the ability of Ca^{2+} to block Na^{+} influx through the channel, and is assumed to provide insight to the channel's relative affinity for Ca^{2+} (according to the "sticky pore" hypothesis).

The dose-response curves from log $[Ca^{2+}]$ of -9 to -2 (i.e., 10^{-9} M to 10^{-2} M $[Ca^{2+}]$) generated from the data collected from our wild-type, mutant and chimera T-type channels are shown in Figure 4.7A. A summary of the statistical analysis for these values can be found in Table 4.3. From data illustrated in Figure 4.7, it is apparent that the LCa_V3 DII-12a channels (i.e.,

LCa_v3-12a, LCa_v3-12a $DIV_{\alpha 1hL}$, and LCa_v3- 12a ΔCys) have the weakest Ca^{2+} block of the Na^+ current, displaying a monotonic decline as $[Ca^{2+}]$ increases. The data shown in Figure 4.7 suggests that the channels with the exon 12a turret always possess a weakened calcium block of the sodium current, regardless of the character of the DIV turret or cysteine configuration of the turrets. LCa_v3 channels with exon 12b, on the other hand, all consistently display a stronger calcium-dependent block of the sodium current compared to all exon 12a turret-containing channels. LCa_v3 DII-12b channels (i.e., LCa_v3-12b, LCa_v3- 12b $DIV_{\alpha 1hL}$, and LCa_v3-12b ΔCys) display the strongest Ca^{2+} dependent Na^+ block of all of the LCa_v3 variants investigated. LCa_v3 DII- α1hL channels (LCa_v3-$DII_{\alpha 1hL}$ and LCav3-$DII_{\alpha 1hL}$ $DIV_{\alpha 1hL}$) possess a block that is in-between, with a stronger block than LCav3 DII-12a channels, but a slightly weaker block than either LCa_v3 DII-12b channels or human Ca_v3 channels. For the most part, all of the LCa_v3 channels have a weaker block than the human Ca_v3 channels, which possess a typical U-shaped dependence. As mentioned previously, this U-shaped curve suggests a progessive Ca^{2+} block of the sodium current ($[Ca^{2+}] = 10^{-9} \rightarrow 10^{-7}$ M) at low calcium concentrations (i.e. the steep downward slope of the U shape), followed by an almost complete block of the Na^+ current ($[Ca^{2+}] = 10^{-5}$ M) (i.e. the trough of the U shape) followed by a steady increase in the current levels as Ca^{2+} begins to permeate the pore ($[Ca^{2+}] = 10^{-4} \rightarrow 10^{-2}$ M) (i.e. the steep upward slope of the U shape). Figure 4.7B highlights the region from $[Ca^{2+}]$ of 10^{-4} M to 10^{-2} M, displaying the steady increase in Ca^{2+} current in human Ca_v3 channels. In this region of $[Ca^{2+}]$, only LCa_v3-12b $DIV_{\alpha 1hL}$ illustrates an increase in the normalized current (presumably carried by Ca^{2+} at this point). All of the other LCa_v3 channel variants display a slight decrease in normalized current size (I/I_{max}), reflecting a relativey low Ca^{2+} influx when calcium concentrations rise through the

physiological (mM) range of external calcium concentrations. The percent change in normalized currents (I/I_{max}) from [Ca^{2+}] = 10 μM to 10 mM for each channel are displayed in Figure 4.8C.

The Ca^{2+} dependent block of the Na^+ current in the $10^{-4} \rightarrow 10^{-5}$ M (i.e., 10μM to 100 μM) range is considered particularly important because it is within this range that the human Ca_v3 channels have a nearly ~100% block of the Na^+ current (average %block at 10μM - $Ca_v3.1$: 96%, $Ca_v3.2$: 95%, $Ca_v3.3$: 98%). Theregion of 10 μM to 100 μM $[Ca^{2+}]_{ext}$ is highlighted in Figure 4.7C. The Ca^{2+} block of Na^+ current values (% block) with 100 μM [Ca^{2+}] for all channels are displayed in Figure 4.8A. Comparisons of the channels in terms of statistical significance (one-way ANOVA, P<0.05*, P<0.01**) are summarized in Table 4.3. The channels, in order of strongest block to weakest block in the 100 μM range, are as follows: $Ca_v3.2$ > $Ca_v3.3$ > $Ca_v3.1$ > LCa_v3-12b > LCa_v3-12b $DIV_{\alpha 1hL}$ > LCa_v3- 12b ΔCys > LCa_v3- $DII_{\alpha 1hL}$ > LCa_v3-$DII_{\alpha 1hL}$ $DIV_{\alpha 1hL}$ > LCa_v3-12a $DIV_{\alpha 1hL}$ > LCa_v3-12a > LCa_v3-12a ΔCys.

Ca^{2+} block of Na^+ current values (% block) with 10 μM [Ca2+] for all channels are displayed in Figure 4.8B. The 10 μM [Ca^{2+}] range is perhaps the most important because the dissociation constant (K_{D1}) of the Na^+ blocking effect of Ca^{2+} for Ca_v3 channels is between 7-10 μM (Shcheglovitov and Shuba, 2006). Comparisons of the channels in terms of statistical significance (one-way ANOVA, P<0.05*, P<0.01**) are summarized in Table 4.3. The channels, in order of strongest block to weakest block in the 10 μM range, are as follows: $Ca_v3.3$ > $Ca_v3.1$ > $Ca_v3.2$ > LCa_v3-12b $DIV_{\alpha 1hL}$ > LCa_v3-12b > LCa_v3- 12b ΔCys > LCa_v3- $DII_{\alpha 1hL}$ $DIV_{\alpha 1hL}$ > LCa_v3-$DII_{\alpha 1hL}$ > LCa_v3-12a $DIV_{\alpha 1hL}$ > LCa_v3-12a > LCa_v3-12a ΔCys.

Note that in terms of calcium-selectivity, the 10 μM Ca^{2+}-block series follows the same order as the fold-increase series determined from the inward sodium permeability experiments. The 10 μM block of the Na^+ current in LCa_v3-12b $DIV_{\alpha 1hL}$ (91% ± 2%) is not statistically

different from $Ca_v3.2$ or LCa_v3- $DII_{\alpha 1hL}$ $DIV_{\alpha 1hL}$, but is significantly greater than LCa_v3-12b ($P<0.01$) and LCa_v3-12b ΔCys ($P<0.05$). LCa_v3-12a $DIV_{\alpha 1hL}$ (49% ± 4%) is not significantly diffferent from LCa_v3-12a, but has a significantly ($P<0.01$) greater block compared to LCa_v3-12a ΔCys. LCa_v3- $DII_{\alpha 1hL}$ $DIV_{\alpha 1hL}$ (74% ± 9%) has a significantly stronger block compared to the LCa_v3-12a ($P<0.01$), LCa_v3-12a ΔCys ($P<0.01$), and LCa_v3-12a $DIV_{\alpha 1hL}$ ($P<0.05$), but is not statistically different compared to the other channels.

Overall, the trends of the Ca^{2+} dependent block of Na^+ currents in $DIV_{\alpha 1hL}$ LCa_v3 chimeras presented here are in agreement with the inward sodium permeability results (Figure 4.4). This data provides further support for the observations that the Domain II turret sequence has a dominant effect in determining ion selectivity in T-type channels, and that the character of the Domain IV turret has a weaker, but consistent and significant, effect on ion selectivity.

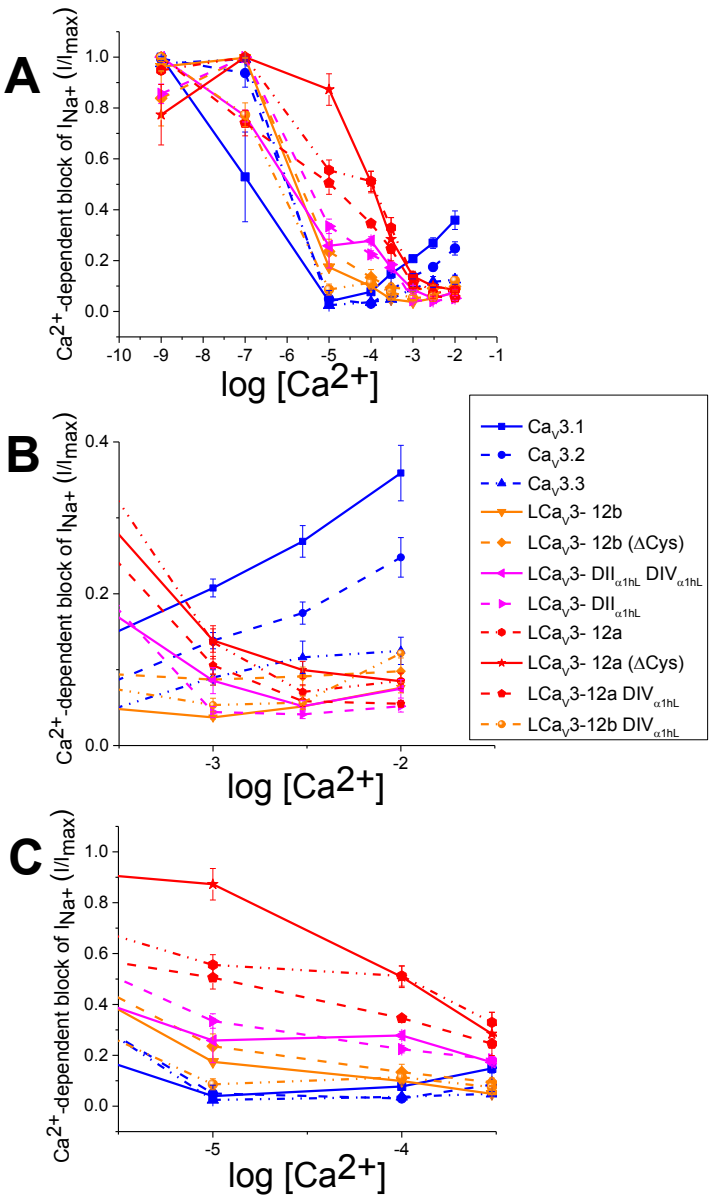

Figure 4.7 The Block of Na+ Current as the External Ca2+ Concentration Increases

Wild-type LCa_v3 and human Ca_v3 channels, LCa_v3 ΔCys mutant channels, and LCa_v3-$DIV_{\alpha 1hL}$ chimera channels are included and colour-coded according to their DII turret sequences. (A) 60 mM of external Na^+ is combined with varying calcium ranging from 10^{-9} to 10^{-2} M, depicting the block of current as calcium concentrations increase. (B) 60 mM of external sodium is combined with varying calcium concentrations ranging from 10^{-3} to 10^{-2} M (C) 60 mM of external sodium is combined with varying calcium concentrations ranging from 10^{-4} to $10^{-3.52}$ M.

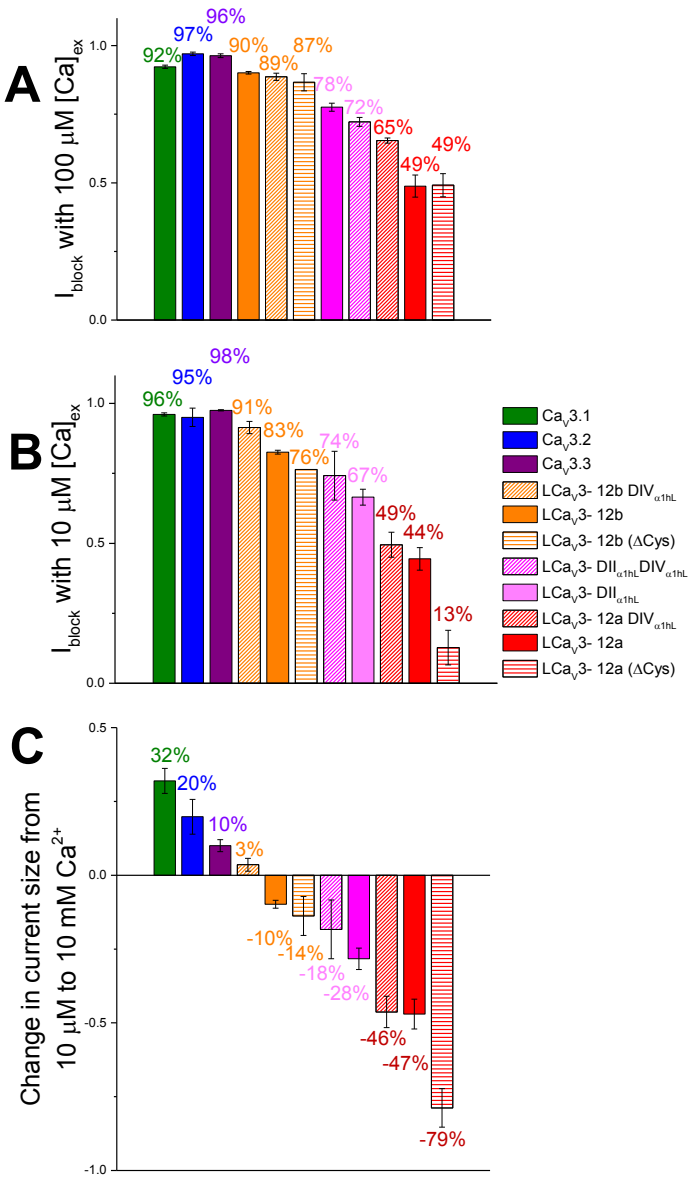

Figure 4.8 Bar Graphs Depicting Sodium Current Block by Calcium

(A)The percent of the sodium current (I/I_{max}) blocked by 100 µM external calcium. (B) shows the percent of sodium current (I/I_{max}) blocked by 10 µM calcium. A and B illustrate the effects that the Domain II and Domain IV turrets have on the Ca^{2+} block of the Na^{+} current. (C) Change in current size when the Ca^{2+} concentration increases from 10 µM to 10 mM; in this range, a current carried by Ca^{2+} is beginning to emerge in the human Cav3 and LCav3-12b $DIV_{\alpha 1hL}$ channels.

Table 4.3 One-Way Analysis of Variance (ANOVA) for Comparisons between Wild-Type, Delta-Cysteine, and Chimera T-types in Percentage of Na^+ Current Blocked by Ca^{2+}

$\log [Ca^{2+}]_{ext}$	**LCa_V3- 12b $DIV_{\alpha 1hL}$**							
	$Ca_V3.2$	LCa_V3-12b	LCa_V3-12a	LCa_V3-12b ΔCys	LCa_V3-12a ΔCys	LCa_V3- 12a $DIV_{\alpha 1hL}$	LCa_V3-$DII_{\alpha 1hL}$	LCa_V3- $DII_{\alpha 1hL}$ $DIV_{\alpha 1hL}$
-9	n.s.	n.s.	*	n.s.	*	n.s.	**	n.s.
-7	*	**	**	*	**	n.s.	**	n.s.
-5	n.s.	**	**	*	**	**	**	n.s.
-4	**	n.s.	**	n.s.	**	**	**	**
-3.52	n.s.	*	**	n.s.	*	**	**	**
-3	**	n.s.	**	*	**	**	n.s.	n.s.
-2.25	**	n.s.	n.s.	n.s.	*	n.s.	n.s.	n.s.
-2	**	**	*	n.s.	**	**	**	**

$\log [Ca^{2+}]_{ext}$	**LCa_V3- 12a $DIV_{\alpha 1hL}$**							
	$Ca_V3.2$	LCa_V3-12b	LCa_V3-12a	LCa_V3-12b ΔCys	LCa_V3-12a ΔCys	LCa_V3- 12b $DIV_{\alpha 1hL}$	LCa_V3-$DII_{\alpha 1hL}$	LCa_V3- $DII_{\alpha 1hL}$ $DIV_{\alpha 1hL}$
-9	n.s.	n.s.	*	n.s.	*	n.s.	**	n.s.
-7	*	**	**	**	**	n.s.	**	n.s.
-5	**	**	n.s.	**	**	**	*	*
-4	**	**	**	**	**	**	**	**
-3.52	**	**	n.s.	**	n.s.	**	*	**
-3	n.s.	**	n.s.	n.s.	n.s.	**	**	n.s.
-2.25	**	n.s.	n.s.	n.s.	**	n.s.	n.s.	n.s.
-2	**	*	*	*	**	**	n.s.	n.s.

$\log [Ca^{2+}]_{ext}$	**LCa_V3- $DII_{\alpha 1hL}$ $DIV_{\alpha 1hL}$**							
	$Ca_V3.2$	LCa_V3-12b	LCa_V3-12a	LCa_V3-12b ΔCys	LCa_V3-12a ΔCys	LCa_V3- 12b $DIV_{\alpha 1hL}$	LCa_V3- 12a $DIV_{\alpha 1hL}$	LCa_V3-$DII_{\alpha 1hL}$
-9	n.s.	n.s.	*	n.s.	*	n.s.	n.s.	**
-7	*	**	**	**	**	n.s.	n.s.	**
-5	n.s.	n.s.	**	n.s.	**	n.s.	*	n.s.
-4	**	**	**	**	**	**	**	*
-3.52	n.s.	**	**	**	n.s.	**	**	n.s.
-3	n.s.	*	n.s.	n.s.	n.s.	n.s.	n.s.	n.s.
-2.25	**	n.s.	n.s.	*	**	n.s.	n.s.	n.s.
-2	**	n.s.	n.s.	n.s.	n.s.	**	n.s.	n.s.

IV Overall Trends in the Ion Selectivity Experiments: Consistent Results for Calcium Selectivity in the Channels being Investigated

To improve clarity in illustrating the influences that the Domain II L5 and Domain IV L6 turrets have on ion selectivity in LCa_v3, the results of the ion selectivity experiments have been organized and compiled into Figures 4.9 to 4.13. Each figure has important results included from each of the experiments for determining inward sodium permeability ($Ca^{2+}/NMDG^{+}$ versus Ca^{2+}/Na^{+}), relative permeabily values based on bi-ionic reversal potentials, and Ca^{2+} dependent block of Na^{+} currents within the channels. Figure 4.9 displays the results collected from the wild-type T-type channels, Figure 4.10 includes the wild-type LCa_v3 channels and the cysteine-substitution (ΔCys) mutants, Figure 4.11 highlights the results for the double-turret mutant LCa_v3-$DII_{\alpha 1hL}$ $DIV_{\alpha 1hL}$, Figure 4.12 highlights the results of the DII-12a channels, and Figure 3.13 highlights the results of the DII-12b channels. Upon examination of these figures, the trends in terms of sodium permeability are readily apparent.

In Figure 4.9, the trends in ion selectivity first observed by Adriano Senatore and Wendy Guan are reiterated, where the high-calcium selectivity of human calcium channels is shown in comparison to the more sodium permeant LCa_v3 snail calcium channels.

Figure 4.10 displays the results of the ion selectivity experiments gathered and analyzed by Wendy Guan for the Domain II cysteine-substitution mutants, LCa_v3-12a ΔCys and LCa_v3-12b ΔCys. In this figure, it is apparent from the results of all of the ion selectivity experiments conducted that the ΔCys mutants have higher sodium permeability compared to their wild-type counterparts. However, the DII-12b channels are still more calcium-selective than the DII-12a channels, regardless of Domain II cysteine configuration.

The first $LCa_v3/Ca_v3.2$ chimera created was the $LCa_v3\text{-}DII_{\alpha 1hL}$ chimera, in which the Domain II L5 turret sequence of LCa_v3 was replaced by the corresponding sequence from $Ca_v3.2$. This channel resulted in a sodium permeability roughly mid-way between $Ca_v3.2$ and LCa_v3-12a. When Domain IV of $LCa_v3\text{-}DII_{\alpha 1hL}$ was replaced with the Domain IV L6 sequence from $Ca_v3.2$ to create $LCa_v3\text{-}DII_{\alpha 1hL}$ $DIV_{\alpha 1hL}$, the calcium-selectivity inreased.

The results of ion selectivity experiments with $LCa_v3\text{-}DII_{\alpha 1hL}$ and $LCav3\text{-}DII_{\alpha 1hL}$ $DIV_{\alpha 1hL}$ are highlighted in Figure 4.11. The relative permeability values calculated from the reversal potentials in bi-ionic conditions with Li^+ and Na^+ are consistent with the results of the inward sodium permeability experiment, suggesting a rank order of sodium permeability of: LCa_v3-12a > $LCa_v3\text{-}DII_{\alpha 1hL}$ > $LCa_v3\text{-}DII_{\alpha 1hL}$ $DIV_{\alpha 1hL}$ > $Ca_v3.2$. The Ca^{2+} dependent block of the Na^+ current in the channels illustrates the same aforementioned rank-order. However, perhaps due to low sample sizes, the $LCa_v3\text{-}DII_{\alpha 1hL}$ $DIV_{\alpha 1hL}$ values for the sodium block at 10 μM [Ca^{2+}] (Figure 4.11E) and current increase from 10 μM to 10 mM (Figure 4.11F) are not significantly different from either $LCa_v3\text{-}DII_{\alpha 1hL}$ or $Ca_v3.2$. Nonetheless, the results included in Figure 4.11 suggest that the addition of $DII_{\alpha 1hL}$ to the LCa_v3 channel increases calcium-selectivity over LCa_v3-12a, and addition of both $DII_{\alpha 1hL}$ and $DIV_{\alpha 1hL}$ increase calcium selectivity even further, allowing $LCa_v3\text{-}DII_{\alpha 1hL}$ $DIV_{\alpha 1hL}$ to approach the calcium-selectivity of $Ca_v3.2$.

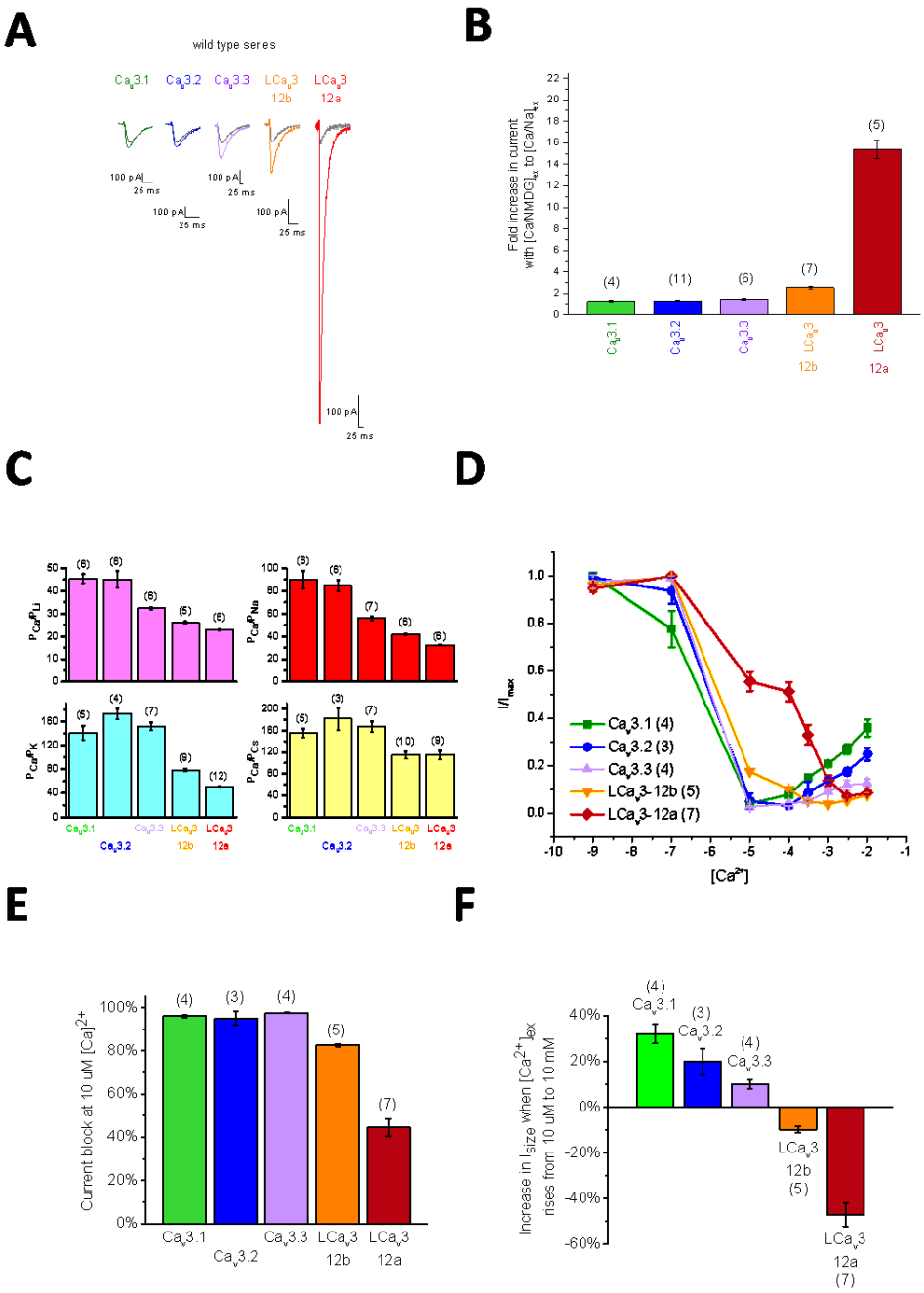

Figure 4.9 Ion Selectivity in Wild-Type Channels of Snails and Humans

(A) 2 mM Ca^{2+}/ 135 mM $NMDG^{+}$ (grey) is replaced by 2 mM Ca^{2+}/ 135 mM Na^{+} (colours).(B) Inward sodium permeability. (C) Relative Permeabilities calculated from bi-ionic reversal potentials. (D) 60 mM $[Na^{+}]_{ext}$ with $[Ca2+]_{ext}$ from 10^{-9} to 10^{-2} M (E) I_{block} at 10 µM calcium.(F) Change in $I/_{Imax}$ as $[Ca^{2+}]$ increases from 10 µM to 10 mM.

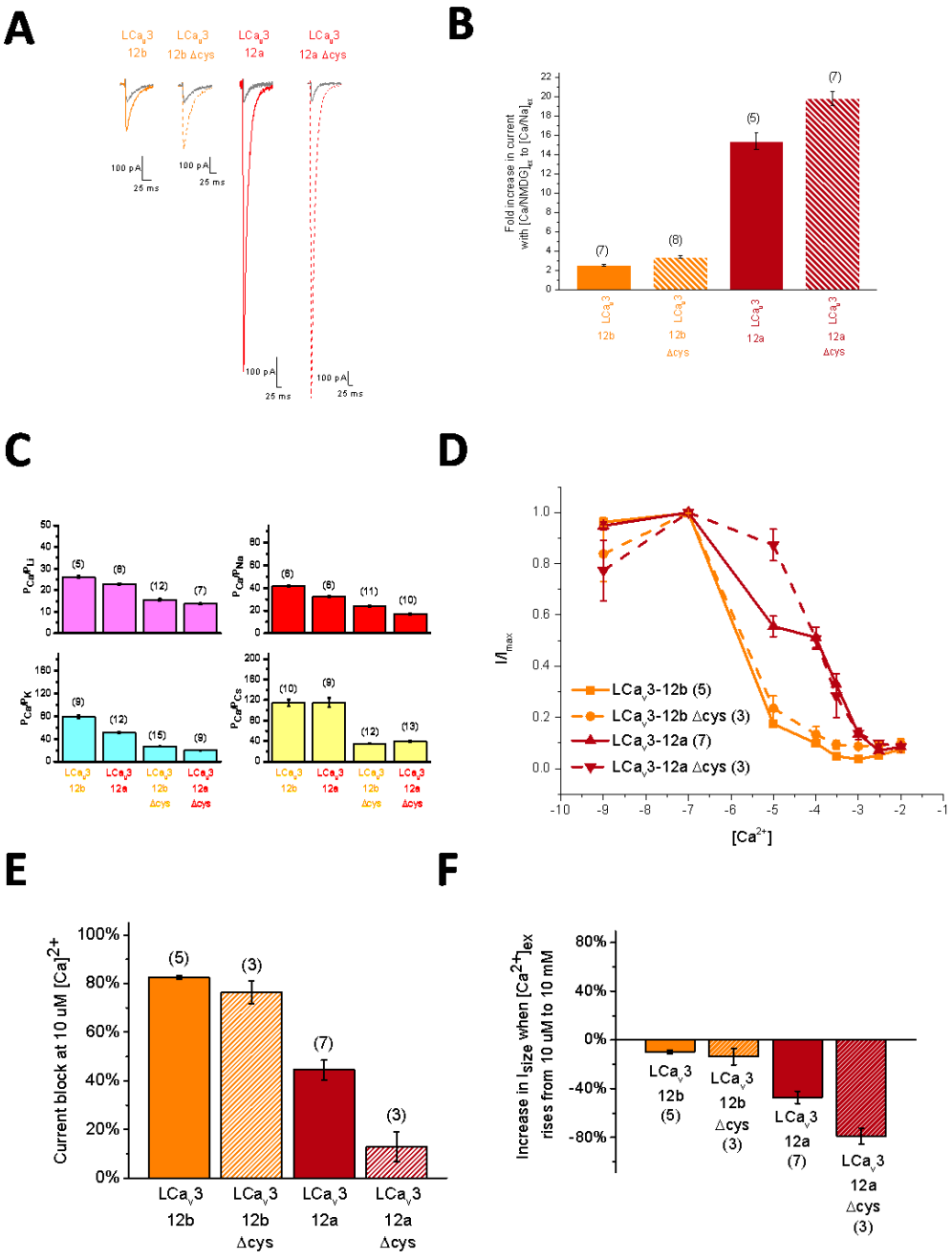

Figure 4.10 Effect of Domain II Delta-Cysteine Mutations in LCa_v3 Channels

(A) 2 mM Ca^{2+}/ 135 mM $NMDG^{+}$ (grey) is replaced by 2 mM Ca^{2+}/ 135 mM Na^{+} (colours).(B) Inward sodium permeability. (C) Relative Permeabilities calculated from bi-ionic reversal potentials. (D) 60 mM $[Na^{+}]_{ext}$ with $[Ca2+]_{ext}$ from 10^{-9} to 10^{-2} M (E) I_{block} at 10 µM calcium.(F) Change in $I/_{Imax}$ as $[Ca^{2+}]$ increases from 10 µM to 10 mM.

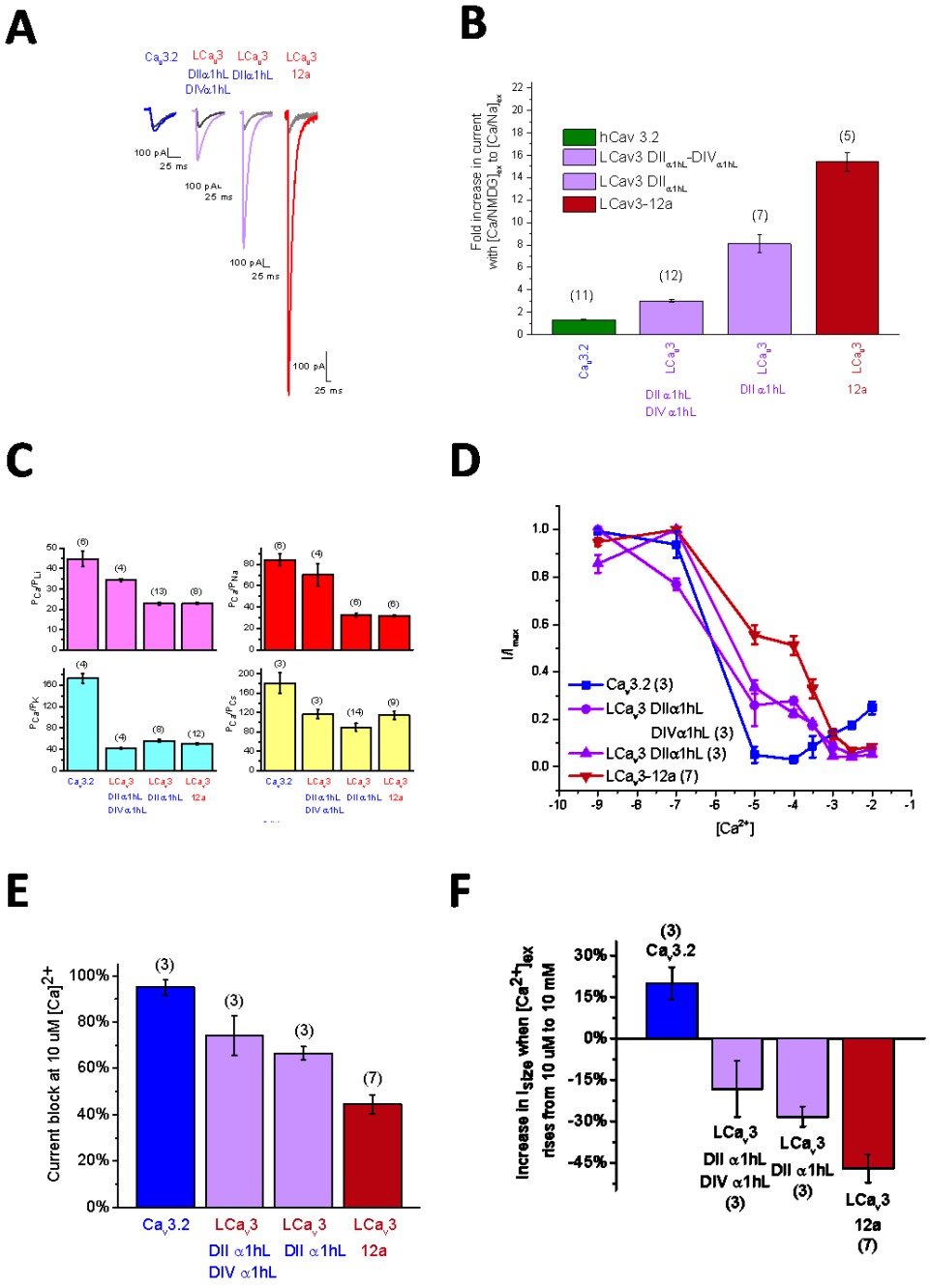

Figure 4.11 Effect of DII-α1hL in LCa$_v$3 Channels

(A) 2 mM Ca^{2+}/ 135 mM $NMDG^{+}$ (grey) is replaced by 2 mM Ca^{2+}/ 135 mM Na^{+} (colours).(B) Inward sodium permeability. (C) Relative Permeabilities calculated from bi-ionic reversal potentials. (D) 60 mM $[Na^{+}]_{ext}$ with $[Ca2+]_{ext}$ from 10^{-9} to 10^{-2} M (E) I_{block} at 10 µM calcium.(F) Change in $I/_{Imax}$ as $[Ca^{2+}]$ increases from 10 µM to 10 mM.

Figure 4.12 and 4.13 summarize the ion selectivity experiments for chimeras with exon 12a containing channels or exon 12b containing channels, respectively. The results of inward sodium permeability experiments with two additional mutants, $Ca_v3.2$-12b and $Ca_v3.2$-12a, are also included. Preliminary data resulting from analyses of $Ca_v3.2$-12a and $Ca_v3.2$-12b chimeras were included to provide further support for the idea that the Domain II sequence has a dominant effect on ion selectivity, regardless of the channel background being snail LCa_v3 or human $Ca_v3.2$ channels. More replicates need to be completed for statistical confidence in the ion selectivity behavior of $Ca_v3.2$-12a and $Ca_v3.2$-12b chimeras.

In Figure 4.12, the LCa_v3 channels and $Ca_v3.2$ with exon 12a in Domain II are presented, and these channels are compared to the wild-type $Ca_v3.2$. The wild-type LCa_v3-12a channel has the greatest measured sodium permeability. This is indicated by the results of every ion selectvity experiment performed here. The addition of the LCa_v3 Domain II L5 turret sequence to the $Ca_v3.2$ channel creates $Ca_v3.2$-12a, and the sodium permeability of this channel increased. Only one replicate has been completed so this result must be considered with this limitation in mind. But it does provide incentive for looking more closely at the Domain II turret sequence as a critical determinant of ion selectivity in human Ca_v3 channels.

The Domain IV sequence is also important in determining ion selectivity. The LCa_v3-12a $DIV_{\alpha 1hL}$ channel has a higher degree of calcium selectivity, which is evidenced by the results of the inward sodium permeaiblity experiments, bi-ionic reversal potential experiments, and the Ca^{2+} dependent block of the Na^+ current. The LCa_v3-12a $DIV_{\alpha 1hL}$ channel does not have significantly greater calcium selectivity in bi-ionic reversal potential experiments with K^+ or Cs^+, and the channel's Ca^{2+} block of the sodium current at 10 μM is not significantly greater than that of LCa_v3-12a. Nonetheless, there is a significant difference in channels containing

invertebrate $DIV_{\alpha 1hL}$ sequence albeit weaker than the influence of invertebrate Domain II channels containig exon 12a.

In Figure 4.13, the results of the ion selectivity experiments in channels containing the Domain II 12b turret sequence are summarized. The $Ca^{2+}/NMDG^{+}$ versus Ca^{2+}/Na^{+} current traces illustratethat the presence of the LCa_v3-12b turret sequence in the human $Ca_v3.2$ channel can increase sodium permeability. In the $Ca_v3.2$ channel, the degree of sodium permeability is weaker to that of any of the channels containing Domain II 12a. Again, this is only a one-recording sample so this single data point must not be over-interpreted. The replacement of the LCa_v3 Domain IV L6 turret sequence with the sequence of $DIV_{\alpha 1hL}$ created higher calcium selectivitiy in these exon-12b-containing channels, just like in the LCa_v3-12a $DIV_{\alpha 1hL}$ channel. All of the results provided for the LCa_v3-12b $DIV_{\alpha 1hL}$ channel lead to the conclusion that the $DIV_{\alpha 1hL}$ sequence in LCa_v3 is associated with increased calcium selectivity. The relative permeability values determined for LCa_v3-12b $DIV_{\alpha 1hL}$ are not significantly different from LCa_v3-12b (except for the P_{Ca}/P_{Na}), but the relative permeability is also not significantly different from $Ca_v3.2$. The 10 μM Ca^{2+} block of the Na^{+} current is significantly greater in LCa_v3-12b $DIV_{\alpha 1hL}$ compared to LCa_v3-12b. The increase in current from 10 μM to 10 mM in LCa_v3-12b $DIV_{\alpha 1hL}$ is also significantly greater than that in LCa_v3-12b.

The results of the inward sodium permeability experiments, bi-ionic reversal potential experiments, and experiments to determine the Ca^{2+} dependent block of the Na^{+} current all to point to consistent trends in ion selectivity for the channels investigated. There are some discrepancies in the results of the bi-ionic reversal potential experiments, especially when the internal ion is K^{+} or Cs^{+}. However, these discrepancies hardly take away from the overall

trends apparent in the dataset. According to these results, the order of sodium permeability, from most sodium-permeable channels to least sodium-permeable is as follows:

- For wild type channels (Figure 4.12; Guan 2014; Senatore et al., 2014), snail channel isoforms are more sodium permeable than human T-type channels:
    - LCa_v3-12a > LCa_v3-12b > $Ca_v3.3$ > $Ca_v3.2$ > $Ca_v3.1$
- If the cysteine residues in the Domain II L5 turret turret in LCa_v3 are removed, the ΔCys channels allow for higher sodium permeability compared to the wild-types (Figure 4.10; Guan 2014):
    - LCa_v3-12a ΔCys > LCa_v3-12a
    - LCa_v3-12b ΔCys > LCa_v3-12b
- If the Domain IV turret from the calcium-selective $Ca_v3.2$ channel replaces the Domain IV turret from the relatively sodium-permeable LCa_v3 channel, then the LCa_v3 channel becomes more calcium selective (Figure 4.11, 4.12 and 4.13):
    - LCa_v3-12a > LCa_v3- 12a $DIV_{\alpha 1hL}$
    - LCa_v3-12b > LCa_v3- 12b $DIV_{\alpha 1hL}$
    - LCa_v3- $DII_{\alpha 1hL}$ > LCa_v3- $DII_{\alpha 1hL}$ $DIV_{\alpha 1hL}$
- All Domain II turret modifications are such that channels containing the exon 12a turret are always more sodium-selective than channels containing exon 12b turrets: LCa_v3-12a ΔCys > LCa_v3-12a > LCa_v3- 12a $DIV_{\alpha 1hL}$ > LCa_v3-12b ΔCys > LCa_v3-12b > LCa_v3-12b $DIV_{\alpha 1hL}$.

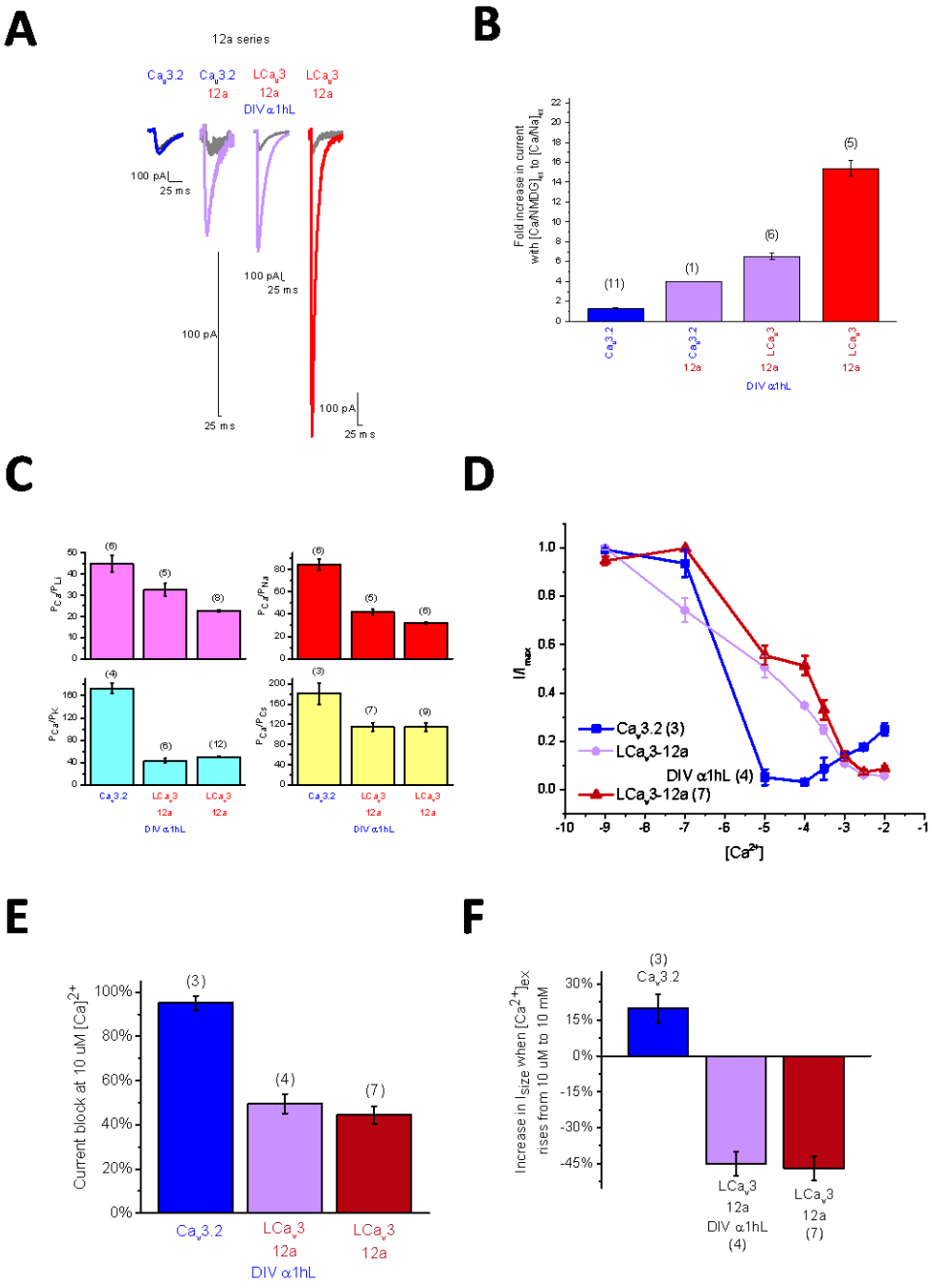

Figure 4.12 Dominant Effect of DII-12a in Cav3.2 and LCav3 Channels

(A) 2 mM Ca^{2+}/ 135 mM $NMDG^{+}$ (grey) is replaced by 2 mM Ca^{2+}/ 135 mM Na^{+} (colours).(B) Inward sodium permeability. (C) Relative Permeabilities calculated from bi-ionic reversal potentials. (D) 60 mM $[Na^{+}]_{ext}$ with $[Ca2+]_{ext}$ from 10^{-9} to 10^{-2} M (E) I_{block} at 10 µM calcium.(F) Change in $I/_{Imax}$ as $[Ca^{2+}]$ increases from 10 µM to 10 mM.

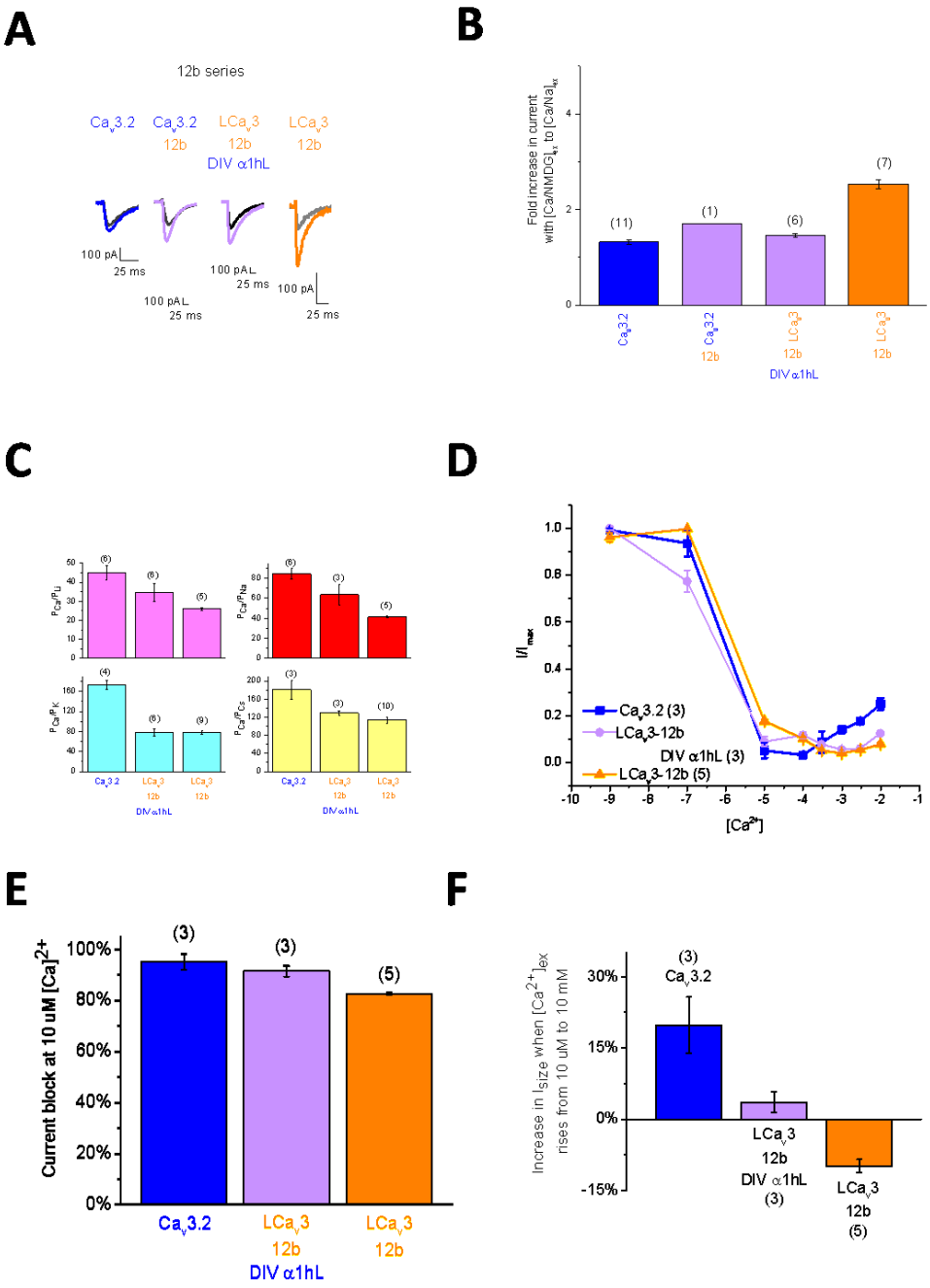

Figure 4.13 Dominant Effect of DII-12b in Cav3.2 and LCav3 Channels

(A) 2 mM Ca^{2+}/ 135 mM $NMDG^{+}$ (grey) is replaced by 2 mM Ca^{2+}/ 135 mM Na^{+} (colours).(B) Inward sodium permeability. (C) Relative Permeabilities calculated from bi-ionic reversal potentials. (D) 60 mM $[Na^{+}]_{ext}$ with $[Ca2+]_{ext}$ from 10^{-9} to 10^{-2} M (E) I_{block} at 10 µM calcium.(F) Change in $I/_{Imax}$ as $[Ca^{2+}]$ increases from 10 µM to 10 mM.

V Channel Kinetics

As a secondary outcome, the biophysical properties of the chimeric LCa_v3 T-type calcium channels were explored and compared to the wild-type LCa_v3 channels and to the human $Ca_v3.2$ channel. This is to ensure that the creation of the chimeric channels did not result in changes so drastic that the resultant channels were no longer reminiscent of the wild-type T-type channels. Our hypothesis includes that we do not expect the channel kinetics to be dramatically altered, because the chimeras did not involve alterations in the voltage-senor domain or gating brake.

The biophysical properties of the chimeric channels, LCa_v3-12b $DIV_{\alpha 1hL}$, LCa_v3-12a $DIV_{\alpha 1hL}$, and LCa_v3- $DII_{\alpha 1hL}$ $DIV_{\alpha 1hL}$, are shown in Figure 4.14. These channels are compared to their wild-type counterparts and to $Ca_v3.2$ using one-way ANOVA, and the results are displayed in Tables 4.4 and 4.5. The values of biophysical properties for LCav3-$DII_{\alpha 1hL}$, LCa_v3-12a, LCa_v3-12b and $Ca_v3.2$ are also found in Table 4.4, and LCav3-DIIα1hL is compared to the wild-type channels using one-way ANOVA in Table 4.5. The biophysical properties of LCa_v3- $DII_{\alpha 1hL}$ and the wild-type channels (LCa_v3-12a, LCa_v3-12b, and $Ca_v3.2$) are taken from Wendy Guan's MSc Thesis (Guan, 2014).

The current-voltage relationships for these channels with external 2mM Ca^{2+} and internal 110 mM Cs^{+} solutions (see Section 3.IV.i) are in Figure 4.14A. These I-V curves are very similar to the I-V relationships determined for LCa_v3-12b, LCa_v3-12a, LCa_v3- $DII_{\alpha 1hL}$ and $Ca_v3.2$ (Guan, 2014). The I-V curves for all three chimeric LCa_v3 channels are also similar to one another. The large outward currents (positive I/I_{max} in the I-V) are presumably carried by internal Cs^{+} ions, and thus are representative of greater monovalent ion permeability. According to the I-V curves in the external kinetics solution, LCa_v3-12a $DIV_{\alpha 1hL}$ has the largest outward currents, LCa_v3-

$DII_{\alpha 1hL}$ $DIV_{\alpha 1hL}$ is intermediate, and LCa_v3-12b $DIV_{\alpha 1hL}$ has the smallest outward current. This is in agreement with the inward sodium permeability resuts, relative permeability results, and Ca^{2+} dependent dose-response of the Na^+ current results (Figures 4.4 and 4.7). The peak of the I-V curves is near the expected value of -40 mV (the peak of the LCa_v3-12a and LCa_v3-12b IV curves), but LCa_v3-12a $DIV_{\alpha 1hL}$ and LCa_v3- $DII_{\alpha 1hL}$ $DIV_{\alpha 1hL}$ both experience a -5 mV shift in peak voltage (-45 mV). The peak of the LCa_v3-$DII_{\alpha 1hL}$ chimera is also at -45 mV. From the I-V data, an activation curve for each channel was also determined (g/g_{max} in Figure 4.14E). The activation curves for all three chimeric LCa_v3 channels are similar to one another. Descriptive values of the activation curves for the chimeras and wild-type channels are provided in Table 4.4. The average $V_{1/2}$ values and the average K slope values of the channels are shown. Although the three chimeric LCa_v3 channels are different than the wild-type LCa_v3 channels, the changes are only small (<5 mV). Notably, the LCa_v3-$DII_{\alpha 1hL}$ $DIV_{\alpha 1hL}$ activation curve is positively shifted by 5 mV compared to LCa_v3-$DII_{\alpha 1hL}$.

The steady-state inactivation curves for the channels are presented in Figure 4.14E (I/I_{max}). Like the activativation curves, these inactivatin curves were fitted to a Boltzmann equation and $V_{1/2}$ and K values were determined. LCa_v3-12a $DIV_{\alpha 1hL}$ inactivation kinetics are not significantly different compared to LCa_v3-12a. On the other hand, LCa_v3-12b $DIV_{\alpha 1hL}$ experiences a significant ($P<0.01$) positive shift in inactivation by ~5 mV compared to LCa_v3-12b. LCa_v3-$DII_{\alpha 1hL}$ $DIV_{\alpha 1hL}$ inactivation curve is significantly different compared to LCa_v3-$DII_{\alpha 1hL,}$ by only a small positive shift. The overlapping activation and inactivation curves, which is apparent for all channels in Figure 4.14E, indicates a characteristic T-type window current.

Other kinetics include the time-to-peak activation and time-constants of inactivation. Introduction of $DIV_{\alpha 1hL}$ resulted in slower time-to-peak activation kinetics in all channels. It

should be noted that $Ca_v3.2$ has slower time-to-peak than the LCa_v3-12a and LCa_v3-12b channels. For each of the channels, the time-constant of inactivation also increased (i.e., the channels become slower to inactivate). This change is only slight from LCa_v3-12b to LCa_v3-12b $DIV_{\alpha 1hL,}$ but the change is dramatic between LCa_v3-12a and LCa_v3-12a $DIV_{\alpha 1hL}$. In fact, the time-constant are almost two-fold in LCav3-12a $DIV_{\alpha 1hL}$ compared to LCa_v3-12a at -55 mV and -10 mV. A similar relationship is observed between the time-constants of inactivation for LCa_v3-$DII_{\alpha 1hL}$ and LCa_v3-$DII_{\alpha 1hL}$ $DIV_{\alpha 1hL,}$ with the LCa_v3-$DII_{\alpha 1hL}$ $DIV_{\alpha 1hL}$ time-constants being almost two-fold compared to LCa_v3-$DII_{\alpha 1hL.}$ The time-constants of inactivation for LCa_v3-$DII_{\alpha 1hL}$ - $DIV_{\alpha 1hL}$ are actually more similar to LCa_v3-12b than to LCa_v3-$DII_{\alpha 1hL.}$

Deactivation kinetics are measured as time-constants of the decay of tail-currents (Figure 4.14B). The tau deactivation values for LCa_v3-12b $DIV_{\alpha 1hL}$ and LCa_v3-$DII_{\alpha 1hL}$ $DIV_{\alpha 1hL}$ are not significantly different from the tau deactivation values from $Ca_v3.2$. LCa_v3-12a $DIV_{\alpha 1hL,}$ however, has tau deactivation values that are significantly different from all of the human and snail wild-type channels. The τ_{deac} values at -100 mV and -60 mV for LCa_v3-12a $DIV_{\alpha 1hL}$ are approximately two-fold greater than the τ_{deac} values of the wild-type channels, indicating that the LCa_v3-12a $DIV_{\alpha 1hL}$ chimera has slower deactivation.

The most striking differences occur for recovery from inactivation. For the chimeric LCa_v3 channels studied here (Figure 4.14D and Table 4.4), the $T_{0.5}$ values are between 475 and 685 ms. Compared to the wild-type channels, in which the fastest channel to recover is LCa_v3-12a at $T_{0.5}$ = 1859.74 ± 93.14, these chimeric channels recover from inactivation very quickly. The average LCa_v3-12b $DIV_{\alpha 1hL}$ recovery from inactivation is almost four times faster than the average LCa_v3-12b, and LCa_v3-12a $DIV_{\alpha 1hL}$ is almost three times faster than LCa_v3-12a. $Ca_v3.2$ recovers more rapidly than LCa_v3-12b, but takes more time to recover than LCa_v3-12a.

Interestingly, the $LCa_v3\text{-}DII_{\alpha 1hL}$ is also significantly faster to recover compared to any of LCa_v3-12a, LCa_v3-12b, or $Ca_v3.2$. However, compared to $LCa_v3\text{-}DII_{\alpha 1hL}$, $LCa_v3\text{-}DII_{\alpha 1hL}$ $DIV_{\alpha 1hL}$ is still more than three times faster when it comes to recovery from inactivation. $LCa_v3\text{-}DII_{\alpha 1hL}$ $DIV_{\alpha 1hL}$ displays the fastest recovery from inactivation compared to any of the channels studied.

Overall, the biophysical properties of the chimeric LCa_v3 channels studied here (i.e., LCa_v3-12a $DIV_{\alpha 1hL,}$ LCa_v3-12b $DIV_{\alpha 1hL,}$ and $LCa_v3\text{-}DII_{\alpha 1hL}$ $DIV_{\alpha 1hL}$) are reminiscent of the mammalian and invertebrate wild-type T-type channels. Although the inactivation, activation and deactivation kinetics are significantly different in the chimeras compared to the wild-type channels, the changes are not dramatic. The changes in recovery from inactivation are quite striking, but these differences should not affect our interpretations of the ion selectivity data. It is interesting, however, that replacment of DII and DIV turrets has rather dramatic affects on the rate of recovery in these channels. It should be noted that slightly different recovery from inactivation voltage-step protocols were used between the wild-type and chimeric channels; however, this cannot explain such drastic changes. Experimenter differences should also be considered.

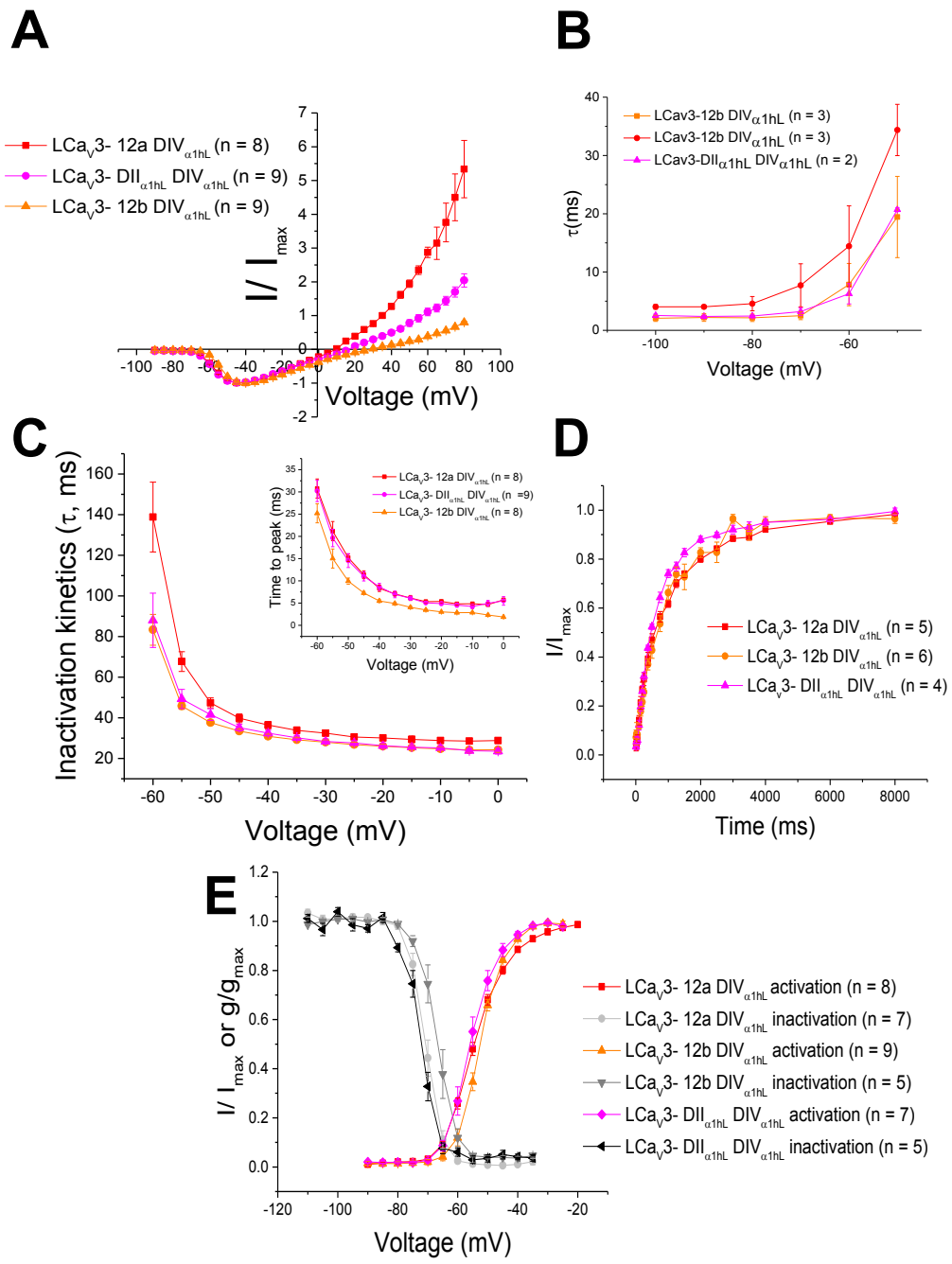

Figure 4.14 Biophysical kinetics of LCa$_v$3 Chimeras with Domain IV Turrets from Ca$_v$3.2

(A) Current-voltage relationship (I-V) (B) Tau deactivation (C) Voltage-dependence of tau inactivation (τ_{inact}) values (inset) Time to peak in milliseconds at voltage-steps from -60 mV to 0 (D) Recovery from inactivation is faster than in wild-type counterparts (E) Activation and steady state inactivation curves.

Table 4.4 Descriptive Values of Biophysical Kinetics for LCa_v3-12b $DIV_{\alpha 1hL}$, LCa_v3-12a $DIV_{\alpha 1hL}$, and LCa_v3-$DII_{\alpha 1hL}$ $DIV_{\alpha 1hL}$, LCa_v3- $DII_{\alpha 1hL}$, LCa_v3-12b, LCa_v3-12a, and $Ca_v3.2$

	LCav3- 12b $DIV_{\alpha 1hL}$	n	LCav3- 12a $DIV_{\alpha 1hL}$	n	LCav3- $DII_{\alpha 1hL}$ $DIV_{\alpha 1hL}$	n	LCav3-$DII_{\alpha 1hL}$	n	LCav3-12b WT	n	LCav3-12a WT	n	Cav3.2	n
Activation														
$V_{1/2}$	-52.44 ± 0.28	9	-54.14 ± 0.63	8	-55.63 ± 1.10	7	-61 ± 0.42	17	-53.48 ± 0.34	13	-53.63 ± 0.35	24	-48.58 ± 0.54	13
K	3.91 ± 0.35	9	5.32 ± 0.18	8	3.97 ± 0.18	7	3.10 ± 0.081	17	5.46 ± 0.14	13	5.60 ± 0.09	29	3.85 ± 0.14	13
Peak of IV	-40 mV	9	-45 mV	8	-45 mV	7	-45 mV	17	-40 mV	13	-40 mV	24	-30 mV	13
Inactivation														
$V_{1/2}$	-67.00 ± 1.22	5	-69.98 ± 0.86	7	-73.31 ± 0.77	5	-75.57 ± 0.71	9	-70.89 ± 0.49	16	-70.21 ± 0.38	20	-62.88 ± 2.25	5
K	2.66 ± 0.13	5	2.50 ± 0.07	7	2.52 ± 0.17	5	2.41 ± 0.051	9	2.93 ± 0.08	16	2.73 ± 0.04	20	4.78 ± 0.37	5
Activation kinetics														
TTP -55mV (ms)	15.01 ± 2.14	8	21.19 ± 2.16	8	19.63 ± 1.96	9	10.58 ± 0.32	17	12.62 ± 0.70	16	14.68 ± 0.63	24	27.61 ± 2.27	12
TTP -10mV (ms)	2.88 ± 0.17	8	4.85 ± 0.32	8	4.22 ± 0.48	9	2.34 ± 0.071	17	2.35 ± 0.12	16	3.19 ± 0.39	24	5.71 ± 0.37	12
Inactivation kinetics														
τ_{inact} -55mV (ms)	45.84 ± 1.69	8	67.71 ± 4.86	8	49.27 ± 4.69	9	26.72 ± 0.81	17	40.07 ± 2.56	16	38.40 ± 1.67	24	91.91 ± 7.27	12
τ_{inact} -10mV (ms)	24.70 ± 1.15	8	28.85 ± 1.35	8	25.22 ± 0.92	9	14.73 ± 0.30	17	15.67 ± 0.56	16	17.20 ± 048	24	19.49 ± 1.50	12
Deactivation														
τ -100 mV (ms)	2.07 ± 0.54	3	4.03 ± 0.40	3	2.55 ± 0.23	2	1.18 ± 0.059	13	1.37 ± 0.05	19	1.97 ± 0.06	12	2.45 ± 0.20	11
τ -60 mV (ms)	7.85 ± 3.62	3	14.43 ± 6.92	3	6.27 ± 1.74	2	13.27 ± 0.3	13	5.45 ± 0.52	19	6.05 ± 0.30	12	8.49 ± 0.68	11
Recovery from Inactivation														
% recovery at 0.25s	26.73 ± 1.43	7	30.99 ± 2.67	5	32.26 ± 1.52	4	7.96 ± 0.0056	12	5.33 ± 0.30	13	7.81 ± 0.37	13	8.72 ± 0.0054	10
% recovery at 5s	97.31 ± 1.23	7	93.77 ± 0.38	5	95.62 ± 1.04	4	69.05 ± 0.010	12	62.50 ± 1.00	13	65.71 ± 1.13	13	62.08 ± 0.013	10
$T_{0.5}$ (ms)	579.18 ± 29.57	6	632.30 ± 51.75	5	496.12 ± 21.94	4	1631.26 ± 46.94	12	2243.09 ± 82.26	13	1859.74 ± 93.14	13	2093.79 ± 95.69	10

Table 4.5 One-way Analysis of Variance (ANOVA) for Comparing Kinetic Values from LCa_v3-12b $DIV_{\alpha 1hL}$, LCa_v3-12a $DIV_{\alpha 1hL}$, and LCa_v3-$DII_{\alpha 1hL}$ $DIV_{\alpha 1hL}$, LCa_v3- $DII_{\alpha 1hL}$, LCa_v3-12b, LCa_v3-12a, and $Ca_v3.2$

	12b $DIV_{\alpha 1hL}$/ 12b WT	12a $DIV_{\alpha 1hL}$/ 12a WT	$DII_{\alpha 1hL}$ $DIV_{\alpha 1hL}$/ $DII_{\alpha 1hL}$ WT	12b $DIV_{\alpha 1hL}$/ Cav3.2	12a $DIV_{\alpha 1hL}$/ Cav3.2	$DII_{\alpha 1hL}$ $DIV_{\alpha 1hL}$/ Cav3.2	$DII_{\alpha 1hL}$ / 12b WT	$DII_{\alpha 1hL}$ / 12a WT	$DII_{\alpha 1hL}$ / Cav3.2
Activation									
$V_{1/2}$	**	**	**	**	**	**	**	**	**
K	**	**	**	n.s.	**	n.s.	**	**	**
Peak of IV									
Inactivation									
$V_{1/2}$	**	n.s.	**	**	**	**	**	**	**
K	**	**	n.s.	**	**	**	**	n.s.	**
TTP -55mV (ms)	**	**	**	**	**	**	**	**	**
TTP -10mV (ms)	**	**	**	**	**	**	**	**	**
τ_{inact} -55mV (ms)	**	**	**	**	**	**	*	*	**
τ_{inact} -10mV (ms)	**	**	**	**	**	**	n.s.	**	n.s.
Deactivation									
τ -100 mV (ms)	**	**	**	n.s.	**	n.s.	n.s.	**	**
τ -60 mV (ms)	**	**	**	n.s.	**	**	**	**	**
Recovery from Inactivation									
% recovery at 0.25s	**	**	**	**	**	**	**	n.s.	n.s.
% recovery at 5s	**	**	**	**	**	**	**	*	**
$T_{0.5}$ (ms)	**	**	**	**	**	**	**	*	**

5. Discussion

I Domain II and Domain IV Turrets Influence Ion Selectivity in LCa_v3

This thesis project has involved exploring the extracellular turret structures from Domain II and Domain IV in LCa_v3 T-type calcium channels to determine their influence on ion selectivity within the channels. First, Domain IV turret chimeras were created using molecular cloning techniques. Then, the results of ion selectivity experiments for these chimeras were compared to the results for wild-type LCa_v3-12a and LCa_v3-12b channels, as well as the human $Ca_v3.2$ channel. Furthermore, these chimeras were compared to Domain II cysteine-substitution mutants (LCa_v3-12a ΔCys and LCa_v3-12b ΔCys) and the $LCa_v3/Ca_v3.2$ Domain II chimera, LCa_v3-$DII_{\alpha 1hL}$. Our results indicate that replacing the Domain IV L6 turret from LCa_v3-12a, LCa_v3-12b, or LCa_v3-$DII_{\alpha 1hL}$ with the Domain IV L6 turret sequence from $Ca_v3.2$ resulted in changes in Ca^{2+} versus Na^+ selectivity. Cloning the $Ca_v3.2$ Domain IV L6 turret into an LCa_v3 channel made these channels more like $Ca_v3.2$ in terms of ion selectivity (i.e., they became more calcium selective).

The results of this thesis project have addressed three of the four hypotheses presented in section 2. First, the LCa_v3 chimeras with Domain IV replaced by the Domain IV turret from $Ca_v3.2$ have become more $Ca_v3.2$-like in terms of Ca^{2+} versus Na^+ selectivity. Results of the inward sodium permeability experiments (Figure 4.4) and Ca^{2+} dependent block of the Na^+ currents (Figures 4.7 and 4.8) in the chimeric channels indicates that replacing Domain IV L6 of LCa_v3 with Domain IV L6 from $Ca_v3.2$ have, indeed, created chimeric channels that are more $Ca_v3.2$-like in terms of calcium-selectivity. Most of the results of bi-ionic reversal potential

experiments to determine relative permeabilities (Table 4.1) also indicate higher calcium selectivity in the chimeras; LCa_v3-12b $DIV_{\alpha 1hL}$ has a higher P_{Ca}/P_{Na} value than LCa_v3-12b, LCa_v3-12a $DIV_{\alpha 1hL}$ has a higher $P_{Ca}/_{Na}$ than LCa_v3-12a, and LCa_v3-$DII_{\alpha 1hL}$ $DIV_{\alpha 1hL}$ has a higher P_{Ca}/P_{Na} value than LCa_v3-$DII_{\alpha 1hL}$.

The second part of the hypotheses that has been adequately addressed by the results of this thesis is whether or not the Domain II and Domain IV turrets are influencing ion selectivity independently of one another. Indeed, the LCa_v3 channel chimeras with Domain IV L6 from $Ca_v3.2$ have a significant influence on ion selectivity, regardless of the character of the Domain II turret. The presence of $DIV_{\alpha 1hL}$ has the same effect on LCa_v3-12a (Figure 4.12), LCa_v3-12b (Figure 4.13), and LCa_v3-$DII_{\alpha 1hL}$ (Figure 4.11); specifically, $DIV_{\alpha 1hL}$ in the L6 region of any of these channels causes increased calcium-selectivity. Furthermore, the results of this study suggest that the Domain II L5 turret sequence has a dominant effect on ion selectivity. Regardless of the cysteine configuration of the Domain II turret or the character of the Domain IV L6 sequence, LCa_v3-12a channels (LCa_v3-12a, LCa_v3-12a ΔCys and LCa_v3-12a $DIV_{\alpha 1hL}$) are always more sodium-permeable than the more calcium-selective LCa_v3-12b channels (LCa_v3-12b, LCa_v3-12b ΔCys and LCa_v3-12b $DIV_{\alpha 1hL}$). The dominant influence of the Domain II sequence is apparent from the results of the $Ca^{2+}/NMDG^{+}$ versus Ca^{2+}/Na^{+} experiments (Figure 4.4), the bi-ionic reversal potential experiments (Table 4.1), and with the Ca^{2+} dependent block of the Na^{+} current (Figure 4.7 and 4.8).

Finally, the results of this project show that the chimeras have experienced changes in their gating kinetics compared to their wild-type counterparts (Figure 4.14 and Table 4.4). Although, for the most part, the changes in gating kinetics were small in these chimeric channels, there are a few instances of large changes in biophysical properties. Compared to LCa_v3-12a, the

time-constant of inactivation (τ_{inact}) for LCa_v3-12a $DIV_{\alpha 1hL}$ changed quite dramatically. The time to recovery from inactivation was also decreased by 3 to 4 times for all of the Domain IV chimeric channels studied. These changes were not expected, but should not have a large impact on our interpretation of the ion selectivity results. Overall, the kinetics of the chimeras are reminiscent of mammalian and snail T-type channels.

II A Structural Model of The Domain II and Domain IV Turrets' Influence on Ion Selectivity in LCa_v3

The Spafford lab has previously identified the Domain II turret as a determinant of ion selectivity in *Lymnaea stagnalis*, where the LCa_v3-12a isoform is sodium-selective and the LCa_v3-12b channel is a more conventional T-type calcium channel (Senatore et al., 2014). LCa_v3-12a is the predominant T-type channel found in the heart, making up 99% of the T-type channel mRNA expressed therein. Exon 12b and exon 12a are found in equal amounts in the brain, and the LCa_v3-12b isoform is dominant in secretory organs like the prostate and albumen, where Ca^{2+} entry plays an important role in secretion (Senatore et al., 2014). Na_v1 channels are not present in the heart of *L. stagnalis*, and instead, selective pressure allowed for changes in the Domain II turret of LCav3 to create a sodium-selective T-type channel that could function as a sodium channel in the heart.

Compared to other 4x6TM channels, the extracellular turrets of T-type calcium channels are cysteine-rich. Most 4x6TM voltage-gated ion channels have a conserved turret-cysteine pattern of eight core cysteines spread out between the Domain I-II-III-IV turrets in a 4-0-2-2 pattern (Stephens et al., 2015). Compared to the extracellular turrets of prokaryotic voltage-gated

ion channels, the 4x6TM channels of eukaryotes all have turrets that are much longer and of variable lengths. Generally speaking, the Domain I turret is the longest, followed by the Domain III turret, and then the Domain II and Domain IV turrets are usually quite similar to one another in terms of length (See Figure 1.16). Although there is variability in the turrets between different voltage-gated ion channel classes, within the classes the size of the turrets and the cysteine configurations seem to be well-conserved. The conservation of the turrets within the Ca_v3 class is highlighted in Figure 1.18, where a phylogenetic tree is presented to illustrate the conservation in length and cysteine configurations of Domain II and Domain IV turret regions of the Ca_v3 channels in vertebrates and invertebrates. The turrets of the T-type calcium channels are longer than those of other 4x6TM channels. Also unique to T-type channels is the presence of alternative splicing in regions coding for the turrets, for example, the alternative splicing to create two versions of the Domain II turret in LCa_v3. This also appears to be occurring in Domain IV in some classes of Cnidarians (Figure 1.15).

The high conservation of the size of the turrets and their cysteine content may indicate that there are functional constraints on the turrets. The results of this thesis suggest that there may be specific configurations of the Domain II L5 and Domain IV L6 turrets that allow them to influence ion selectivity. Different configurations, as a result of sequence divergence and alternative splicing, allow these turrets to alter ion selectivity within T-type channels without dramatically changing other functional properties of the channels. A role for the P-loop residues outside of the selectivity filter in influencing the pore properties of sodium channels has also been suggested (Bénitah et al., 1996; Li et al., 2000). The mechanisms that allow extracellular turrets to act as modulators of ion selectivity are not yet understood.

The overall goal of this research is aimed at creating a comprehensive structural model that could explain how variations in the extracellular turrets of T-type channels can affect the pore to alter ion permeability and selectivity. A mechanism was proposed based on the sequence variations of LCa_v3-12a and LCa_v3-12b, using the cryo-EM structure of $Ca_v1.1$ as a template (see Figures 1.23 and 1.24). The results of this thesis project offer support for the proposed model, although further research is required to confirm the validity of the model.

The semi-autonomous effects that Domain II and Domain IV have on ion selectivity in wild-type T-type channels and T-type channel chimeras provide support for the model in Figure 1.23 and 1.24. Domain IV may be influencing ion selectivity by influencing the positions of the residues of the selectivity filter. Domain II, on the other hand, is more likely to influence ion selectivity by interacting closely with an aspartate residue, called the "molecular beacon", immediately adjacent to the selectivity filter residue in Domain II (Cheng et al., 2010). Given that Domain II and Domain IV are influencing ion selectivity in different ways, according to the model proposed in Figure 1.23 and Figure 1.24, we would expect to find that these turrets have independent effects on ion selectivity.

The sequence of the Domain II turret has a dominant effect on the selectivity of the channel, regardless of the cysteine configuration of this turret or the identity of the Domain IV L6 turret sequence. This can be well explained by the model in Figures 1.23 and 1.24. If the model is correct, then the Domain II turret is influencing ion selectivity in T-type channels by the degree to which the arginine residue (R2 in Figure 1.23) can neutralize the negatively charged aspartate residue at position $D2_{p51}$. Neutralization of this negative charge near the pore would decrease the net negative charge of the molecular beacon near the channel's constricture point (i.e., the selectivity filter). Thus, the selectivity filter would be less capable of attracting highly

positively charged divalent cations like Ca^{2+}, and instead might allow monovalent ions like Na^{+} to permeate the channel pore.

In eukaryotic Na_v1 channels, the net negative charge at the channel's selectivity filter is diminished (compared to Ca_v channels) by the presence of a positively charged lysine residue (Favre et al., 1996; Grigoriev et al., 1996; Heinemann et al., 1992; Schlief et al., 1996; Spafford et al., 1998; Sun et al., 1997). If the Domain II turret is neutralizing the $D2_{p51}$ residue to reduce the net negative charge at the selectivity filter to affect ion selectivity, the overall length and sequence of the Domain II turret would be important in determining a) how closely the arginine residue, R2, can approach the aspartate residue at $D2_{p51}$, and b) how effectively the positively charged residues (e.g., R2) can neutralize the $D2_{p51}$ aspartate before and during ion permeation. The cysteine configuration of the Domain II turret, which is different between LCa_v3-12a, LCa_v3-12b, and $Ca_v3.2$, might be involved in stabilization of the turret structure.

Another possibility is that the electrostatic interaction between the R2 and $D2_{p51}$ residues might serve to stabilize the position of the glutamate selectivity filter residue ($E2_{p50}$), maintaining the diameter of the ion-permeation pathway to allow for precise ion selectivity. The precise positioning of these residues is important in ion selectivity (Chakrabarti et al., 2013; Finol-Urdaneta et al., 2014; Hille, 1975; Kostyuk et al., 1982; Talavera et al., 2001; Tang et al., 2014; Tsien et al., 1987). According to the model proposed in Figure 1.24, the Domain IV turret could affect ion selectivity by slightly altering the position of the Domain IV selectivity filter residue ($D4_{p50}$).

The Domain IV turret has a consistent effect on ion selectivity as well, although the effect of the Domain II L5 turret seems to be dominant. The model proposed here (Figures 1.23 and 1.24) might help to explain the differing contributions of Domain II and Domain IV turrets in

determining ion selectivity. The Domain IV L6 turret is positioned further from the channel's selectivity filter, whereas the Domain II L5 turret is very close to the selectivity filter. Therefore, the Domain IV turret cannot interact with the selectivity filter to the same degree that the Domain II turret can. Nonetheless, the Domain IV turret is in a position to moderately influence the position of the DIV selectivity filter residue ($D4_{p50}$). The Domain IV L6 turret is cysteine-rich, and the presence of these cysteine residues could be important in ion selectivity. Compared to the wild-type channels, the relative positions of these Domain IV turret cysteine residues are altered; such alterations could disrupt the ability of these cysteine residues to influence the position(s) of the selectivity filter residue in Domain IV.

III The Cysteine Configuration and Length of the Domain II and Domain IV Turrets may be Important in their Ability to Influence Ion Selectivity

Changes in ion selectivity are conferred onto LCa_v3 channels and human Ca_v3 channels by the presence of different sequences of the Domain II turrets and Domain IV turrets. The differences between turret variants are mainly their length (i.e., number of amino acids) and their cysteine configuration. In general, the presence of cysteines within the turrets and their configuration among related species seems to be highly conserved (Figures 1.15 and 1.18). But what role could these cysteine residues be playing in the function of the T-type calcium channels? Why do different channels from different organisms with different turret-cysteine configurations display differences in ion selectivity? These questions are yet to be resolved, but there are a number of features of cysteine residues within proteins that might help to explain their role in the turrets of T-type channels.

Cysteine residues in proteins that are secreted or that function in oxidizing environments outside of the cell, in the extracellular matrix or on the extracellular surface of the cell, are capable of undergoing disulphide bond formation. In two-pore domain K2P1 potassium channels, critical cysteine residues within extracellular turrets form a disulphide bond at the apex of an A-frame above the channel (Miller and Long, 2012). This highly organized structure is important for ion selectivity and drug resistance in the K2P1 channel. The cryo-EM structures of the Na_v1 channel from *Electrophorus electricus* (Sato et al., 2001) and the $Ca_v1.1$ channel from humans (Wu et al., 2015) both provide evidence for a highly organized extracellular vestibule above eukaryotic 4x6TM channels (Figures 1.18 and 1.20). Given the results presented within this thesis, it is possible that some of the cysteine residues within the Domain II and Domain IV turrets are contributing to an organized extracellular configuration above the pore, and that this structure is somehow influencing ion selectivity; likely, the organized extracellular structure is interacting with important residues at or near the selectivity filter (refer to Figures 1.23 and 1.24). Alterations in the organization of the extracellular structure, caused by removal or displacement of critical cysteine residues, could explain why the turret chimeras have altered ion selectivity and why LCa_v3 ΔCys mutants display increased sodium permeability compared to their wild-type counterparts.

The results of experiments involving the oxidation of extracellular cysteine residues in L-type Ca^{2+} channels suggest that at least some of the extracellular cysteines (which are mostly concentrated in the turret regions) are not meant to undergo disulphide bond formation, otherwise the open probability of the channels might be affected (Chiamvimonvat et al., 1995). In some instances, disulphide bond formation has been implicated in disrupting the ion-permeation pathway to decrease current amplitudes (Bénitah et al., 1996; Tsushima et al., 1997).

However, the turret cysteines that are unique to T-types (outside of the conserved 4-0-2-2 turret cysteine configuration of L-type channels) might still be available to participate in protein-stabilizing disulphide bonds. Jevtovic-Todorovic and Todorovic have reported results of redox modulations in T-type channels (Jevtovic-Todorovic and Todorovic, 2006). After modulation with the reducing agents dithiothreitol (DTT) or L-cysteine, the currents of T-types were enhanced. Whether these currents were due to sodium influx or calcium influx is not known.

It is also possible that the cysteines are not forming disulphide bonds. Perhaps, these cysteines are helping to stabilize nearby alpha-helices. Alternatively, the cysteine residues may be involved in metal binding. Of course, it is also possible that the entire sequence of the Domain II or Domain IV turret is important in influencing ion selectivity, and the cysteine residues within these sequences are not playing a principal role. There are many sequence differences between the turrets of LCa_v3-12a, LCa_v3-12b, and $Ca_v3.2$. Perhaps, the important difference between the turrets for influencing ion selectivity is the number of amino acids present. Or, it could be possible that there is a critical balance of acidic, basic, hydrophobic, and neutral amino acids within the turrets that determines an overall geometry which allows the turrets to influence ion selectivity. Perhaps, these sequences are concentrating Ca^{2+} or Na^{+} at the mouth of the channel, to facilitate their permeation through the pore. Given the model proposed in Figures 1.23 and 1.24, the shape and length of the turret would be an important factor in a) neutralizing the $D2_{p51}$ residue, and b) influencing the position(s) of the selectivity filter residue(s). Considering the results of ion selectivity experiments with the ΔCys mutants and chimeric LCa_v3 channels, it is apparent that the presence or absence of cysteine residues has the ability to alter the Domain II turret's ability to influence ion selectivity, regardless of whether this is through the formation of

disulphide bonds, stabilization of alpha helices, metal binding, or simply because it is a small hydrophobic residue.

In short, the experimental analysis performed in this thesis cannot provide precise answers to questions regarding the nature of the turrets that allows them to influence ion selectivity. But, the turrets of Domain II and Domain IV are certainly affecting ion selectivity in some way. Considering the nature of the sequence variations between the turrets from vertebrates and invertebrates, the most likely explanation for differences in ion selectivity between the channels is that both the length of the turret and cysteine residues within the turret are playing some role in influencing ion selectivity.

IV Structural and Functional Asymmetry in T-type Calcium Channels

An important consequence of this research is in suggesting a unique feature of T-type calcium channels that allows residues outside of the selectivity filter to influence ion selectivity. The research completed in the Spafford lab is the first instance of residues outside of the selectivity filter consistently affecting ion permeation in T-type channels. This can provide insights to the mechanisms of ion selectivity in eukaryotic 4x6TM channels. Domains I-IV in eukaryotic 4x6TM channels are all a part of the same long polypeptide. Throughout evolutionary history, these Domains have undergone sequence divergence and come to play different roles in the 4x6TM ion channels; this has created some structural and functional asymmetry between the Domains. This asymmetry is further evidenced by the results of this thesis. The turrets from Domain II and Domain IV both influence ion selectivity, but the effect of the Domain II turret is dominant.

There are several other instances throughout the ion channel literature that suggest the asymmetry of the 4x6TM channels is important in various ion channel functions. Particularly, the differences in kinetics between the human Ca_v3 channels ($Ca_v3.1$, $Ca_v3.2$ and $Ca_v3.3$) have been explored by creating chimeras between the Ca_v3 channels. Hamid et al. created chimeras in which they swapped the major transmembrane domains from $Ca_v3.1$ and $Ca_v3.3$, and they found that Domain IV is the most important determinant of activation kinetics and recovery from activation, but they found that multiple Domains work together to influence inactivation kinetics (Hamid et al., 2006). Our findings, in which Domain IV turret character strongly influences recovery from inactivation, are consistent with the Hamid et al. findings. However, another group found that Domain I and the III-IV linker are the most important determinants of activation and inactivation kinetics (Kang et al., 2008). Functional asymmetry within the pore cavity of L-type and T-type calcium channels has also been observed (Shcheglovitov et al., 2007; Talavera et al., 2001). Importantly, the research completed in the Spafford lab is the first to show that the extracellular turrets from different Domains may be contributing asymmetrically to ion selectivity in voltage-gated calcium channels (Guan, 2014; Senatore, 2012; Senatore et al., 2014).

Interestingly, functional asymmetry in terms of ion selectivity has been explored in the prokaryotic sodium channel, Na_vAb, and in an Na_v channel from rabbit skeletal muscle (Finol-Urdaneta et al., 2014; Garber, 1988). In bi-ionic reversal potential experiments, oppositely directed gradients of K^+ and Na^+ affected the degree to which the reversal potential was shifted. With isotonic Na^+ and K^+ solutions on opposite sides of the membrane, the reversal potentials are approximately +45 mV (Na^+ inside) and -100 mV (Na^+ out). Apparently, the direction of the Na^+/K^+ gradient is important in influencing the reversal potentials due to ion-ion interactions.

The authors suggested that this functional asymmetry may reflect a common property among the various members of the P-loop family of channels, which possess a non-selective entrance to the intracellular cavity, and a selectivity filter located nearer to the extracellular mouth (Finol-Urdaneta et al., 2014). The results of our bi-ionic reversal potential experiments were, under certain conditions, inconsistent with our findings from inward sodium permeability experiments (i.e., Ca^{2+}/Na^{+} versus $Ca^{2+}/NMDG^{+}$) and experiments to determine the external Ca^{2+} dependent block of influxing Na^{+} currents. Particularly, these discrepancies occurred when K^{+} was the monovalent charge carrier in the internal solution. Perhaps, these inconsistencies can be explained by considering the asymmetry of the extracellular and intracellular entrances to the T-type calcium channel pore. The chimeric T-type channels and delta-cysteine mutants were different from the wild-type channels only on the extracellular surface, where the turrets are found. Alterations in the sequence of the turrets would not affect the intracellular surface, where monovalent ions are approaching the channel during bi-ionic reversal potential experiments. Theoretically, this could differentially affect the behaviour of the channels in bi-ionic conditions.

V Future Directions

In order to improve our confidence in the model for turret involvement in ion selectivity, which was proposed in this thesis (Figure 1.23 and Figure 1.24), future experiments are necessary.

Investigating the ion selectivity of the chimeras $Ca_v3.2$-12a and $Ca_v3.2$-12b will be necessary. These chimeras have the Domain II L5 turret sequence of $Ca_v3.2$ replaced by either the LCa_v3 exon 12a sequence ($Ca_v3.2$-12a) or the LCa_v3 exon 12b sequence ($Ca_v3.2$-12b). The

chimeras were created by Amrit Mehta, an MSc student in the Spafford lab. These chimeras express in HEK293T cells, and whole-cell patch clamp currents are obtainable. However, the amplitude of their whole-cell currents is reduced compared to the wild-type $Ca_v3.2$ channel in HEK293T cells. This may be due to neutralization of the $D2_{p51}$, such that the ion pathway through the pore is no longer favourable. Alternatively, the formation of disulphide bonds may be impeding current flow (Bénitah et al., 1996; Tsushima et al., 1997). Or, for whatever reason, the expression levels of the chimeric Cav3.2-12a and Cav3.2-12b channels are decreased. Nonetheless, we were able to record these channels in conditions to determine inward sodium permeability (i.e., Ca^{2+}/$NMDG^{+}$ versus Ca^{2+}/Na^{+}). Only a single recording for each chimera has been collected thus far. The results of these recordings suggest that $Ca_v3.2$-12a becomes more similar to LCa_v3-12a in terms of sodium permeability and $Ca_v3.2$-12b becomes more like LCa_v3-12b. $Ca_v3.2$-12a had a fold-increase of ~4 in sodium and calcium and $Ca_v3.2$-12b had a fold-increase of ~1.7. Both $Ca_v3.2$-12a and $Ca_v3.2$-12b have increased sodium permeability compared to the wild-type $Ca_v3.2$ channel (fold-increase of 1.32 ± 0.046). Of course, more replicates will need to be gathered for both $Ca_v3.2$-12a and $Ca_v3.2$-12b to confirm the preliminary results.

To provide support for the Domain II influence of $D2_{p51}$ and the plausibility of the model presented in Figure 1.23, a mutant channel with the $D2_{p51}$ residue removed should be investigated. Electrophysiological analysis of such a mutant would allow for the final component of our hypothesis to be tested (See Section 2). A mutant in which the $D2_{p51}$ residue within $Ca_v3.2$ (at position 975 in the $Ca_v3.2$ sequence) has been substituted for asparagine has been created. This mutant has been dubbed $Ca_v3.2$ DII_{D975N}. This channel expresses in HEK293T cells but, like $Ca_v3.2$-12a and $Ca_v3.2$-12b, the current amplitudes are diminished. The $D2_{p51}$ residue is present in all known voltage-gated calcium channels, including the Ca_v1, Ca_v2, and Ca_v3

channels. An analogous aspartate residue was necessary in engineering a calcium-selective bacterial Na_vAb sodium channel (Tang et al., 2014). According to a model by Cheng et al., this residue serves as a "molecular beacon" for calcium, attracting it to the calcium channel's pore. This position may serve as a binding site for Ca^{2+} as it begins to permeate the pore. So far, recordings in external Ca^{2+} solutions have not produced any currents through the $Ca_v3.2$ DII_{D975N} mutant, but there are small currents in Na^+-containing external solutions. These preliminary recordings suggest that these channels are more likely to pass sodium currents instead of calcium currents.

Domain I and Domain III turrets should also be explored as possible determinants of ion selectivity in T-type calcium channels. It is clear from the results of this thesis and from previous research conducted in the Spafford lab that Domain II and Domain IV turrets are determinants of ion selectivity. However, replacements of the snail Domain II turret and Domain IV turret sequences with those of $Ca_v3.2$ are sufficient in creating an LCa_v3 channel with the calcium-selectivity of $Ca_v3.2$; but it appears that the turrets have a semi-autonomous effect, and perhaps there is an interaction occurring between turrets from all of the transmembrane domains. It might be possible to create an LCa_v3 channel with the selectivity of $Ca_v3.2$ (or vice-versa) if all of the turrets were exchanged, which would require swapping Domain I and/or Domain III turrets as well. A chimera in which the Domain I sequence from $Ca_v3.2$ replaced the Domain I turret sequence of LCa_v3 (i.e., LCa_v3-12a $DI_{\alpha 1hL}$) was cloned, but it failed to express in HEK293T cells. Interestingly, Karmazinova et al. investigated mutants in which the cysteine residues in the Domain I turret of Cav3.1 were substituted for alanine residues. Substitution of the core cysteine residues in Domain I (see Figure 1.14) produced non-functional channels. However, cysteine-to-alanine substitutions involving the Domain I turret cysteine residues that are unique to T-types

(positions 298 and 313 in $Ca_v3.1$) resulted in changes in activation and Ca^{2+} current amplitude. From these results, it is reasonable to believe that these cysteine residues could be playing some role in the ion permeation pathways. The creation of the chimera $Ca_v3.2\text{-}DI_{LCav3}$ might produce measurable currents. Alternatively, chimeras between LCa_v3 and $Ca_v3.1$ or $Ca_v3.3$ could be explored.

Single channel recordings of the different T-type channels would also be valuable in confirming or refuting the conclusions drawn from this research. Shchlegovlitov, Kostyuk and Shuba (2007) performed experiments of single-channel recordings of $Ca_v3.1$, $Ca_v3.2$, and $Ca_v3.3$ and determined that the ability of $Ca_v3.1$ and $Ca_v3.2$ to discriminate between Ca^{2+} and Ba^{2+} ions was dependent on the ion's ability to affect channel open-probability. On the other hand, $Ca_v3.3$ was able to discriminate between these ions based on intra-pore binding affinity (Shcheglovitov et al., 2007). Single channel recordings of the LCa_v3-12a, LCa_v3-12b, $Ca_v3.2$, $Ca_v3.2$-12a, $Ca_v3.2$-12b, LCa_v3-12a $DIV_{\alpha 1hL}$, LCa_v3-12b $DIV_{\alpha 1hL}$, $LCa_v3\text{-}DII_{\alpha 1hL}$ and $LCa_v3\text{-}DII_{\alpha 1hL}$ $DIV_{\alpha 1hL}$ in various conditions of intracellular and extracellular ions would allow us to observe whether single-channel conductance and/or gating (e.g. open probability) are affected.

Ultimately, the best way to elucidate the mechanisms of ion selectivity in T-type calcium channels is to have a reliable structural model based upon a well-resolved image of the structure of the channel. With cryo-electron microscopy (cryo-EM) becoming more widely available and the recent success in visualizing the human $Ca_v1.1$ channel (Wu et al., 2015), we might have access to a valid image of a T-type channel in the near-future.

VI Implications of the Current Research

By exploring critical structures within T-type calcium channels, we can draw conclusions regarding mechanisms of ion selectivity and permeation. This may provide clues about the evolution of these channels, the selective pressures that led to their creation, and the physiological roles that they play in the organs of various organisms. Furthermore, understanding fundamental features of these channels might allow scientists to devise improved permeation models and design novel channel blockers. From Wendy Guan's MSc thesis, we know that cysteine-to-alanine substitutions in the Domain II turret of LCa_v3 channels results in changes in nickel (Ni^{2+}) block; there is also some evidence that the drug block of TTA-P2, a potent T-type channel blocker, is affected by cysteine-substitution mutations in LCa_v3 channels (Choe et al., 2011; Guan, 2014). The presence of an extracellular structure contributing to ion selectivity above the T-type channel pore may make it possible to design drugs that selectively block T-type over L-type and N-type calcium channels, and differentiate amongst different mammalian Ca_v3 isoforms (i.e. selective block of $Ca_v3.1$, $Ca_v3.2$, or $Ca_v3.3$). As T-types are implicated in childhood absence epilepsy, chronic pain, and cancer, the discovery and development of effective T-type channel blockers is certainly a worthwhile endeavour (Cheong and Shin, 2013; Eckle et al., 2014; Taylor et al., 2008; Todorovic and Jevtovic-Todorovic, 2013). Before this can be accomplished, a thorough understanding of structure-function relationships governing ion selectivity in T-type calcium channels is necessary. Hopefully, the research presented in this thesis can bring the scientific community one-step closer to a complete understanding calcium channels.

6. References

Almers, B.Y.W., McCleskey, E.W., 1984. Non-selective conductance in calcium channels of frog muscle: calcium selectivity in a single-file pore. J. Physiol. 353, 585–608.

Anderson, P.A.V., Greenberg, R.M., 2001. Phylogeny of ion channels: Clues to structure and function. Comp. Biochem. Physiol. 129, 17–28.

Bean, B.P., 1985. Two kinds of calcium channels in canine atrial cells. Differences in kinetics, selectivity, and pharmacology. J. Gen. Physiol. 86, 1–30. doi:10.1085/jgp.86.1.1

Bénitah, J.P., Tomaselli, G.F., Marban, E., 1996. Adjacent pore-lining residues within sodium channels identified by paired cysteine mutagenesis. Proc. Natl. Acad. Sci. U. S. A. 93, 7392–6. doi:DOI 10.1073/pnas.93.14.7392

Birnboim, H.C., Doly, J., 1979. A rapid alkaline extraction procedure for screening recombinant plasmid DNA. Nucleic Acids Res. 7, 1513–1523.

Brohawn, S.G., del Marmol, J., MacKinnon, R., 2012. Crystal Structure of the Human K2P TRAAK, a Lipid- and Mechano-Sensitive K+ Ion Channel. Science (80-.). 335, 436–441.

Carbone, E., Lux, H.D., 1987. Kinetics and selectivity of a low-voltage-activated calcium current in chick and rat sensory neurones. J. Physiol. 386, 547–570.

Catterall, W.A., 2010. Ion channel voltage sensors: Structure, function, and pathophysiology. Neuron 67, 915–928. doi:10.1016/j.neuron.2010.08.021

Catterall, W.A., 2000. From Ionic Currents to Molecular Mechanisms: The structure and function of voltage-gated sodium channels. Neuron 26, 13–25. doi:10.1016/S0896-6273(00)81133-2

Catterall, W.A., 1986. Voltage-dependent gating of sodium channels: correlating structure and

function. Trends Neurosci. 9, 7–10. doi:10.1016/0166-2236(86)90004-4

Cens, T., Rousset, M., Collet, C., Charreton, M., Garnery, L., Le Conte, Y., Chahine, M., Sandoz, J.C., Charnet, P., 2015. Molecular characterization and functional expression of the Apis mellifera voltage-dependent Ca2+ channels. Insect Biochem. Mol. Biol. 58, 12–27. doi:10.1016/j.ibmb.2015.01.005

Chakrabarti, N., Ing, C., Payandeh, J., Zheng, N., Catterall, W.A., Pomès, R., 2013. Catalysis of Na+ permeation in the bacterial sodium channel NavAb. Proc. Natl. Acad. Sci. U. S. A. 110, 11331–6. doi:10.1073/pnas.1309452110

Chemin, J., Monteil, A., Bourinet, E., Lory, P., 2001. Alternatively Spliced alpha1G (CaV 3 .1) Intracellular Loops Promote Specific T-Type Ca2+ Channel Gating Properties. Biophys. J. 80, 1238–1250. doi:10.1016/S0006-3495(01)76100-0

Chemin, J., Monteil, A., Perez-Reyes, E., Bourinet, E., Nargeot, J., Lory, P., 2002. Specific contribution of human T-type calcium channel isotypes (alpha(1G), alpha(1H) and alpha(1I)) to neuronal excitability. J. Physiol. 540, 3–14. doi:10.1113/jphysiol.2001.013269

Cheng, R.C.K., Tikhonov, D.B., Zhorov, B.S., 2010. Structural modeling of calcium binding in the selectivity filter of the L-type calcium channel. Eur. Biophys. J. 39, 839–853. doi:10.1007/s00249-009-0574-2

Cheong, E., Shin, H.-S., 2013. T-type Ca^{2+} channels in absence epilepsy. Biochim. Biophys. Acta 1828, 1560–71. doi:10.1016/j.bbamem.2013.02.002

Chiamvimonvat, N., O'Rourke, B., Kamp, T.J., Kallen, R.G., Hofmann, F., Flockerzi, V., Marban, E., 1995. Functional Consequences of Sulfhydryl Modification in the Pore-Forming Subunits of Cardiovascular Ca2+ and Na+ Channels. Circ. Res. 76 , 325–334. doi:10.1161/01.RES.76.3.325

Choe, W., Messinger, R.B., Leach, E., Eckle, V.-S., Obradovic, A., Salajegheh, R., Jevtovic-Todorovic, V., Todorovic, S.M., 2011. TTA-P2 is a potent and selective blocker of T-type calcium channels in rat sensory neurons and a novel antinociceptive agent. Mol. Pharmacol. 80, 900–10. doi:10.1124/mol.111.073205.central

Dang, T.X., McCleskey, E.W., 1998. Ion channel selectivity through stepwise changes in binding affinity. J. Gen. Physiol. 111, 185–193.

Doyle, D.A., Cabral, J.M., Pfuetzner, R.A., Kuo, A., Gulbis, J.M., Cohen, S.L., Chait, B.T., MacKinnon, R., 1998. The Structure of the Potassium Channel: Molecular Basis of K+ Conduction and Selectivity. Science 280, 69–77. doi:10.1126/science.280.5360.69

Eckle, V.-S., Shcheglovitov, A., Vitko, I., Dey, D., Yap, C.C., Winckler, B., Perez-Reyes, E., 2014. Mechanisms by which a CACNA1H mutation in epilepsy patients increases seizure susceptibility. J. Physiol. 592, 795–809. doi:10.1113/jphysiol.2013.264176

Eisenman, G., Sandbolm, J.P., Walker, J.L., 1967. Membrane structure and ion permeation. Study of ion exchange membrane structure and function is relevant to analysis of biological ion permeation. Science 155, 965–974.

Ellinor, P.T., Yang, J., Sather, W.A., Zhang, J.F., Tsien, R.W., 1995. Ca 2+ channel selectivity at a single locus for high-affinity Ca 2+ interactions. Neuron 15, 1121–1132.

Ertel, E.A., Campbell, K.P., Harpold, M.M., Hofmann, F., Mori, Y., Perez-Reyes, E., Schwartz, A., Snutch, T.P., Tanabe, T., Birnbaumer, L., Tsien, R.W., Catterall, W.A., 2000. Nomenclature of voltage-gated calcium channels. Neuron 25, 533–535. doi:10.1080/13518040701205365

Eyring, H., Lumry, R., Woodbury, J.W., 1949. Some applications of modern rate theory to physiological systems. Rec. Chem. Prog. 10, 100–114.

Favre, I., Moczydlowski, E., Schild, L., 1996. Voltage-Gated Sodium. Biophys. J. 71, 3110–3125.

Finol-Urdaneta, R.K., Wang, Y., Al-Sabi, A., Zhao, C., Noskov, S.Y., French, R.J., 2014. Sodium channel selectivity and conduction: prokaryotes have devised their own molecular strategy. J. Gen. Physiol. 143, 157–171. doi:10.1085/jgp.201311037

Friel, D.D., Tsien, R.W., 1989. Voltage-gated calcium channels: Direct observation of the anomalous mole fraction effect at the single-channel level. Proc. Natl. Acad. Sci. U. S. A. 86, 5207–5211. doi:10.1073/pnas.86.13.5207

Garber, S.S., 1988. Symmetry and asymmetry of permeation through toxin-modified Na+ channels. Biophys. J. 54, 767–776.

Glick, B.R., 1995. Metabolic Load and Heterologous Gene Expression. Biotechnol. Adv. 13, 247–261.

Goldman, D.E., 1943. Potential, Impedance, and Rectification in Membranes. J. Gen. Physiol. 27, 37–60. doi:10.1085/jgp.27.1.37

Grant, A.O., 2009. Cardiac ion channels. Circ. Arrhythmia Electrophysiol. 2, 185–194. doi:10.1161/CIRCEP.108.789081

Grigoriev, N.G., Spafford, J.D., Przysiezniak, J., Spencer, A.N., 1996. A cardiac-like sodium current in motor neurons of a jellyfish. J. Neurophysiol. 76, 2240–2249.

Guan, W., 2014. Domain II (S5-P) region in Lymnaea T-type calcium channels and its role in determining biophysical properties , ion selectivity and drug sensitivity. University of Waterloo.

Gur Barzilai, M., Reitzel, A.M., Kraus, J.E.M., Gordon, D., Technau, U., Gurevitz, M., Moran, Y., 2012. Convergent Evolution of Sodium Ion Selectivity in Metazoan Neuronal Signaling.

Cell Rep. 2, 242–248. doi:10.1016/j.celrep.2012.06.016

Guy, H.R., Seetharamulu, P., 1986. Molecular model of the action potential sodium channel. Proc. Natl. Acad. Sci. U. S. A. 83, 508–512. doi:10.1073/pnas.83.2.508

Hagiwara, S., Ozawa, S., Sand, O., 1975. Voltage clamp analysis of two inward current mechanisms in the egg cell membrane of a starfish. J. Gen. Physiol. 65, 617–644. doi:10.1085/jgp.65.5.617

Hamid, J., Peloquin, J.B., Monteil, A., Zamponi, G.W., 2006. Determinants of the differential gating properties of Cav3.1 and Cav3.3 T-type channels: A role of domain IV? Neuroscience 143, 717–728. doi:10.1016/j.neuroscience.2006.08.023

Hanahan, D., 1983. Studies on transformation of Escherichia coli with plasmids. J. Mol. Biol. 166, 557–580.

Heinemann, S.H., Terlau, H., Stuhmer, W., Imoto, K., Numa, S., 1992. Calcium channel characteristics conferred on the sodium channel by single mutations. Nature 356, 441–3. doi:10.1038/355242a0

Hess, P., Lansman, J.B., Tsien, R.W., 1986. Calcium Channel Selectivity for Divalent and Monovalent Cations Voltage and Concentration Dependence of Single Channel Current in Ventricular Heart Cells 88.

Hess, P., Tsien, R.W., 1984. Mechanism of ion permeation through calcium channels. Nature 309, 453–6.

Hille, B., 2001. Ion Channels of Excitable Membranes, 3rd ed. Sinauer Associates, Sunderland, Massachusetts.

Hille, B., 1975. Ionic selectivity, saturation, and block in sodium channels. A four-barrier model. J. Gen. Physiol. 66, 535–60. doi:10.1085/jgp.66.5.535

Hille, B., 1971. The permeability of the sodium channel to organic cations in myelinated nerve. J. Gen. Physiol. 58, 599–619. doi:10.1085/jgp.58.6.599

Hille, B., Schwarz, W., 1978. Potassium channels as multi-ion single-file pores. J. Gen. Physiol. 72, 409–442. doi:10.1085/jgp.72.4.409

Hodgkin, A.L., Katz, B., 1949. The effect of sodium ions on the electrical activity of the giant axon of the squid. J. Physiol. 108, 37–77. doi:10.1016/0165-3806(85)90091-4

Jegla, T., Zmasek, C., Batalov, S., Nayak, S.K., 2009. Evolution of the Human Ion Channel Set. Comb. Chem. High Throughput Screen. 12, 2–23. doi:10.2174/138620709787047957

Jevtovic-Todorovic, V., Todorovic, S.M., 2006. The role of peripheral T-type calcium channels in pain transmission. Cell Calcium 40, 197–203. doi:10.1016/j.ceca.2006.04.024

Jiang, M., Chen, G., 2006. High Ca2+-phosphate transfection efficiency in low-density neuronal cultures. Nat. Protoc. 1, 695–700. doi:10.1038/nprot.2006.86

Jiang, Y., Lee, A., Chen, J., Cadene, M., Chait, B.T., MacKinnon, R., 2002a. Crystal structure and mechanism of a calcium-gated potassium channel. Nature 417, 515–22. doi:10.1038/417515a

Jiang, Y., Lee, A., Chen, J., Cadene, M., Chait, B.T., MacKinnon, R., 2002b. The open pore conformation of potassium channels. Nature 417, 523–526. doi:10.1038/417523a

Jiang, Y., Lee, A., Chen, J., Ruta, V., Cadene, M., Chait, B.T., MacKinnon, R., 2003. X-ray structure of a voltage-dependent K+ channel. Nature 423, 33–41. doi:10.1038/nature01580

Kang, H.W., Park, J.Y., Lee, J.H., 2008. Distinct contributions of different structural regions to the current kinetics of the Cav3.3 T-type Ca2+ channel. Biochim. Biophys. Acta 1778, 2740–2748. doi:10.1016/j.bbamem.2008.08.002

Kostyuk, P.G., Fedulova, S.A., Veselovsky, N.S., 1985. Two types of calcium channels in the

somatic membrane of new-born rat dorsal root ganglion neurones. J. Physiol. 359, 431–446.

Kostyuk, P.G., Mironov, S.L., Doroshenko, P.A., 1982. A three-barrier model for describing the energy profile of the calcium channel in the molluscan neuron membrane. Neurophysiology 13, 242–250.

Kostyuk, P.G., Mironov, S.L., Shuba, Y.M., 1984. Two selective filters in the calcium channel of the molluscan neuron somatic membrane. Neurophysiology 15, 314–319.

Li, R.A., Vélez, P., Chiamvimonvat, N., Tomaselli, G.F., Marban, E., 2000. Charged residues between the selectivity filter and S6 segments contribute to the permeation phenotype of the sodium channel. J. Gen. Physiol. 115, 81–92. doi:10.1085/jgp.115.1.81

Lipkind, G.M., Fozzard, H. a, 2008. Voltage-gated Na channel selectivity: the role of the conserved Domain III lysine residue. J. Gen. Physiol. 131, 523–9. doi:10.1085/jgp.200809991

Llinas, R., Yarom, Y., 1981. Electrophysiology of mammalian inferior olivary neurones in vitro. Different types of voltage-dependent ionic conductances. J. Physiol. 315, 549–567.

Long, S.B., Campbell, E.B., MacKinnon, R., 2005. Crystal structure of a mammalian voltage-dependent Shaker family K+ channel. Science 309, 897–903. doi:10.1524/ncrs.2006.0167

Matteson, D.R., Armstrong, C.M., 1986. Properties of two types of calcium channels in clonal pituitary cells. J. Gen. Physiol. 87, 161–182. doi:10.1085/jgp.87.1.161

McCleskey, E.W., 1999. Calcium channel permeation: A field in flux. J. Gen. Physiol. 113, 765–772. doi:10.1085/jgp.113.6.765

McCusker, E.C., D'Avanzo, N., Nichols, C.G., Wallace, B.A., 2011. Simplified bacterial "pore" channel provides insight into the assembly, stability, and structure of sodium channels. J. Biol. Chem. 286, 16386–16391. doi:10.1074/jbc.C111.228122

Miller, A.N., Long, S.B., 2012. Crystal Structure of the Human Two-Pore Domain Potassium Channel K2P1. Science 335, 432–436. doi:10.5061/dryad.sh7rm2pt

Mitsuiye, T., Shinagawa, Y., Noma, A., 2000. Sustained inward current during pacemaker depolarization in mammalian sinoatrial node cells. Circ. Res. 87, 88–91. doi:10.1161/01.RES.87.2.88

Molleman, A., 2003. Patch clamping: An introductory guide to patch clamp. J. Wiley, New York.

Murata, Y., Iwasaki, H., Sasaki, M., Inaba, K., Okamura, Y., 2005. Phosphoinositide phosphatase activity coupled to an intrinsic voltage sensor. Nature 435, 1239–43. doi:10.1038/nature03650

Nilius, B., Hess, P., Lansman, J.B., Tsien, R.W., 1985. A novel type of cardiac calcium channel in ventricular cells. Nature 316, 443–446.

Nimigean, C.M., Allen, T.W., 2011. Perspectives on: Ion selectivity. Origins of ion selectivity in potassium channels from the perspective of channel block. J. Gen. Physiol. 137, 405–413. doi:10.1085/jgp.201010551

Noskov, S.Y., Roux, B., 2006. Ion selectivity in potassium channels. Biophys. Chem. 124, 279–291. doi:10.1016/j.bpc.2006.05.033

Nowycky, M.C., Fox, A.P., Tsien, R.W., 1985. Three types of neuronal calcium channel with different calcium agonist sensitivity. Nature 316, 440–443. doi:10.1038/316440a0

Oelstrom, K., Goldschen-Ohm, M.P., Holmgren, M., Chanda, B., 2014. Evolutionarily conserved intracellular gate of voltage-dependent sodium channels. Nat. Commun. 5, 1–9. doi:10.1038/ncomms4420

Ono, K., Iijima, T., 2010. Cardiac T-type Ca2+ channels in the heart. J. Mol. Cell. Cardiol. 48,

65–70. doi:10.1016/j.yjmcc.2009.08.021

Park, H.J., Park, S.J., Ahn, E.J., Lee, S.Y., Seo, H., Lee, J.H., 2013. Asp residues of the Glu-Glu-Asp-Asp pore filter contribute to ion permeation and selectivity of the Cav3.2 T-type channel. Cell Calcium 54, 226–235. doi:10.1016/j.ceca.2013.06.006

Payandeh, J., Scheuer, T., Zheng, N., Catterall, W.A., 2011. The crystal structure of a voltage-gated sodium channel. Nature 475, 353–358. doi:10.1038/nature10238

Ren, D., Navarro, B., Xu, H., Yue, L., Shi, Q., Clapham, D.E., 2001. A Prokaryotic Voltage-Gated Sodium Channel. Science 294, 2372–2375. doi:10.1126/science.1065635

Sather, W.A., McCleskey, E.W., 2003. Permeation and selectivity in calcium channels. Annu. Rev. Physiol. 65, 133–159. doi:10.1146/annurev.cellbio.18.031802.150501

Sato, C., Ueno, Y., Asai, K., Takahashi, K., Sato, M., Engel, A., Fujiyoshi, Y., 2001. The voltage-sensitive sodium channel is a bell-shaped molecule with several cavities. Nature 409, 1047–1051. doi:10.1038/35059098

Schlief, T., Schönherr, R., Imoto, K., Heinemann, S.H., 1996. Pore properties of rat brain II sodium channels mutated in the selectivity filter domain. Eur. Biophys. J. 25, 75–91. doi:10.1007/s002490050020

Senatore, A., 2012. Alternative splicing of Lymnaea Ca v 3 and NALCN ion channel genes serves to alter biophysical properties , membrane expression , and ion selectivity by. University of Waterloo.

Senatore, A., Boone, A.N., Spafford, J.D., 2011. Optimized transfection strategy for expression and electrophysiological recording of recombinant voltage-gated ion channels in HEK-293T cells. J. Vis. Exp. 4–11. doi:10.3791/2314

Senatore, A., Guan, W., Boone, A.N., Spafford, J.D., 2014. T-type channels become highly

permeable to sodium ions using an alternative extracellular turret region (S5-P) outside the selectivity filter. J. Biol. Chem. 289, 11952–11969. doi:10.1074/jbc.M114.551473

Senatore, A., Monteil, A., van Minnen, J., Smit, A.B., Spafford, J.D., 2013. NALCN Ion Channels Have Alternative Selectivity Filters Resembling Calcium Channels or Sodium Channels. PLoS One 8, e55088. doi:10.1371/journal.pone.0055088

Senatore, A., Spafford, J.D., 2012. Gene transcription and splicing of T-type channels are evolutionarily-conserved strategies for regulating channel expression and gating. PLoS One 7, e37409. doi:10.1371/journal.pone.0037409

Senatore, A., Spafford, J.D., 2010. Transient and big are key features of an invertebrate T-type channel (LCav3) from the central nervous system of Lymnaea stagnalis. J. Biol. Chem. 285, 7447–7458. doi:10.1074/jbc.M109.090753

Senatore, A., Zhorov, B.S., Spafford, J.D., 2012. Cav3 T-type calcium channels. Wiley Interdiscip. Rev. Membr. Transp. Signal. 1, 467–491. doi:10.1002/wmts.41

Shaya, D., Findeisen, F., Abderemane-Ali, F., Arrigoni, C., Wong, S., Nurva, S.R., Loussouarn, G., Minor, D.L., 2014. Structure of a prokaryotic sodium channel pore reveals essential gating elements and an outer ion binding site common to eukaryotic channels. J. Mol. Biol. 426, 467–483. doi:10.1016/j.jmb.2013.10.010

Shcheglovitov, A., Kostyuk, P., Shuba, Y., 2007. Selectivity signatures of three isoforms of recombinant T-type Ca2+ channels. Biochim. Biophys. Acta 1768, 1406–1419. doi:10.1016/j.bbamem.2007.02.017

Shcheglovitov, A.K., Shuba, Y.M., 2006. Sodium/calcium selectivity of cloned calcium T-type channels. Neurophysiology 38, 149–157.

Shuba, Y.M., 2014. Models of calcium permeation through T-type channels. Pflugers Arch. Eur.

J. Physiol. 466, 635–644. doi:10.1007/s00424-013-1437-3

Spafford, J.D., Chen, L., Feng, Z.-P., Smit, A.B., Zamponi, G.W., 2003. Expression and modulation of an invertebrate presynaptic calcium channel alpha1 subunit homolog. J. Biol. Chem. 278, 21178–21187. doi:10.1074/jbc.M302212200

Spafford, J.D., Dunn, T., Smit, A.B., Syed, N.I., Zamponi, G.W., 2006. In vitro characterization of L-type calcium channels and their contribution to firing behavior in invertebrate respiratory neurons. J. Neurophysiol. 95, 42–52. doi:10.1152/jn.00658.2005

Spafford, J.D., Spencer, A.N., Gallin, W.J., 1998. A putative voltage-gated sodium channel alpha subunit (PpSCN1) from the hydrozoan jellyfish, Polyorchis penicillatus: structural comparisons and evolutionary considerations. Biochem. Biophys. Res. Commun. 244, 772–780. doi:10.1006/bbrc.1998.8332

Stephens, R.F., Guan, W., Zhorov, B.S., Spafford, J.D., 2015. Selectivity filters and cysteine-rich extracellular loops in voltage-gated sodium, calcium, and NALCN channels. Front. Physiol. 6, 153. doi:10.3389/fphys.2015.00153

Strong, M., Chandy, K.G., Gutman, G.A., 1993. Molecular evolution of voltage-sensitive ion channel genes: on the origins of electrical excitability. Mol. Biol. Evol. 10, 221–242.

Stühmer, W., Conti, F., Suzuki, H., Wang, X.D., Noda, M., Yahagi, N., Kubo, H., Numa, S., 1989. Structural parts involved in activation and inactivation of the sodium channel. Nature 339, 597–603. doi:10.1038/339597a0

Sun, Y.-M., Favre, I., Schild, L., Moczydlowski, E., 1997. On the structural basis for size-selective permeation of organic cation through the voltage-gated sodium channel. J. Gen. Physiol. 110, 693–715.

Talavera, K., Janssens, A., Klugbauer, N., Droogmans, G., Nilius, B., 2003. Pore structure

influences gating properties of the T-type Ca2+ channel alpha1G. J. Gen. Physiol. 121, 529–40. doi:10.1085/jgp.200308794

Talavera, K., Staes, M., Janssens, A., Klugbauer, N., Droogmans, G., Hofmann, F., Nilius, B., 2001. Aspartate Residues of the Glu-Glu-Asp-Asp (EEDD) Pore Locus Control Selectivity and Permeation of the T-type Ca2+ Channel alpha1G. J. Biol. Chem. 276, 45628–45635. doi:10.1074/jbc.M103047200

Tang, L., Gamal El-Din, T.M., Payandeh, J., Martinez, G.Q., Heard, T.M., Scheuer, T., Zheng, N., Catterall, W. a, 2014. Structural basis for Ca2+ selectivity of a voltage-gated calcium channel. Nature 505, 56–61. doi:10.1038/nature12775

Taylor, J.T., Zeng, X.-B., Pottle, J.E., Lee, K., Wang, A.R., Yi, S.G., Scruggs, J.A.S., Sikka, S.S., Li, M., 2008. Calcium signaling and T-type calcium channels in cancer cell cycling. World J. Gastroenterol. 14, 4984–4991. doi:10.3748/wjg.14.4984

Thomas, P., Smart, T.G., 2005. HEK293 cell line: A vehicle for the expression of recombinant proteins. J. Pharmacol. Toxicol. Methods 51, 187–200. doi:10.1016/j.vascn.2004.08.014

Todorovic, S.M., Jevtovic-Todorovic, V., 2013. Neuropathic pain: Role for presynaptic T-type channels in nociceptive signaling. Pflugers Arch. - Eur. J. Physiol. Eur. J. Physiol. 465, 921–927. doi:10.1007/s00424-012-1211-y

Tsai, C.J., Tani, K., Irie, K., Hiroaki, Y., Shimomura, T., McMillan, D.G., Cook, G.M., Schertler, G.F.X., Fujiyoshi, Y., Li, X.D., 2013. Two alternative conformations of a voltage-gated sodium channel. J. Mol. Biol. 425, 4074–4088. doi:10.1016/j.jmb.2013.06.036

Tsien, R.W., Hess, P., McCleskey, E.W., Rosenberg, R.L., 1987. Calcium channels: mechanisms of selectivity, permeation, and block. Annu. Rev. Biophys. Biophys. Chem. 16, 265–290.

doi:10.1146/annurev.biophys.16.1.265

Tsushima, R.G., Li, R.A., Backx, P.H., 1997. P-loop flexibility in Na+ channel pores revealed by single- and double-cysteine replacements. J. Gen. Physiol. 110, 59–72. doi:10.1085/jgp.110.1.59

Veselovski, N., Fedulova, S., 1983. 2 Types of calcium channels in the somatic membrane of spinal ganglion neurons in the rat. Dokl Akad Nauk SSSR 268, 747–750.

Webster, S.M., del Camino, D., Dekker, J.P., Yellen, G., 2004. Intracellular gate opening in Shaker K+ channels defined by high-affinity metal bridges. Nature 428, 864–868. doi:10.1038/nature02468

Wilfinger, W.W., Mackey, K., Chomcynski, P., 1997. Effect of pH and Ionic Strength on The Spectrophotometric Asssessment of Nucleic Acid Purity. Biotechniques 22, 474–481. doi:10.2144/000113277

Wu, J., Yan, Z., Li, Z., Yan, C., Lu, S., Dong, M., Yan, N., 2015. Structure of the voltage-gated calcium channel Cav1.1 complex. Science 350, aad2395–1. doi:10.1126/science.aad2395

Yue, L., Navarro, B., Ren, D., Ramos, A., Clapham, D.E., 2002. The Cation Selectivity Filter of the Bacterial Sodium Channel, NaChBac. J. Gen. Physiol. 120, 845–853. doi:10.1085/jgp.20028699

Zamponi, G.W., 2005. Voltage-Gated Calcium Channels, Molecular Biology Intelligence Unit. Kluwer Academic/ Plenum Publishers, New York, New York.

Zhang, X., Ren, W., DeCaen, P., Yan, C., Tao, X., Tang, L., Wang, J., Hasegawa, K., Kumasaka, T., He, J., Wang, J., Clapham, D.E., Yan, N., 2012. Crystal structure of an orthologue of the NaChBac voltage-gated sodium channel. Nature 486, 130–134. doi:10.1038/nature11054

Zhao, Y., Yarov-Yarovoy, V., Scheuer, T., Catterall, W.A., 2004. A gating hinge in Na+

channels: A molecular switch for electrical signaling. Neuron 41, 859–865. doi:10.1016/S0896-6273(04)00116-3

Zhou, W., Chung, I., Liu, Z., Goldin, A.L., Dong, K., 2004. A voltage-gated calcium-selective channel encoded by a sodium channel-like gene. Neuron 42, 101–112. doi:10.1016/S0896-6273(04)00148-5

7. Appendix

A1. Sequences of Oligonucleotides used in the Cloning of Chimeric LCav3 T-type Calcium Channels

DIV_{a1hL} synthetic Oligonucleotide sequence for insertion into LCav3-12a DIV_{a1hL}, LCav3-12b DIV_{a1hL}, and LCav3- DII_{a1hL} DIV_{a1hL} (SpeI – XhoI)

ACTAGTGTTTTTATTCTGGAAGCTGTAATGAAAATTATAGCACTGGGCTTTTACCGAT
ACATTAGAGACAGATGGAACCAGCTGGACATCATGATAGTCATCTTGTCAATAGTG
GGTATTGTGCTGGAAGAGATGAGGACCAATGTAATACCCATCAACCCGACCATCAT
AAGAGTCATGAGAGTACTTAGGATTGCCAGGGTGCTTAAGCTTCTGAAAATGGCCA
AAGGAATCAGGGCTTTGTTGGACACCGTGATACAGGCGCTGCCACAAGTGGGCAAT
CTTGGTCTTCTCTTTTTCCTGCTCTTCTTTATATTTGCTGCACTGGGTGTGGAACTTTT
TGGCAGGCTGGAGTGCAGTGAAGACAACCCCTGCGAGGGCCTGAGCAGGCACGCCA
CCTTCAGCAACTTCGGCATGGCCTTCCTCACGCTGTTCCGCGTGTCCACGGGGGACA
ATTGGAACGGGATCATGAAGGACACGCTGCGCGAGTGCTCCCGTGAGGACAAGCAC
TGCCTGAGCTACCTGCCGGCCCTGGCTCCTGTTTACTTTGTGGTCTTTGTCCTGATGG
CGCAGTTTGTGCTCGTTAATGTTGTGGTGGCCGTGCTTATGAAACATCTCGAG

DIIa1hL synthetic Oligonuceleotide sequence for insertion into LCav3-DIIa1hL and LCav3- DII_{a1hL} DIV_{a1hL} (AvrII – AfeI)

ATCCTAGGCATGCACCTTTTCGGCTGCAAGTTCAGCCTGAAGACAGACACCGGtGAC
ACCGTGCCTGACAGGAAGAACTTCGACTCCCTGCTGTGGGCCATCGTCACCGTGTTC
CAGGTACTGACGCAGGAAGACTGGAACACAGTCCTCTATAATGGCATGACCAAAAC
ATCAAACTGGGCATCACTTTACTTTGTAGCGCTCATG

A2. Plasmid Maps and Expected Banding Patterns of Restriction Enzyme Digests, Generated using Gene Construction Kit V 3.0

1. pIRES2- eGFP- LCav3-12b DIV$_{\alpha 1hL}$

a. Plasmid Map

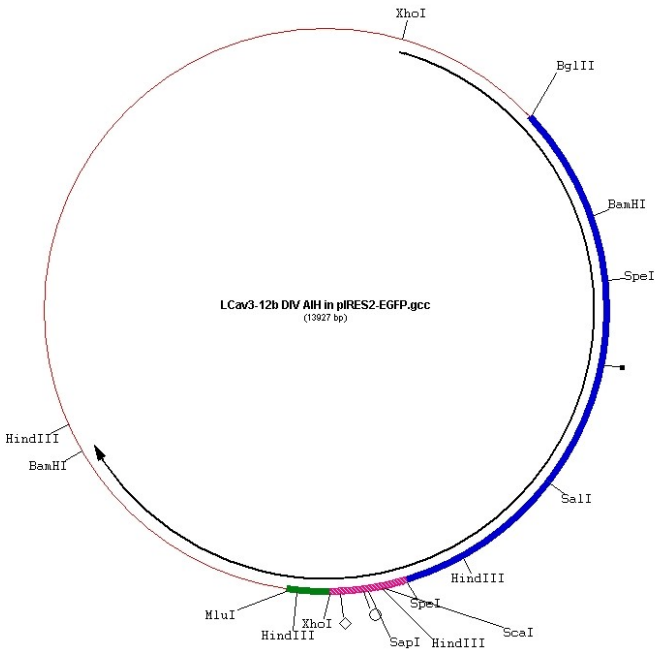

b. Expected Banding Pattern: SpeI and XhoI

Digest #1, LCav3-12b DIV AIH in pIRES2-EGFP.gcc (13927) : XhoI/SpeI

size	from	to
7610	6931 (XhoI)	613 (XhoI)
3063	3253 (SpeI)	6315 (SpeI)
2639	614 (XhoI)	3252 (SpeI)
615	6316 (SpeI)	6930 (XhoI)

Digest #1, LCav3-12b DIV AIH in pIRES2-EGFP.gcc (13927) : XhoI/SpeI

position	site
613	XhoI
3252	SpeI
6315	SpeI
6930	XhoI

2. pIRES2- eGFP- LCav3- $DII_{\alpha 1hL}$ $DIV_{\alpha 1hL}$

a. Plasmid Map

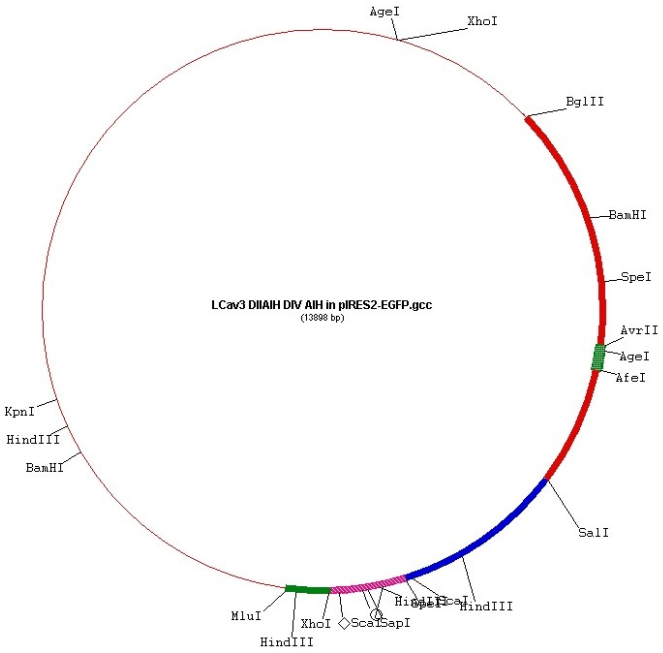

b. Expected Banding Pattern: ScaI and AgeI

Digest #1, LCav3 DIIAIH DIV AIH in pIRES2-EGFP.gcc (13898) : AgeI/ScaI

size	from	to
8028	6471 (ScaI)	600 (AgeI)
3198	601 (AgeI)	3798 (AgeI)
2431	3799 (AgeI)	6229 (ScaI)
241	6230 (ScaI)	6470 (ScaI)

Digest #1, LCav3 DIIAIH DIV AIH in pIRES2-EGFP.gcc (13898) : AgeI/ScaI

position	site
600	AgeI
3798	AgeI
6229	ScaI
6470	ScaI

3. pIRES2- eGFP- LCav3-12a DIV$_{\alpha 1hL}$

c. Plasmid Map

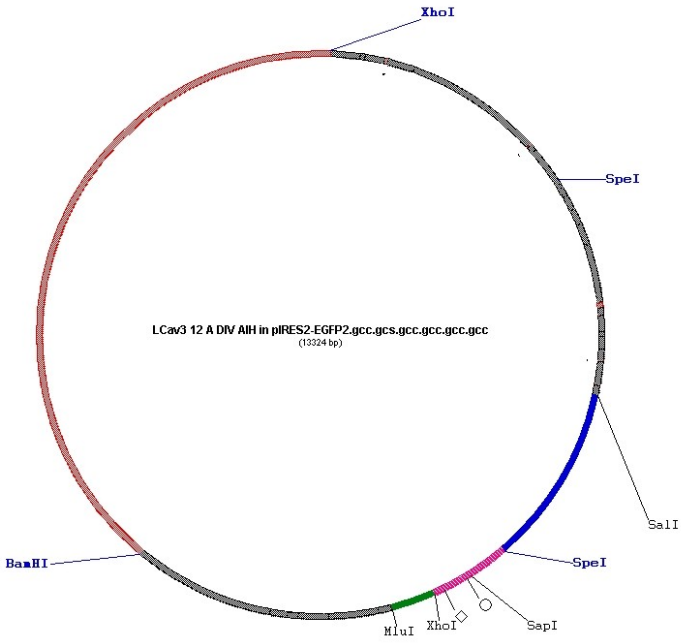

d. Expected Banding Pattern: BamHI and SalI

Digest #1, LCav3-12a DIV AIH in pIRES2-EGFP.gcc (13927) : BamHI/SalI

size	from	to
7383	9280 (BamHI)	2735 (BamHI)
4343	4937 (SalI)	9279 (BamHI)
2201	2736 (BamHI)	4936 (SalI)

Digest #1, LCav3-12a DIV AIH in pIRES2-EGFP.gcc (13927) : BamHI/SalI

position	site
2735	BamHI
4936	SalI
9279	BamHI

e. Expected Banding Pattern: XhoI

Digest #1, LCav3-12a DIV AIH in pIRES2-EGFP.gcc (13927) : XhoI

size	from	to
7610	6931 (XhoI)	613 (XhoI)
6317	614 (XhoI)	6930 (XhoI)

Digest #1, LCav3-12a DIV AIH in pIRES2-EGFP.gcc (13927) : XhoI

position	site
613	XhoI
6930	XhoI

4. pcDNA3.1- Cav3.2 DII_{D975N}

   a. Plasmid Map

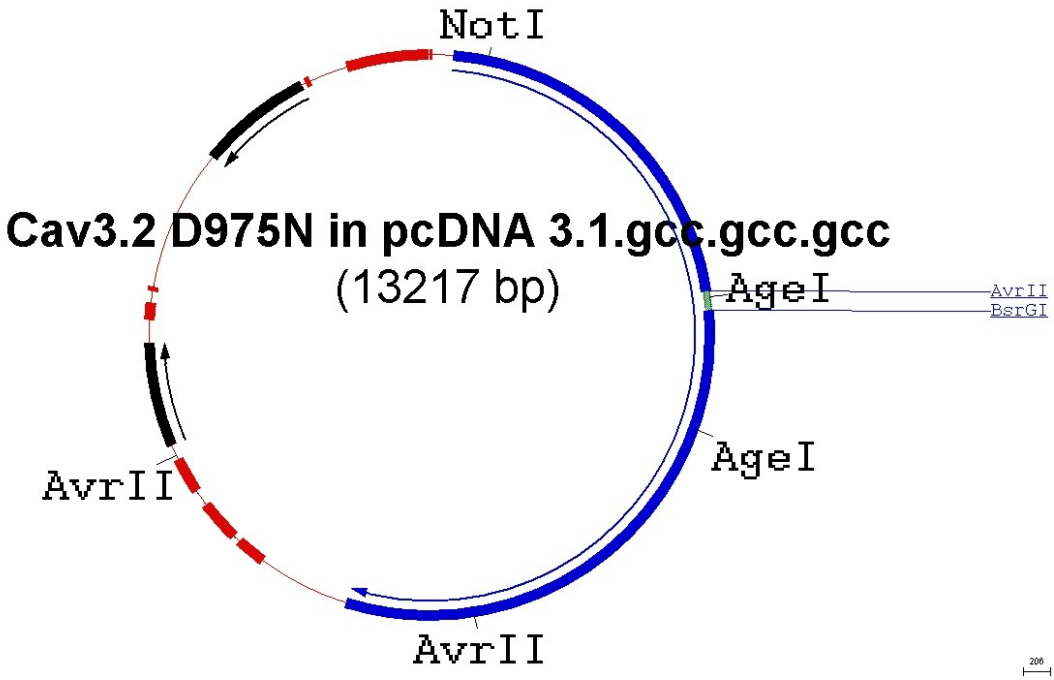

   b. Expected Banding Pattern: AgeI and NotI

Digest #1, Cav3.2 D975N in pcDNA 3.1.gcc.gcc.gcc (13217) : NotI/AgeI

size	from	to
9637	4024 (AgeI)	443 (NotI)
2577	444 (NotI)	3020 (AgeI)
1003	3021 (AgeI)	4023 (AgeI)

Digest #1, Cav3.2 D975N in pcDNA 3.1.gcc.gcc.gcc (13217) : NotI/AgeI

position	site
443	NotI
3020	AgeI
4023	AgeI